

Integrating Protein Engineering and Genomics for Cancer Therapy

by

Mandana Taghizadeh Manzari

Department of Biomedical Engineering
Duke University

Date: _____

Approved:

Ashutosh Chilkoti, Supervisor

Kris C. Wood

Jennifer L. West

Xiling Shen

George A. Truskey

Dissertation submitted in partial fulfillment of
the requirements for the degree of Doctor
of Philosophy in the Department of
Biomedical Engineering in the Graduate School
of Duke University

2018

ABSTRACT

Integrating Protein Engineering and Genomics for Cancer Therapy

by

Mandana Taghizadeh Manzari

Department of Biomedical Engineering
Duke University

Date: _____

Approved:

Ashutosh Chilkoti, Supervisor

Kris C. Wood

Jennifer L. West

Xiling Shen

George A. Truskey

Dissertation submitted in partial fulfillment of
the requirements for the degree of Doctor
of Philosophy in the Department of
Biomedical Engineering in the Graduate School
of Duke University

2018

Copyright by
Mandana Taghizadeh Manzari
2018

Abstract

We have developed a broadly applicable platform that harnesses the power of protein engineering and genetic screening to produce efficacious protein-drug combinations for cancer therapy. For proof-of-concept, we implemented this strategy to engineer targeted pro-apoptotic drug combinations that overcome cancer resistance to protein agonists of death receptor 5 (DR5), a key upregulated marker in colorectal cancer (CRC). Over the past decade, various DR5 agonists have shown poor clinical efficacy, including both engineered antibodies and TRAIL, the natural ligand for this receptor. Comprehensive studies suggest that there are three major obstacles to success of these agents: 1) potency, 2) delivery, and 3) resistance.

We have systematically addressed these challenges by engineering a sustained-release formulation of a highly potent, hexavalent death receptor 5 agonist (DRA), and administering the agonist as a sustained release depot, in combination with rationally nominated targeted drugs that overcome intrinsic resistance to DRAs. To address the need for sustained delivery of therapeutic proteins, we developed injectable depots of DRAs recombinantly fused to thermally responsive elastin-like polypeptide (ELP) biopolymers. The bioactive ELP-DRA fusions undergo temperature-driven phase transition upon subcutaneous injection in vivo, resulting in the formation of a gel-like

depot suitable for sustained drug delivery. A single 30 mg/kg injection of the gel-like ELP-DRA depot induced significant tumor regression in Colo205 mouse xenografts. To pinpoint the genetic drivers of CRC resistance to the DRA, we used a gain-of-function ORF screen and a CRISPR/Cas9 knockout screen. The screens identified genes that confer sensitivity to the DRA in resistant CRC cell lines. Over twenty small molecule drugs targeting pathways and proteins identified from the screens were then tested in combination with the DRA to identify highly synergistic combinations using cytotoxicity assays. Clonogenic, time-to-progression, and cell viability assays showed that pharmacological blockade of XIAP, Bcl-X_L, and CDK4/6 strongly enhances antitumor activity of DRA in established human CRC cell lines and patient-derived CRC cells. *In vivo* tumor regression studies demonstrated the potent anti-tumor efficacy of combining inhibitors of XIAP and Bcl-X_L with the sustained release formulation of ELP-DRA.

By addressing both delivery and resistance issues with our protein engineering and genomics platform, we have overcome the key obstacles to DRA translation as a successful drug in the clinic. Our rational approach elegantly provides optimal protein-small molecule drug combinations that elicit a robust anticancer response, exhibit minimal toxicity, and combat drug resistance.

Dedication

Dedicated to my grandfather Manouchehr Parvaz, whose love of education and humanity motivates my commitment to knowledge and science.

Contents

Abstract	iv
List of tables	xii
List of figures	xiii
Acknowledgements	xvi
1. Introduction	1
1.1 Protein engineering for cancer therapy	1
1.1.1 Engineering of scaffold-based proteins.....	5
1.1.2 Challenges in development of scaffold-based protein drugs	8
1.1.3 Extrinsic apoptotic pathway agonists.....	9
1.2 Effective delivery of protein therapeutics.....	13
1.2.1 Strategies for improved protein delivery	13
1.2.2 Elastin-like polypeptides.....	15
1.3 Genomics in cancer therapy	16
1.3.1 Using genomics to understand cancer drug resistance	17
1.3.2 Lentiviral ORF gain-of-function screens	18
1.3.3 CRISPR/Cas9 knockout screens.....	19
1.4 Objectives.....	21
2. Design, production, and evaluation of death receptor agonists (DRAs)	24

2.1 Introduction.....	24
2.2 Materials and methods	26
2.2.1 Molecular biology of construct fusions	26
2.2.2 Expression and purification.....	27
2.2.3 Evaluation of extrinsic pathway gene expression	29
2.2.4 Cell Lines and Cytotoxicity assays.....	29
2.3 Results and discussion.....	31
2.3.1 Protein expression and characterization	31
2.3.2 Evaluation of extrinsic pathway gene expression	33
2.3.3 Cytotoxicity results	35
2.3.4 Apoptotic competence of DRA-resistant cancer cells	36
2.4 Significance.....	37
3. Engineering ELP-DRA fusions for <i>in vivo</i> sustained release	39
3.1 Introduction.....	39
3.2 Materials and methods	42
3.2.1 ELP-DRA fusion molecular biology	42
3.2.2 ELP-DRA fusion purification.....	42
3.2.3 Dynamic light scattering	44
3.2.4 ELP-DRA optical turbidity.....	45
3.2.5 ELP-DRA fusion <i>in vitro</i> testing	45

3.2.6 Tumor regression analysis <i>in vivo</i>	46
3.3 Results and discussion.....	46
3.3.1 Design of ELP fusions to death receptor-binding domains	46
3.3.2 Purification of ELP-DRAs	49
3.3.3 Characterization and depot formulation of ELP-DRAs.....	52
3.3.4 Depot-forming ELP-DRA formulation abolishes tumors <i>in vivo</i>	55
3.4 Significance.....	58
4. Rational design of drug combinations to overcome DR5 agonist resistance in cancer cells.....	60
4.1 Introduction.....	60
4.1.1 ORF gain-of-function screen	60
4.1.2 CRISPR/Cas9 loss-of-function screen	61
4.2 Materials and methods	63
4.2.1 ORF gain-of-function screen.....	63
4.2.2 CRISPR/Cas9 loss-of-function screen	64
4.2.3 Short-term drug combination studies	67
4.2.4 Long-term drug combination studies.....	69
4.2.5 Immunoblotting.....	70
4.3 Results and discussion.....	71
4.3.1 ORF GOF screen results.....	71

4.3.2 CRISPR/Cas9 LOF screen results	74
4.3.3 Genetically credentialed targeted inhibitors potentially sensitize cancer cells to DRA in short-term <i>in vitro</i> studies	79
4.3.4 Long-term <i>in vitro</i> studies confirm efficacy of sensitizers in combination with DRA in patient-derived DRA-resistant cells	83
4.3.5 DRA combination with key sensitizers promotes apoptotic pathway signaling	87
4.4 Significance.....	89
5. Integration of delivery and genomics to improve DRA efficacy in patient-derived xenografts.....	90
5.1 Introduction.....	90
5.2 Materials and methods	90
5.2.1 Cell lines and cell viability assays.....	90
5.2.2 <i>In vivo</i> patient-derived xenograft study	92
5.3 Results and discussion.....	93
5.3.1 Selection of drug combinations for <i>in vivo</i> studies	93
5.3.2 Pilot <i>in vivo</i> study for toxicity evaluation.....	97
5.3.3 <i>In vivo</i> tumor regression study confirms superior efficacy of rationally designed drug combinations	100
5.4 Significance.....	102
6. Conclusions.....	105
6.1 Platform summary and application for broad use	105

6.2 Future Perspectives: Integrating genomics and drug delivery	107
Appendix A.....	113
Appendix B.....	114
Appendix C.....	156
References	157
Biography.....	172

List of tables

Table 1: Summary of expression and purification approaches for depot-forming ELP-DRA fusion.	51
Table 2: Examples of hits from sensitizer screen.	78
Table 3: Summary of sensitizer drugs and observed DRA EC ₅₀ and E _{max} in combination cell viability assays.....	81

List of figures

Figure 1: Procedure for engineering scaffold-based proteins.....	7
Figure 2: Tenth type III domain of human fibronectin (Fn3).....	8
Figure 3: TRAIL binding to DR4 or DR5 results in receptor homotrimerization.	10
Figure 4: Hexavalent DR5-binding Tn3 fusions are potent pro-apoptotic drugs.	12
Figure 5: Multidisciplinary platform for cancer drug development.	23
Figure 6: DRA-induced DR5 crosslinking results in potent apoptotic signal.	25
Figure 7: Construction, expression, and purification scheme for DRA.....	28
Figure 8: Periplasm of <i>E. coli</i> , located between the inner and outer membranes.	32
Figure 9: Protein characterization of DRA and TRAIL.....	32
Figure 10: Anti-DR5 immunoblot confirms DR5 expression in panel of human colorectal cancer cell lines.....	33
Figure 11: TRAIL sensitivity cannot be explained by differential expression of extrinsic pathway proteins.	34
Figure 12: Cytotoxicity dose-response curves for TRAIL and DRA in human colorectal cancer cell lines.....	36
Figure 13: DRA-resistant human CRC cells can undergo apoptosis.	37
Figure 14: Fusion of thermally responsive ELPs to death receptor agonists enables depot formation for sustained release.....	41
Figure 15: Fusion of thermally responsive ELPs to bivalent and tetravalent DR5-binding Tn3 domains.	48
Figure 16: Schematic of ELP-DRA fusion purification and final product.....	50

Figure 17: ELPs fusion to the DRA does not affect DRA potency in cytotoxicity assays.	52
Figure 18: ELP-DRA formulation demonstrates appropriate phase-transition behavior for gel depot formation.	54
Figure 19: Fusions of hydrophobic ELP to DRA form nanoparticles at physiological temperature.	55
Figure 20: Pilot tumor regression study confirms ELP-DRA depot efficacy in vivo.	56
Figure 21: ELP-DRA depot demonstrates superior in vivo efficacy.	57
Figure 22: ELP-DRA formulation is efficacious when injected subcutaneously and does not require intratumoral injection for in vivo tumor regression.	58
Figure 23: Schematic of CRISPR/Cas9 knockout screen.	63
Figure 24: Overview of the gain-of-function ORF library screen.	64
Figure 25: Overview of loss-of-function CRISPR screen experimental set-up.	67
Figure 26: GOF ORF screen results reveal key players in TRAIL resistance.	72
Figure 27: Replicate comparison of gene-level essentiality phenotypes in the CRC cell line RKO.	76
Figure 28: CRISPR/Cas9 loss-of-function screen results for TRAIL and DRA.	77
Figure 29: Drug combination guidelines and efficacy summary.	80
Figure 30: Cell viability assay results of combination treatment of DRA with targeted sensitizer drugs in RKO and three patient-derived cell lines.	83
Figure 31: Clonogenic 2D growth assay experiments in human colorectal cancer cells demonstrate long-term potency of drug combinations.	85
Figure 32: Time-to-progression assay in patient-derived CRC247s.	86

Figure 33: Flow cytometry data shows increased cytotoxicity (positive Annexin V staining) in for combination treatment conditions in RKO cells.....	87
Figure 34: Increased extrinsic and intrinsic pathway activation observed with combination treatments.	88
Figure 35: Selected drug combinations for <i>in vivo</i> tumor regression studies.....	94
Figure 36: A-1331852 potentially sensitizes RKO cells to DRA <i>in vitro</i>	94
Figure 37: A-1331852 potentially sensitizes patient-derived CRC247 cells to DRA.	95
Figure 38: Cell viability assay of single agent sensitizers in CRC247 cells.	96
Figure 39: ELP-DRA is equally potent as DRA when combined with sensitizer drugs in patient-derived CRC247 cells.	97
Figure 40: Weight loss data for animals treated with A-1331852 in combination with palbociclib.	98
Figure 41: Combination of DRA with XIAP and BCL-X _L inhibitors is tolerable <i>in vivo</i> in patient-derived xenografts.	99
Figure 42: CRC247 PDX data demonstrates <i>in vivo</i> efficacy of the A+B+DRA compared to other treatment groups.	101
Figure 43: Kaplan-Meier survival analysis results.	102
Figure 44: CRC247 PDX data over course of entire study.....	156

Acknowledgements

Foremost, I would like to sincerely thank my advisor, Dr. Ashutosh Chilkoti, without whom this thesis would not be possible. I am grateful for his enthusiastic support and for his faith in my scientific explorations throughout my PhD. His curiosity and passion for discovery have motivated me through the inevitable challenges that arose along the path to this degree. His flexibility made this research possible, opening doors to a new, highly interdisciplinary way of approaching cancer therapy. Despite having many other responsibilities, he has consistently demonstrated his dedication to my scientific growth, making time to share his knowledge and experience. I feel remarkably lucky to have worked in his group, as the opportunities, scientific training, and exposure that I gained have given me confidence as a researcher.

My dissertation work was completed in constant collaboration with Dr. Kris Wood, whose constructive guidance, enthusiasm, and encouragement inspired my growth both professionally and personally. His knowledge and creativity made this work possible, and I greatly appreciate his generosity in sharing his time, experience, and ideas. I am also grateful for the feedback and discussions with the other members of my committee.

I express my deepest gratitude to my parents, Simin Parvaz and Majid T. Manzari for their incredible sacrifice by building a life for our family in the United States. My achievements are a direct reflection of the love, dedication, and resources they have provided throughout my entire life. I am very grateful for my brother, Mohammad, who has consistently helped me navigate the world since childhood, and always with endless empathy and encouragement.

I would like to thank my wonderful friends, Kristen Peña, Shiva Prakash, Janelle Fouché, Marine Minvielle, Penni Perrotte, Lisa Cervia, Alison Tisdale, Geraldine Paulus, Kamil Gedeon, Julie Paul, Arati Prakash, Tian Ong, Sisi, and Katayoun Sadri, who have been constant sources of support during my time at Duke and beyond. These friendships have been a source of laughter, inspiration, motivation, and comfort for many years. Simone Costa, thank you for being an amazing labmate and friend over the years. Your friendship empowered me every day inside and outside of the lab. I will always be grateful that you introduced me to my first and beloved dog- Dalton, who taught me what's important in life.

I want to thank my partner AJ, who has been a stabilizing force, sharing in my struggles and successes over the past year. I thank him for his loving kindness, support,

and patience, and for always lifting me up. I also thank him for our ray of sunshine, Riley, who provided constant encouragement as I wrote this dissertation.

I would also like to thank my mentors. My graduate student mentor from MIT, Dr. Jamie Spangler, has shown unwavering support and encouragement over the years. My former supervisor from Eleven, Dr. Mike Schmidt, your perseverance in research and professionalism in the laboratory continues to inspire me. Dr. David Katz, thank you for the amazing opportunity to teach with you, and for your advice and kindness. Dr. Theodore Slotkin, thank you for your outstanding service to Duke as an educator, for understanding the urgency of scientific discussions, and for your patience in helping me with *in vivo* studies. Dr. Eric Monson, thank for your invaluable guidance on data visualization and research presentations.

I would like to genuinely thank all of my colleagues in the Chilkoti and Wood labs; especially Grace Anderson, Kevin Lin, Maréva Fevre, Eric Mastria, Stefan Roberts, Michael Dzuricky, Sarah MacEwan, Wafa Hassouneh, Zareen Kapadia, and Krissey Lloyd. I am deeply indebted to my amazing mentees, Chandler Moore, Mitchell Zhang, Rachel Skelton, and Victoria Nguyen, for their hard work in the laboratory. With many of my colleagues- Parisa Yousefpour, Joseph Bellucci, Nicholas Tang, Davoud Mozhdehi, Imran Ozer, and Samagya Banskota- I have developed friendships that I am

sure will outlast our time at Duke. I am also incredibly grateful to have had the perfect officemate- Dr. Xinghai Li, who I am indebted to for his patience and generous technical help with *in vivo* studies.

1. Introduction

Despite decades of research and significant progress in the field of cancer therapy, delivery barriers and drug resistance substantially limit treatment efficacy in the clinic. At the preclinical stage, scientific research is often solely focused on one specific aspect of therapeutic improvement. In this work, we introduce a novel platform for cancer drug development that addresses drug delivery and resistance issues through the integration of the largely siloed fields of protein engineering and genomics. A brief discussion of the current state of the art in each field follows.

1.1 Protein engineering for cancer therapy

While incredible medical and biotechnological feats over the past 100 years have led to crucial discoveries and treatments for many cancers, they have also revealed the staggering complexity of these diseases. The understanding that tumor cells evolve from “self” raises an incredibly difficult question: how can we develop drugs that most effectively eliminate cancer while differentiating as much as possible between normal and malignant cells? Chemotherapeutics are among the options for the first line of treatment, and although they inhibit the proliferation of tumor cells, they often damage healthy cells and result in serious side effects. In the 1900’s, physician and scientist Paul Ehrlich proposed the revolutionary concept of “magic bullet” drugs, which could fight against human disease by finding and affecting specific targets without harming healthy tissue. Ehrlich’s ideas have since been the basis for decades of groundbreaking research,

from the development of hybridoma technology for production of monoclonal antibodies to the design of personalized immunomodulatory drugs (1-3). In cancer treatment, the advantage of such targeted therapies lies in the exquisite specificity of the drug to molecules expressed on tumor cells but lacking or less prominent in healthy tissue (4). Antibodies are targeted affinity proteins, evolved by nature to bind specifically to other molecules (5). Their innate tolerance of alteration and manipulation of variable regions has made antibodies an extremely important class of tumor targeted agents. Differentially expressed cell surface antigens can be targeted by antibodies acting as immunomodulatory molecules, antagonists/agonists of specific cellular receptors, or target-specific molecules loaded with chemotherapeutics.

Since the mid-1990's, over 60 antibody-based drugs have been approved for therapeutic use, twelve of which are anti-tumor antibodies clinically established as the standard of care for a number of cancers including breast cancer, leukemia, lymphoma, lung, kidney, and colorectal cancer (6). These antibodies have anti-cancer efficacy through direct tumor cell killing, vascular or stromal cell ablation, or immune-mediated tumor cell elimination (7). Successfully targeted tumor antigens include epidermal growth factor receptor (EGFR), vascular endothelial growth factor receptor (VEGFR), cytotoxic T lymphocyte-associated antigen 4 (CTLA4), and CD20 (8). Despite these successes, antibody-derived therapeutics have some important limitations, as described in the remainder of this section.

Antibody valency, architecture, and production cost can dramatically hinder their development and use as therapeutics. The bivalency of antibodies limits their potency in certain contexts, and although higher valency fusions have been developed with the attachment of additional binding domains, the size of these fusions restricts effective penetration into the tumor fusions (9). The ideal valency of the antibody or protein therapeutic depends on target antigen density on the cell surface, accessibility of adjacent epitopes, and conformational flexibility. In some cases, the architecture and steric constraints of antibodies significantly limit conformational flexibility, precluding a specific type of desired binding interaction- especially if distances of target epitopes are incongruent with distances between the antibody's binding domains (9). Specifically, higher order clustering of certain target receptors can be necessary to trigger downstream signaling. This clustering effect has been shown to be critical to the efficacy of antibodies targeting tumor necrosis factor receptor (TNFR) family members CD40, death receptor 5 (DR5), and CD95(Fas) (10-13). To achieve higher order clustering, the Fc domain of a monoclonal IgG antibody must bind to Fc- γ receptors; the need for this additional step dramatically reduces efficiency and potency of the antibodies, especially compared to alternative protein formats designed with necessary multimeric properties that do not require a secondary crosslinking step (14).

Aside from valency and architectural limitations, inadequate tumor penetration, structural complexity, and high cost of production also present significant challenges to

development of antibody-based drugs. The large size of antibodies reduces diffusion rate, impedes solid tumor uptake, and ultimately hinders efficacy (8, 15-17). Structural complexity involving multiple domains, disulfide bonds, and post-translational modifications also hinder antibody manipulation and necessitate costly production in mammalian cells (8, 18). Antibodies are also highly prone to degradation, aggregation, and high viscosity at the high concentrations required for drug administration, which increases the likelihood of immunogenicity and reduces the range of possibilities for payload attachment (18).

To address some of these issues, the field has expanded toward the development of antibody fragments, such as single-chain variable fragments (scFvs) and fragment antigen-binding (Fab) fragments, which are smaller and therefore demonstrate better tissue penetration and improved targeting of cryptic epitopes (9, 19-21). Unfortunately, these formats often fail to retain the high affinity of the parent antibody, and manifest other undesirable properties including inefficient folding in *E. coli*, oligomerization, aggregation, low yield, short plasma half-life, and reduced antigen-binding activity upon fusion to other peptides or proteins (22-24). Thus, there is a need for modular, stable protein templates that can be engineered to bind a specific target. An ideal alternative binding protein framework would be composed of highly stable, engineered protein scaffolds that are inexpensive to produce and easy to manipulate into multivalent, recombinant fusions of various sizes, architectures, and pharmacological

properties. The following section describes the emerging role of protein scaffolds for tumor targeting.

1.1.1 Engineering of scaffold-based proteins

Scaffold-based proteins are less prone to aggregation than Ig-based formats, easier to produce at high yields in microbiotic culture, and more intrinsically stable. The robustness of scaffold-based protein drugs is also advantageous in the context of conjugation of desired payloads, including chemotherapeutic drugs; stable scaffolds may not aggregate as readily as Ig-based proteins upon attachment of hydrophobic small molecules.

Recently, protein scaffolds have been engineered into a variety of therapeutic and diagnostic formats. The key properties of non-Ig fold protein scaffolds are (1) a single polypeptide chain with a highly structured core, (2) tolerance of conformational changes introduced in the form of various insertions, deletions, or amino acid changes in the variable region, (3) modularity due to small size (2-4KDa for constrained peptides; 6-20 kDa for protein domains) (25, 26). Once a template scaffold is chosen, molecular design and selection techniques are used for development of a variant that binds to a target protein with high affinity.

Technological progress in the field of protein engineering has enabled scientists to evolve proteins into highly specific targeting agents for manipulation of tumor cell signaling. Combinatorial protein engineering and molecular selection techniques such as

phage, yeast, and mRNA display technologies provide a physical link between genotype and phenotype of huge libraries of protein variants, enabling screening of billions of molecules that share the same core framework. Directed evolution and affinity maturation of variants from these libraries reveal high affinity proteins that bind to specific targets of interest. For example, the 3-helix affibody scaffold, which is based on a 58 amino acid protein domain derived from staphylococcal protein A, has been evolved to bind the cell surface receptor HER2. The HER2-specific affibody has been used to image HER2 expression in metastatic breast cancer patients (27). Advances in molecular modeling and computational tools have also facilitated rational protein design strategies based on relationships between protein sequence, structure, and function (28). A summary of the workflow for scaffold-based protein agent development can be found in Figure 1.

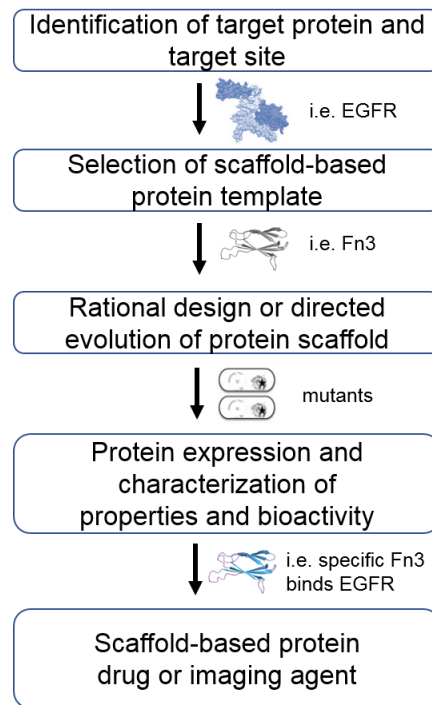


Figure 1: Procedure for engineering scaffold-based proteins.

First a target of interest is identified. Then a scaffold-based protein template can be selected for mutagenesis by computational methods (rational design) or display technologies (directed evolution), or a combination of both approaches. Mutants are selected based on affinity for target protein, characterized, and optimized (23, 29). PDB ID: 1TTF.

One promising protein scaffold domain is the tenth type III fibronectin domain of human fibronectin (Fn3), which is structurally analogous to the variable region of an antibody and has been engineered to bind vascular endothelial growth factor receptor 2 (VEGFR2) and epidermal growth factor receptor (EGFR), among other targets (30). Fn3 is a 10 kDa, highly stable, soluble scaffold that can be expressed with high yield in *E. coli*. Fn3 structure consists of 3 solvent-exposed loops (BC, DE, FG) that can tolerate a diverse range of sequences (Figure 2) (31). The native domain contains an RGD peptide within its FG loop that is key in binding to integrins (32). Directed evolution and affinity

maturation of Fn3s using library screens has enabled development of variants that can bind target proteins with nanomolar or sub-nanomolar affinity (33). An anti-VEGFR2 Fn3 binds to its target with 11 nM affinity and inhibits VEGF-dependent proliferation of cancer cells. Phase II clinical trials are underway to evaluate the efficacy of this VEGFR2 inhibitor, CT-322, in patients with glioblastoma multiforme, non-small cell lung cancer, and metastatic colorectal cancer (34).

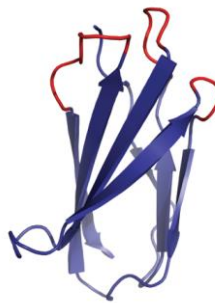


Figure 2: Tenth type III domain of human fibronectin (Fn3).

Fn3 is a scaffold for engineering of proteins for binding to therapeutic targets of interest. The 3 red loops at the top of the crystal structure highlight the variable region that can be manipulated by mutagenesis. PDB ID: 1TEN.

1.1.2 Challenges in development of scaffold-based protein drugs

While the stability and malleability of scaffold-based protein agents are highly advantageous, there are key challenges associated with translation of these proteins for clinical use. These challenges include immunogenicity, rate of tissue penetration, and-most importantly- short serum half-life. The immunogenicity of protein-based therapeutics is highly dependent on the specific protein in question, and more clinical trial data is necessary before reliable conclusions can be drawn regarding this problem

for a specific class of scaffold proteins. The rate of tissue penetration and biodistribution of scaffold-based drug is based on size, and single-domain drugs are smaller than the optimal size for tumor penetration specifically (17). This issue, as well as that of short serum half-life, can be addressed by conjugation of polymers, or fusion of recombinant proteins to increase molecular weight. The modularity and stability of scaffold-based proteins streamlines such modifications. For example, the aforementioned Fn3 VEGFR2 inhibitor, CT-322, has been chemically conjugated to a polyethylene glycol (PEG) polymer to extend circulation half-life (35). This and other drug delivery strategies are essential to clinical feasibility of protein drugs. One class of proteins, extrinsic pathway agonists, is an especially powerful model of the full gamut of delivery and efficacy challenges associated with recombinant proteins, monoclonal antibodies, and scaffold-based drugs. The evolution of this class of agonists is described in the following section.

1.1.3 Extrinsic apoptotic pathway agonists

Over twenty years ago, it was discovered that TNF-related apoptosis-inducing ligand (TRAIL, also Apo2L) kills many cancer cells *in vitro* and *in vivo* while remaining innocuous to normal cells (36-38). Upon binding to death receptors 4 or 5 (DR4 or DR5), TRAIL activates the extrinsic apoptotic pathway and induces programmed cell death (apoptosis) in a range of human cancer cell lines, including breast, lung, colon, melanoma, lymphoma, pancreatic, and prostate (36). TRAIL binding to DR4 or DR5 on the surface of cancer cells results in receptor trimerization, which is crucial for

subsequent downstream signaling (Figure 3). However, there is evidence that normal cells are protected from TRAIL-induced apoptosis by multiple, redundant pathways, differential DR4/DR5 expression, and the presence of TRAIL-binding decoy receptors (DcR1 and DcR2) that lack intracellular death domains, and thus inhibit apoptotic signaling (38).

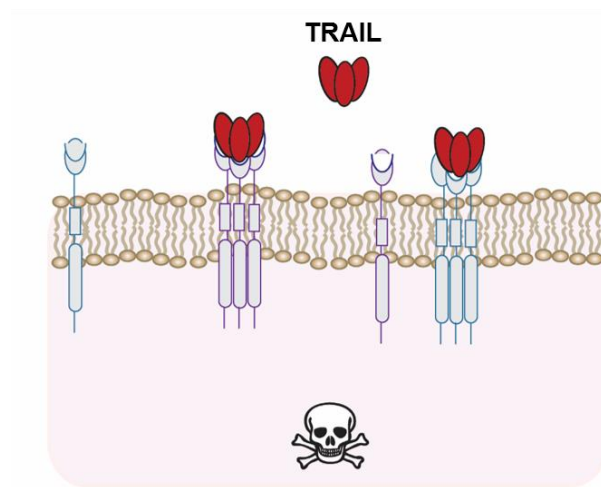


Figure 3: TRAIL binding to DR4 or DR5 results in receptor homotrimerization. Binding of homotrimeric TRAIL to death receptors results in receptor trimerization, which is necessary for effective induction of downstream apoptotic signaling in tumor cells.

Over the past two decades, TRAIL and other promising extrinsic apoptotic pathway agonists (i.e. monoclonal antibodies or mAbs) have been developed and tested in the clinic, but none of these drugs showed robust therapeutic efficacy in patients. From the significant efforts expended to understand this outcome, a number of important, interrelated conclusions have emerged. Clinical translation of TRAIL, the

natural ligand for DR5, was confounded by its short half-life, inadequate delivery to cancer cells, and the presence of TRAIL-resistant cancer cell populations (39). Despite the pharmacokinetic advantages of DR5-specific antibodies, it is thought that the bivalency of these drugs resulted in subpar potency, likely due to their inability to trimerize the death receptors for initiation of apoptotic signaling. Due to the bivalency of mAbs, these drugs were dependent on a separate cross-linking platform for agonistic activity, which, in fact, could still not achieve the higher order cross-linking of many TNF-family receptors required to trigger optimal signaling (11, 40). The development of highly potent, multivalent DR5 agonists has overcome this issue through maximization of receptor engagement and induction of downstream signaling. The remainder of this section focuses on a recent study, in which scaffold-based death receptor agonists were developed and optimized for potency in cancer cells.

In 2013, Swers and colleagues isolated a DR5-specific Tn3 protein and assembled the domains into multivalent fusion proteins with pro-apoptotic activity. The Tn3 scaffold is derived from the third fibronectin type III domain of human tenascin C and exhibit the same fold as Fn3 (41). This scaffold was directed to bind DR5 with high affinity (43 nM); fusions of repeated DR5-specific Tn3 units were then constructed to generate multivalent, cancer-killing proteins of various formats, including an Fc fusion, an IgG1 fusion, and linear fusions (14). Interestingly, the tetravalent linear fusion demonstrated a 1000-fold increase in bioactivity when compared to the tetravalent IgG1

fusion, suggesting that the flexibility of the linear format translates to enhanced potency. In vitro characterization of multivalent linear agonists also revealed their enhanced potency compared to TRAIL in both TRAIL-sensitive and certain TRAIL-resistant cell lines. Interestingly, mono- or di-valent DR5-binding domains did not induce apoptosis, but the hexavalent linear construct was extremely cytotoxic in sensitive cell lines, likely due to the enhanced signaling strength owed to higher order receptor crosslinking (Figure 4). The hexavalent linear fusion demonstrated maximal potency *in vitro* and exhibited potent anti-tumor activity when tested *in vivo* in murine xenografts. These exciting results corroborated the idea that scaffold-based proteins can be powerful protein drugs due their modularity and ease of manipulation (14).

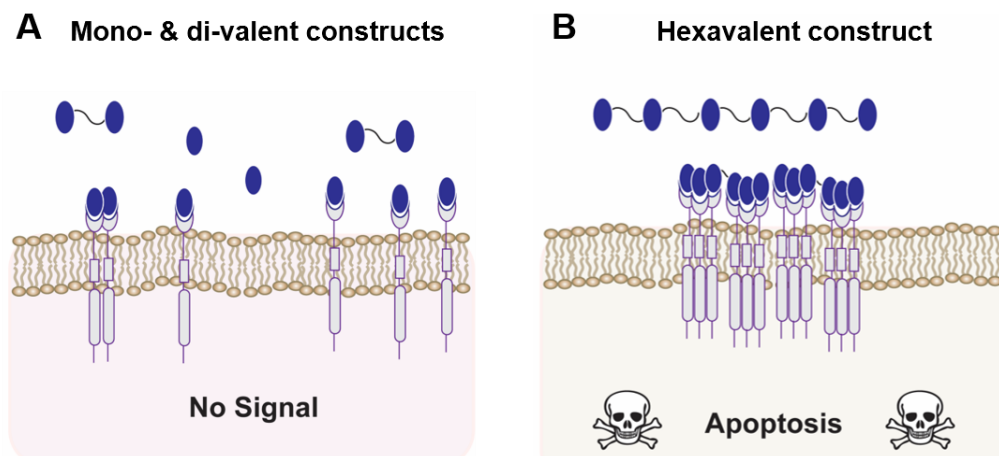


Figure 4: Hexavalent DR5-binding Tn3 fusions are potent pro-apoptotic drugs. Multivalency of linear fusions of DR5-binding Tn3 domains is critical to activity. (A) Monovalent and divalent Tn3 domains have no effect on cells due to lack of receptor trimerization. (B) Hexavalent linear fusions of Tn3 domains facilitate receptor trimerization and higher order crosslinking for potent cytotoxicity in cancer cells.

Despite these excellent preclinical results, the super-potent, hexavalent, extrinsic apoptotic pathway agonists suffer from subpar pharmacokinetics (serum half-life of 36 minutes), and therefore require modification for improved tumor delivery and feasibility of clinical administration. Next, we will discuss approaches for improving protein drug delivery, highlighting a few strategies in particular.

1.2 Effective delivery of protein therapeutics

1.2.1 Strategies for improved protein delivery

The promise of protein therapeutics is commonly hampered by rapid renal clearance, enzymatic degradation, and uptake in non-target tissues. To address these challenges, a number of approaches have been established, including polymer conjugation, tumor targeting, and microparticle drug carriers. Polymer conjugation can increase protein longevity in circulation by increasing molecular weight above the kidney filtration cut-off and reducing susceptibility to enzymatic degradation. If the protein is encapsulated in a liposome or similar drug delivery vehicle, increased tumor specificity is achieved through attachment of vector molecules, such as antibodies, to the surface of the vehicle. Micro-reservoirs such as liposomes and micelles are used to improve circulation half-life, reduce degradation, increase accumulation in the tumor, and avoid direct conjugation with the therapeutic molecule (42, 43). Despite the benefits of these delivery strategies, each of these still requires frequent parenteral administrations and results in a bolus effect, which may have undesirable side effects.

An ideal protein delivery system for cancer therapy would provide sustained circulating levels of the protein and limit injection frequency.

For prolonged release and circulation, proteins are often conjugated to large polymeric carriers such as polyethylene glycol (PEG) or entrapped in synthetic polymer matrices such as poly(D,L-lactide-co-glycolide) (PLGA) microspheres. For example, PEGylation of IFN- α 2 improved lymphatic uptake and antitumor efficacy in a metastatic breast tumor model (44). PEGylation, however, is a costly approach for half-life extension, and can often reduce protein bioactivity (45). In microsphere formulations, issues such as protein stability and bioavailability can also limit practicality (46).

Ideally, the most effective delivery system for targeted anti-cancer proteins (1) reduces necessary injection frequency by providing sustained release from a depot, (2) maintains the potency of the bioactive protein, (3) increases molecular weight of the therapeutic protein to increase circulation time upon release from depot, (4) can be produced at low cost for ease of manufacturing and scale-up. This can be accomplished using biopolymers such as elastin-like-polypeptides, which can (1) confer desired material properties to recombinantly fused therapeutic proteins, (2) retain bioactivity of the fused proteins, (3) increase molecular weight of the fused proteins, and (4) be produced in *E. coli* and purified easily from contaminant proteins. This class of biopolymers is introduced in the following section.

1.2.2 Elastin-like polypeptides

Elastin-like polypeptides (ELPs) are repetitive, artificial, genetically encoded biopolymers derived from recurring amino acid sequences found in the hydrophobic domain of tropoelastin. Tropoelastin is the soluble precursor to insoluble elastin, a component of extracellular matrix (ECM). The ELP repeat unit is the pentapeptide (VPGXG), where X can be any amino acid except proline. ELPs are stimulus-responsive biopolymers that exhibit lower critical solution temperature (LCST) behavior, meaning that they are soluble below a critical transition temperature (T_t). Heating above the T_t triggers ELP phase transition and reversible aggregation into an insoluble coacervate (47). The T_t of ELPs depends on X, the guest residue of the pentapeptide sequence and n, the number of repeats of the pentapeptide sequence; hydrophobic X amino acids and larger repeat number n lower the T_t . The T_t is also dependent on the concentration and buffer of the ELP, as more concentrated ELP solutions in higher salt buffers will transition at lower temperatures.

ELPs have some key advantages over synthetic polymers. Their genetically encoded design allows for precise control over sequence and chain length and ensures monodispersity of the purified product. This design also permits straight-forward fusion of ELP genes to those of proteins and peptides of interest for production of recombinant protein-ELP fusions. Their environmental responsiveness can be used for chromatography-free purification by inverse transition cycling, a process that involves triggering phase transition with heat or salt, centrifuging to obtain the aggregated fusion

proteins, and reversing the transition by lowering the temperature and salt content to obtain the resolubilized product (48-50). Fusion of an ELP biopolymer to a protein or peptide of interest can confer the material properties (i.e. phase transition behavior) of the ELP, enabling production of an injectable protein drug depot. This approach has been successful for creation of a sustained-release glucagon-like peptide 1 (GLP-1) depot for diabetes treatment (51). Slow release of the fusions from the depot prolongs the availability of the protein therapeutic.

1.3 Genomics in cancer therapy

Over the past 15 years, comprehensive sequencing efforts have enabled cancer researchers to collect a wealth of information about the genomic landscapes of human cancers. At the core of this progress are advances in sequencing technology, such as next-generation sequencing, which have enabled detailed characterization of tumor genetics at the point of care and revealed key genetic mechanisms that drive cancer initiation, evolution, and progression (52). Large-scale cancer genome projects, including The Cancer Genome Atlas (TCGA) and the International Cancer Genome Consortium (ICGC) among others, systematically catalog all mutations in a variety of human cancers. The availability of these resources to the larger cancer research community has already translated to tangible impacts on diagnosis, prognosis, and treatment strategies for patients in the clinic (53). A better understanding of the genes and pathways involved in cancer progression and treatment response has led to routine genomic

profiling, which can dramatically influence clinical outcomes, and is now required for clinical management of a number of tumor types, including gliomas, melanoma, and breast, lung, ovary, and colon carcinomas. The genetic profile of a patient can therefore inform selection of targeted therapy, a practice known as precision cancer medicine. For example, in melanoma patients with BRAF V600 mutations, treatment with RAF and MEK inhibitors can improve survival (54). In this and many other examples, genomics data can provide valuable information for patient-tailored treatment strategies.

While deep analyses of patient data can reveal the presence of key genetic alterations, the bewilderingly large list of mutations in every tumor necessitates systematic, functional approaches to gain a more complete molecular understanding of cancer (55). Probing human cancer cells through systematic genetic perturbations enables assessment of the effects of various genes and pathways on functional cancer cell properties like survival and drug response (56). The power of this systematic genomic approach, referred to as functional genomics, is described in the following section.

1.3.1 Using genomics to understand cancer drug resistance

Genomics is a very powerful tool for understanding cancer drug resistance, which is an inevitable and immense obstacle to the efficacy of precision cancer medicine. Functional genomic approaches can be applied to identify the genetic mechanisms of drug resistance, guiding selection of drug combinations to overcome this resistance.

Functional genomics uses high-throughput, often genome-wide screens to assess the effects of genes and pathways on functional cancer cell properties like survival and therapeutic resistance, which, when used alone or in combination with patient genomics data, can reveal new targets for precision therapy.

Functional genetic screening efforts have revealed the genetic drivers of drug resistance to targeted therapeutic agents with little a priori knowledge of the mechanisms of resistance (57). For example, one study used a targeted short hairpin RNA (shRNA) screen to investigate the problem of resistance to MAP/ERK kinase (MEK)/phosphoinositide 3-kinase (PI3K) inhibitor combinations in KRAS—mutant non-small cell lung cancer. The screen identified BCL-2 family proteins as key regulators of apoptotic response to this drug combination, and concluded that the inability to induce apoptosis may explain inefficacy of the drug combination in lung cancer patients with RAS mutations (58). This and many other functional screening approaches have illuminated a great deal about cancer drug resistance. In the remainder of this section, we provide a brief overview of two important types of functional screens: open reading frame (ORF) gain-of-function screens and CRISPR/Cas9 loss-of-function screens.

1.3.2 Lentiviral ORF gain-of-function screens

An open reading frame (ORF) is the protein-coding region of a DNA sequence. The gain-of-function open-reading frame (ORF) method screens a library of pathway-activating mutant complementary DNAs (cDNAs) to identify pathways that confer

cancer cell resistance to a particular drug. In 2011, Yang and colleagues published a public genome-scale lentiviral expression library of human ORFs (59). This enabled identification of gain-of-function mediators of resistance to drugs of interest through the systematic perturbation of thousands of genes. For example, one study utilized this library to identify genes whose overexpression drive resistance to ALK inhibition in ALK-driven non-small cell lung cancers. The ORFs were introduced into an ALK-dependent lung adenocarcinoma cell line with high sensitivity to ALK inhibition. The ORF-expressing cells were then assessed for sensitivity to ALK inhibitors and over 50 genes were identified as potential drivers of resistance to these inhibitors. This data leads to the nomination of a number of agents, such as EGFR, HER2, or PKC inhibitors, for combination with ALK inhibitors (60). This and other examples demonstrate the value of ORF screens for understanding the functional landscape of drug resistance in cancer, and for identifying drug candidates for overcoming this resistance.

1.3.3 CRISPR/Cas9 knockout screens

Clustered Regularly Interspaced Short Palindromic Repeats (CRISPRs) are short, palindromic repeated DNA sequences found in the genomes of bacteria and archaea. These sequences are the hallmark of the adaptive immune systems of these microorganisms, enabling them to fight against invading viruses. Briefly, the CRISPR sequence is transcribed and processed to generate short RNA molecules that guide an RNA-guided endonuclease called CRISPR-associated protein 9 (Cas9) to the target

sequence in an invading virus, identifying this attacker sequence for a Cas9-mediated double-stranded break. The double-stranded break is repaired in an error-prone manner by nonhomologous end-joining, resulting in short deletion and insertion mutations that can knock out gene function (61). This phenomenon is the basis for CRISPR/Cas9 editing technology, which has recently revolutionized the molecular toolbox for genome engineering (62).

Large-scale pooled functional screens using CRISPR/Cas9 technology can be used in human cancer cells to knock out function of thousands of genes in an unbiased, efficient manner. Previously, RNA interference (RNAi) was used for genome-wide loss-of-function screening, but this method often suffered from unavoidable incomplete protein depletion and confounding off-target effects. These issues are less problematic in CRISPR/Cas9-based screens.

In CRISPR/Cas9 functional screens, a pool of cells co-expressing Cas9 and the sgRNA library are subjected to a particular phenotypic selection, genomic material is extracted and purified from the selected cells and evaluated by high-throughput DNA sequencing of the genes encoding the sgRNAs. These sequencing results are then analyzed for identification of sgRNAs that were enriched or depleted as a result of the specific selection pressure. The development of a genome-scale lentiviral single-guide RNA (sgRNA) library has enabled the precise, complete evaluation of the genetic mechanisms of cancer resistance to targeted inhibitors, and provided valuable insight

into genes that are essential in various cancer cell lines (63, 64). For instance, a recent study identified point mutations in PARP1 as the underlying mechanism of ovarian cancer resistance to poly-(ADP-ribose) polymerase (PARP) inhibitors (65).

1.4 Objectives

The overall goal of this research is the development of a platform that integrates an elegant solution for protein drug delivery with a genomics-based strategy for rationally designed drug combinations that overcome tumor drug resistance. The platform harnesses the power of protein engineering and genomics to (1) generate targeted therapies that do not possess the technical limitations of antibodies, (2) improve drug delivery with precise control over bioavailability and material properties, and (3) rationally formulate drug combinations that block the signaling pathways that control drug resistance (Figure 5).

We have employed a novel multidisciplinary strategy to systematically accomplish these objectives by: (1) utilizing a highly potent, hexavalent death receptor agonist (DRA), (2) developing a gel depot for sustained delivery of the DRA, and (3) leveraging functional genomic screens in DRA-resistant colorectal cancer (CRC) cells to identify functional drivers of resistance and broadly efficacious combination drugging strategies.

In Chapters 2 and 3, we present the protein engineering aspect of this work, describing the production and characterization of the DRA and the development of gel-

like sustained release depot formulations in which DRAs were recombinantly fused to stimulus-responsive elastin-like polypeptides (ELPs). A single injection of the ELP-DRA fusion abolished tumors in DRA-sensitive Colo205 mouse xenografts. In Chapter 4, we leverage an ORF-based gain-of-function screen in a DRA-sensitive colorectal cancer (CRC) cell line and a CRISPR/Cas9 knockout screen in DRA-resistant CRC cells to identify functional drivers of resistance. Follow-up cell viability, time-to-progression, and clonogenic assays showed that pharmacological blockade of XIAP, BCL-X_L, and/or CDK4/6 strongly enhanced the antitumor activity of DRA in both established and patient-derived CRC cell lines. In Chapter 5, we demonstrate that combination therapies involving ELP-DRA plus the BCL-X_L inhibitor A-1331852 and/or the XIAP inhibitor BV6 led to tumor growth inhibition, and extended survival in DRA-resistant patient-derived xenografts (PDX). Finally, in Chapter 6, we discuss the extension and application of this platform to other protein-based therapeutics for cancer therapy, and discuss future directions for integrating the fields of drug delivery and genomics for drug development.

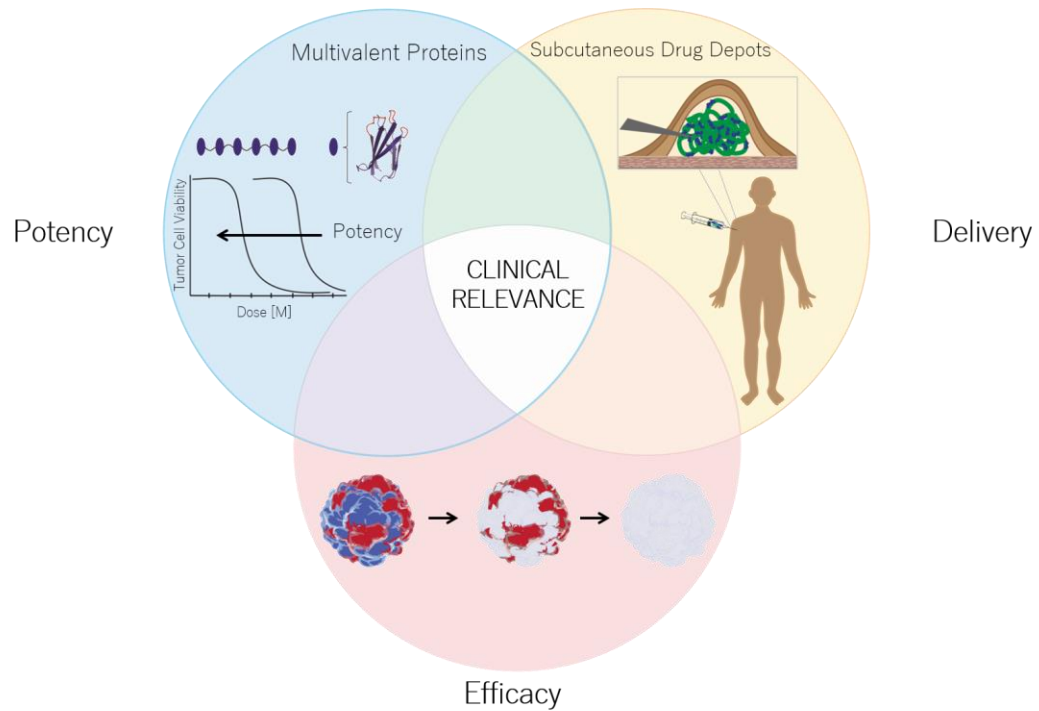


Figure 5: Multidisciplinary platform for cancer drug development.

For clinically translatable cancer drug development, potency, efficacy, and delivery must be simultaneously accounted for. In the context of this dissertation, potency is maximized with multivalent extrinsic pathway agonists, efficacy is maximized with genomic screening to inform rational selection of drug combinations to overcome drug resistance, and delivery is maximized with gel depots for sustained release of protein therapeutics.

2. Design, production, and evaluation of death receptor agonists (DRAs)

2.1 Introduction

For proof-of-concept of our novel drug design and delivery platform, we selected a pro-apoptotic death receptor agonist (DRA), as this class of protein drugs has consistently eluded clinical translation despite preclinical promise. The DRA referred to in this work targets death receptor 5 (DR5). DR5 is a clinically relevant target receptor on the surface of cancer cells, and significantly up-regulated in stage II and III colorectal cancer (CRC), but without prognostic significance (66, 67). Although human CRC cells express detectable levels of DR5, expression levels do not correlate with sensitivity to agonists (67, 68).

Specifically, the DRA is a hexavalent fusion protein composed of six DR5-binding Tn3 domains connected by flexible glycine/serine linkers to create a beads-on-a-string molecule. The DRA has demonstrated sub-picomolar EC_{50} in human cancer cell lines (14). This specific agonist is highly superior to death receptor-specific antibodies in that it can be expressed in *E. coli*, and its multivalency enables higher order receptor clustering. Higher order clustering has been shown to induce stronger signaling in TNF family receptor signaling cascades (11). When compared to TRAIL, the natural ligand for DR5, the DRA exhibits higher receptor binding affinity and increased multivalency, which likely contribute to its superior performance (Figure 6). Despite excellent potency, the DRA is hindered by subpar pharmacokinetics (circulation half-life of 36 minutes)

and therefore requires significant modification for improved tumor delivery and a realistic clinical administration regimen. Furthermore, as with all cancer treatments, tumor resistance is unavoidable, so exploration of these mechanisms and assessment of combination formulations is also imperative. Before addressing the delivery and resistance issues, successful recombinant expression and purification of the DRA was necessary. The purified DRA was then evaluated for potency and compared to TRAIL in a panel of human colorectal cancer cell lines with a range of TRAIL sensitivity (68).

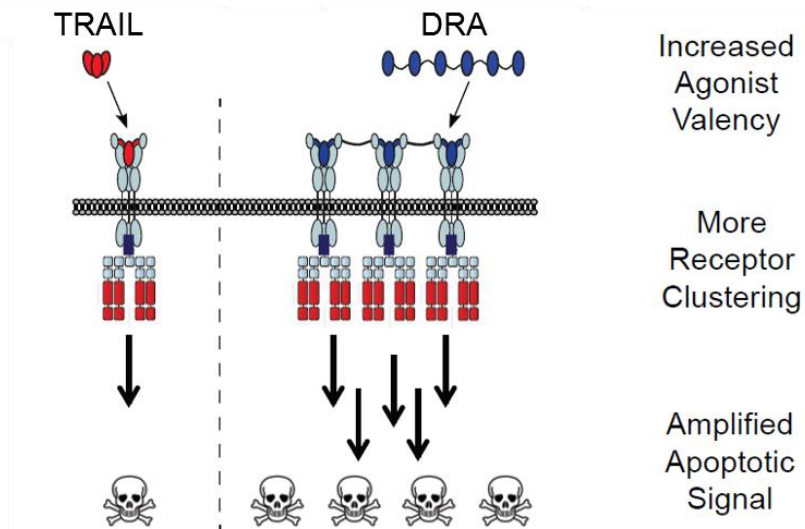


Figure 6: DRA-induced DR5 crosslinking results in potent apoptotic signal.

Binding of homotrimeric TRAIL to death receptors results in receptor trimerization and apoptosis (left). DRA has higher affinity and multivalency in comparison to TRAIL, allowing for more effective DR5 binding, receptor clustering and higher order crosslinking, and an amplified apoptotic signal (right).

2.2 Materials and methods

2.2.1 Molecular biology of construct fusions

The DNA encoding the Tn3 unit in the death receptor agonist (DRA) encoded the amino acid sequence provided in Appendix A. The *E. coli* codon-optimized gene was purchased as a “G-block” from Integrated DNA Technologies (IDT). The gene was purchased with a (Gly₄Ser)₃ linker at the C-terminus and designed with restriction sites compatible with recursive directional (RDL) ligation for seamless cloning of oligomeric genes. The amplified PCR product was purified using a Qiagen PCR cleanup kit and digested with BseRI for insertion into a BseRI/CIP digested pET-24(+) vector modified for RDL (69). The insert and vector were agarose gel-purified and ligated with QuickLigase to clone the single unit construct. This was followed by digestion of the single unit construct (Tn3 in pET24(+)) with BseRI/CIP and ligation with BseRI-digested insert (Tn3 unit) to clone 2, 4, and 6 Tn3 repeats in the pET-24(+) vector. Subcloning efficiency EB5α cells (EdgeBio) were used for cloning steps. All enzymes were purchased from New England Biolabs. For DRA expression without fusion to ELP, a periplasmic secretion signal, oppA (Appendix A) was cloned into the 5' terminus of the DRA gene (Tn3)₆ by the previously discussed RDL method and an eight-histidine tag was cloned to the 3' end to create oppA-DRA-His8. TRAIL-His8 was purchased as a G-block from IDT and cloned into the previously described plasmid system. The plasmids containing the DRA and TRAIL genes were transformed into BL21(DE3) cells for expression.

2.2.2 Expression and purification

The oppA-DRA-His8 construct was then expressed in BL21(DE3) cells: overnight cultures were used to inoculate 1 L shake flasks and cells were grown at 37°C for 4-5 hours, then induced with 1 mM sterile IPTG and incubated in 37°C shaker for another 4-6 hours. Cells were then pelleted and resuspended in 100 mL ice-cold 10 mM Tris 1 mM EDTA pH 8 buffer and placed on a rotator at 4°C for 1-2 hours to complete protein extraction from periplasmic space. The periplasm extraction samples were then centrifuged at 14000 rpm for 15' at 4°C to pellet cell debris. Proteins in solution were precipitated with ammonium sulfate (60% weight/volume) and centrifuged for 15' to pellet the precipitated protein. Protein pellet was then placed on ice and resuspended in ice-cold PBS. Nickel-NTA agarose resin was then used to purify His-tagged DRA from other periplasmic proteins (manufacturer's protocol, Thermo Fisher Scientific). Pure eluate then underwent buffer exchange into 20 mM Tris 300 mM Arginine pH 7 using 10 kDa Amicon Ultra centrifugal filters (EMD Millipore). A summary of the purification process is shown in Figure 7.

DRA-His_s was analyzed by size exclusion chromatography by ÄKTA Superdex HiLoad 26 60/200 in PBS, and MALDI-TOF mass spectrometry using an Applied Biosystems Voyager-DE Pro system fitted with a nitrogen laser. Results were obtained using α -Cyano-4-hydroxycinnamic acid matrix in a 20:1 (v/v) ratio with the analyte.

2.2.3 Evaluation of extrinsic pathway gene expression

Immunoblotting. DR5 expression was confirmed in a panel of human colorectal cancer cell lines. Cell lysate was obtained from cultured cell lines, and protein content was quantified by BCA assay. Equal amounts of protein from each cell lysate were run on SDS-PAGE, after which the gel was transferred to a PVDF membrane for immunoblot analysis. The membrane was incubated with primary antibodies against DR5 and GAPDH loading control, followed by incubation with a secondary, Dylight650 fluorophore-conjugated detection antibody. The fluorescent blot was imaged using a Typhoon laser scanning instrument.

Gene expression analysis. mRNA expression data was obtained from CCLE for three DRA resistant and six DRA sensitive CRC cell lines. A heat map was created to visualize the data for expression of eight pro-apoptotic and five anti-apoptotic proteins and one control (CFLAR) gene in each cell line.

2.2.4 Cell Lines and Cytotoxicity assays

All cell lines were grown at 37°C in 5% CO₂. Colo205 were cultured in RPMI (10% FBS, HEPES, pyruvate, 1% Pen/Strep (P/S)). HCT116 and HT29 were cultured in

McCoy's (10% FBS, 1% Pen/Strep). RKO were cultured in MEM Earle's (10% FBS, pyruvate, NEAA, 1% P/S). Lovo were cultured in F-12K (10% FBS, 1% P/S). T84 were cultured in 50/50 mix of HAM's F-12 and DMEM (2.5 mM L-glutamine, 5% FBS, 1% P/S). Colo320HSR, DLD-1, and HCT-15 were cultured in RPMI (10% FBS, 1% pen/strep). All cell lines were purchased within 6 months from Duke CCF or ATCC and patient-derived lines were obtained from David Hsu (Duke University) and passaged less than 10 times. All cell lines were authenticated using Promega PowerPlex 18D kit for short tandem repeat (STR) analysis or were purchased within 6 months from Duke CCF. All cell lines were tested for mycoplasma by Duke CCF. FBS: fetal bovine serum (GIBCO); P/S: penicillin/streptomycin (Thermo Fisher). Media was purchased from GIBCO or Sigma Aldrich.

For cytotoxicity evaluation, DRA or TRAIL proteins were tested *in vitro* using a colorimetric formazan assay (MTT) as follows. The cells were plates in 96 well plates at a density of 2,000-10,000 cells/well in 90 μ L of complete media (RPMI 1640+10% FBS) and incubated for 1-18 hours at 37°C with 5% CO₂. The cells were then treated with 10 μ L additional media containing a serial dilution of the drug(s) of interest. The treatments were done in triplicate to account for technical variability. After 18-20 hours, the Promega CellTiter 96 Aqueous One Solution Reagent G3581 kit was used according to manufacturer's instructions to assay the number of viable cells; it is an accepted method. The inhibition of cell viability was determined using measurements of the

absorbance at 490, the absorbance maximum of the formazan product. The dose response curves were generated by plotting inhibition v. compound concentration. The dose response curve was approximated from the scatter plot using a four-parameter logistic model calculation, and EC50 was calculated as the concentration of drug required to kill 50% of the cells.

2.3 Results and discussion

2.3.1 Protein expression and characterization

Expression and purification of the DRA required a great deal of optimization. The challenge of producing this protein was due largely to the disulfide bond in each domain of the hexavalent DRA. Expression in the reducing environment of the *E. coli* cytoplasm resulted in misfolding and aggregation due to formation of intermolecular disulfide bonds. To address this issue, we introduced a periplasmic secretion signal to the N terminus of the DRA. This secretion signal, a short peptide called oppA, promotes secretion of the protein to the oxidizing environment of the *E. coli* periplasm, located between the inner and outer membrane of the bacteria (Figure 8) (70). SDS-PAGE for purified DRA and TRAIL and mass spectrometry data for DRA are shown in Figure 9.

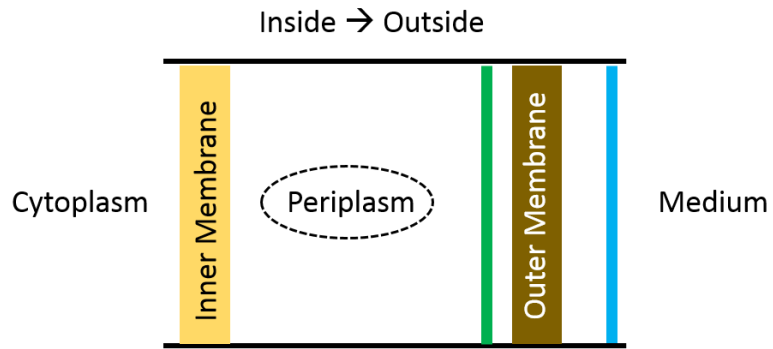


Figure 8: Periplasm of *E. coli*, located between the inner and outer membranes.

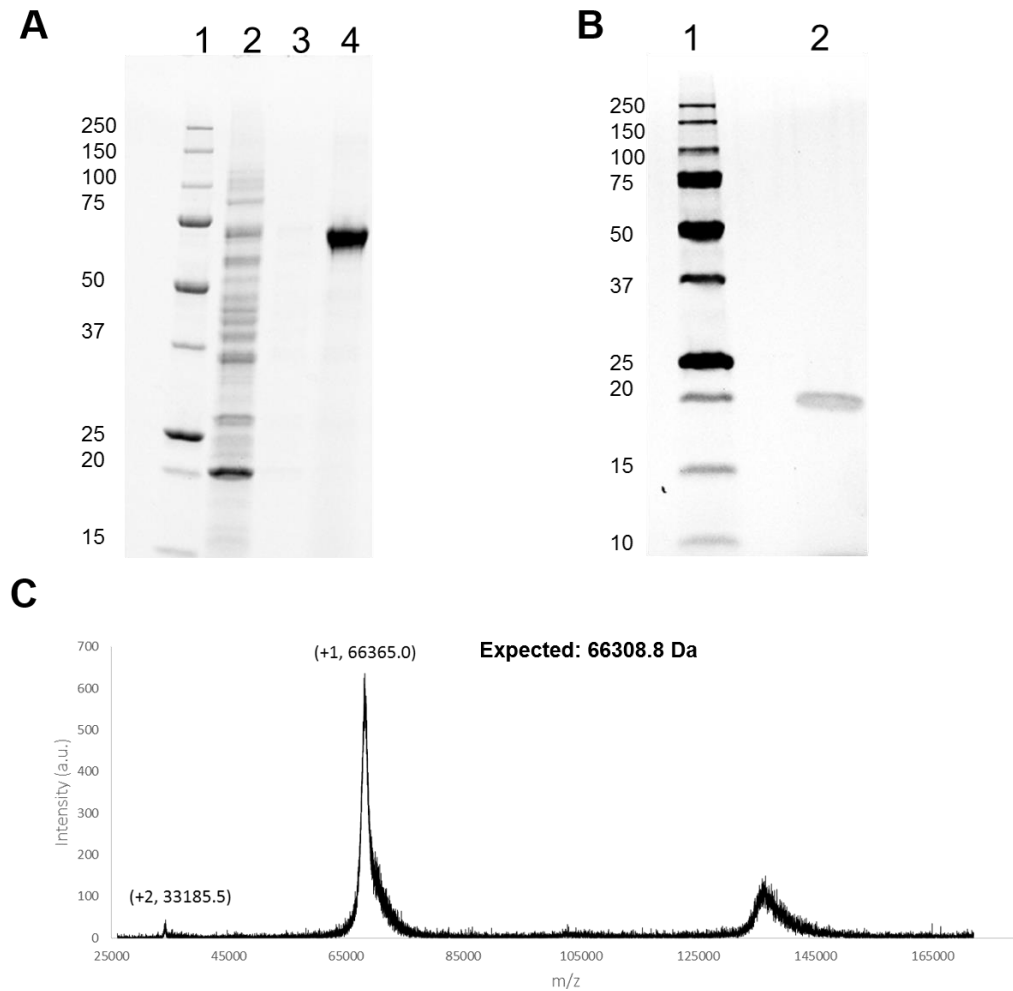


Figure 9: Protein characterization of DRA and TRAIL.

(A) SDS-PAGE of DRA-His₈ purified from *E. coli* periplasmic space. Lanes: #1 Precision Plus Unstained Protein Standards (markers are labeled to the left in kDa), #2: Flow-

through fraction from Ni-NTA agarose resin purification, #3 wash fraction, #4 pure DRA eluate at about 66 kDa. (B) SDS-PAGE of TRAIL- His₈ purified from *E. coli* cell lysate using Ni-NTA agarose resin purification. Lanes: #1 Precision Plus Unstained Protein Standards, #2: pure TRAIL eluate at about 21 kDa. (C) MALDI-TOF mass spectrum of purified DRA-His₈ shows peaks that correspond to ions arising from the full-length protein at the +1 charge state ($m/z=66365$) and the +2 charge state ($m/z= 33185.5$). Expected molecular weight is 66308.8 Da.

2.3.2 Evaluation of extrinsic pathway gene expression

Although the level of DR5 expression is not indicative of cell line sensitivity to proapoptotic DR5 agonists, the presence of DR5 is required for DRA activity. Thus, DR5 expression was confirmed by immunoblotting in a panel of human colorectal cancer (CRC) cell lines before testing of TRAIL and DRA by cytotoxicity assays (Figure 10). A collection of known TRAIL-sensitive cell lines (i.e. DLD-1, Colo205, HCT116, HCT15) and TRAIL-resistant cell lines (i.e. HT29, Colo320HSR, Lovo, RKO) were compared.

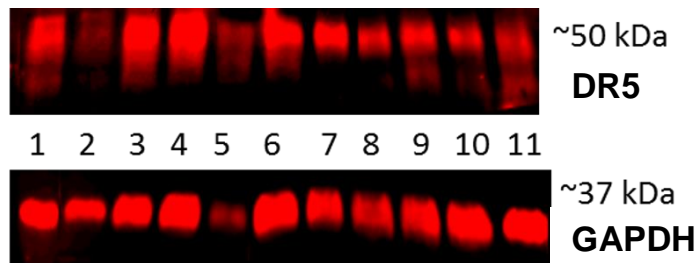


Figure 10: Anti-DR5 immunoblot confirms DR5 expression in panel of human colorectal cancer cell lines.

DR5 expression and drug sensitivity in a panel of human colon cancer cell lines. Lanes correspond to 1: DLD-1, 2: Colo205, 3: HCT116, 4: HT29, 5: Colo320HSR, 6: HCT15, 7: T84, 8: SW948, 9: RKO, 10: CaCO-2, 11: LoVo.

DRA sensitivity and resistance could not be trivially explained by differential expression of individual genes in the extrinsic and intrinsic apoptotic pathways, as mRNA expression data from the Cancer Cell Line Encyclopedia (CCLE) revealed no significant differences in the expression of these genes (Figure 11). These results are consistent with a large body of literature suggesting that cancer cell resistance to TRAIL and other pro-apoptotic drugs cannot be easily explained by simple analyses of differential gene expression (37).

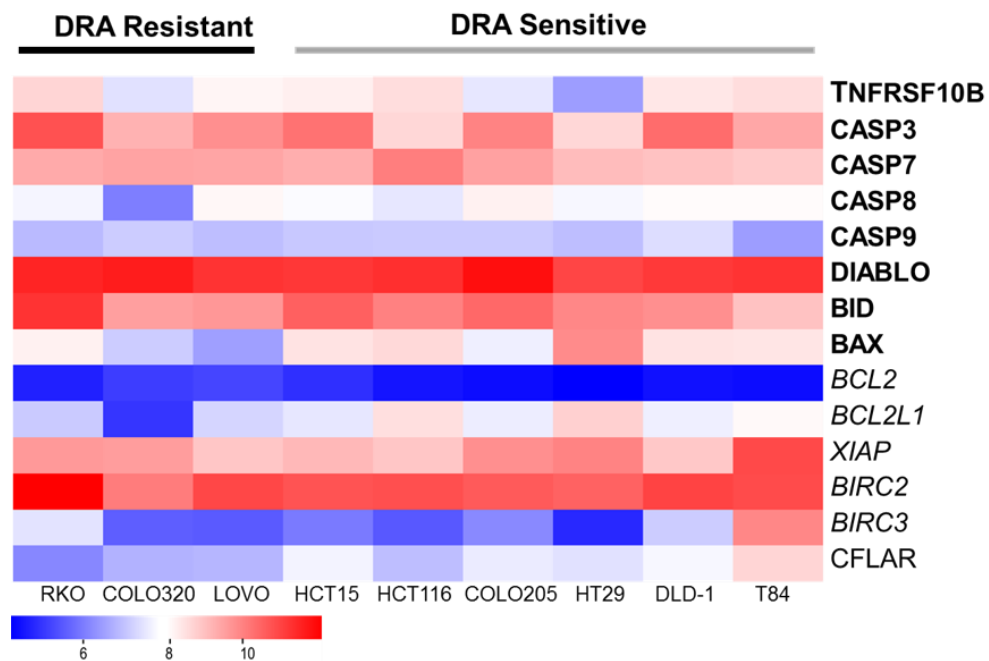


Figure 11: TRAIL sensitivity cannot be explained by differential expression of extrinsic pathway proteins.

mRNA expression data was obtained from CCLE for three DRA resistant and six DRA sensitive CRC cell lines. A heatmap was created to visualize the data for expression of eight pro-apoptotic (**bold**) and five anti-apoptotic proteins (*italic*) and one control (CFLAR) gene in each cell line.

2.3.3 Cytotoxicity results

Once size and purity of the DRA were confirmed, its potency was assessed in a panel of human colorectal cancer cell lines with a range of TRAIL sensitivities (68). As measured by MTT cell cytotoxicity assays, the hexavalent DRA demonstrates EC_{50} in the picomolar range in all tested TRAIL-sensitive cell lines and is maximally over one thousand times more potent than TRAIL (Fig. 12A, C, D, E). DRA can also demonstrate cytotoxicity in partially (Figure 12F, G) or completely TRAIL-resistant cell lines (Figure 12B), suggesting that, in some instances, TRAIL resistance is driven by inefficient receptor clustering. However, despite the drastically improved potency offered by the hexavalent DRA, certain cell lines, such as RKO (Figure 12H), remained resistant to the DRA ($EC_{50} > 100$ nM) (68), suggesting additional intrinsic resistance mechanisms.

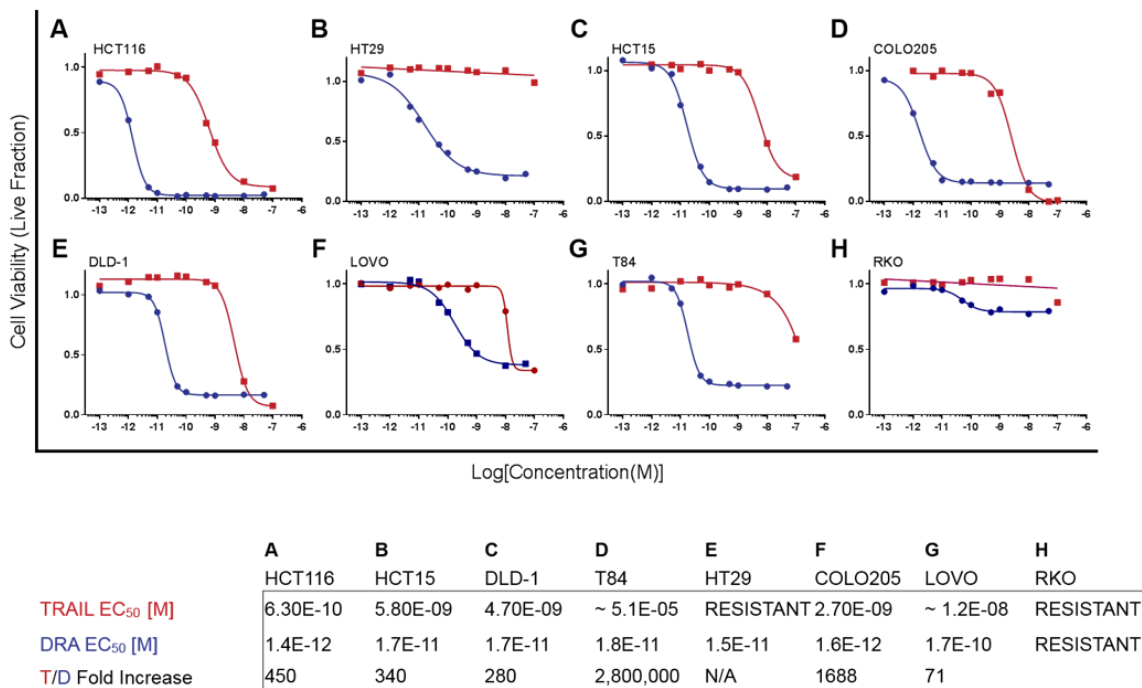


Figure 12: Cytotoxicity dose-response curves for TRAIL and DRA in human colorectal cancer cell lines.

Cell lines with an EC₅₀>100 nM were deemed resistant. (A, C, D, E) DRA is at least 2 orders of magnitude more potent in TRAIL-sensitive cell lines HCT116, HCT15, Colo205, and DLD-1 respectively. (B, F, G) DRA induces cytotoxicity in TRAIL-resistant cell line HT29 as well as partially-resistant LoVo, and T84. (H) TRAIL-resistant RKO is also resistant to DRA. Table indicates EC₅₀ of each drug for each cell line and the increase in potency (fold change) of DRA compared to TRAIL.

2.3.4 Apoptotic competence of DRA-resistant cancer cells

Differential DRA responses were unrelated to apoptotic competence, as DRA-resistant cell lines were capable of undergoing apoptosis by treatment with the topoisomerase inhibitor etoposide for 48 hours, as indicated by annexin V binding assays in two intrinsically resistant cultures, the established cell line, RKO, and low-passage patient-derived line, CRC247 (Figure 13).

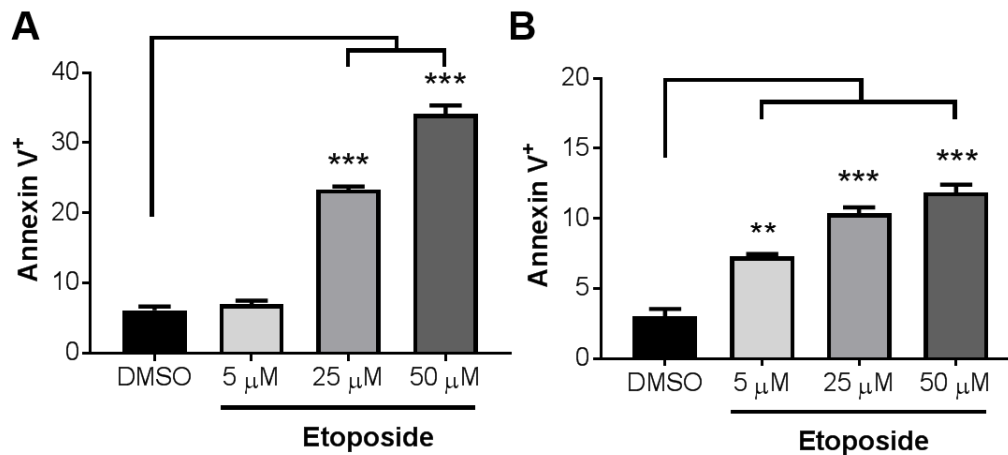


Figure 13: DRA-resistant human CRC cells can undergo apoptosis.

(A) Percent RKO cells positively stained for Annexin V after treatment with etoposide for 48 hours. Annexin V binding to DMSO control treated cells is statistically significantly different from treatment with 25 or 50 μ M etoposide. (B) Percent CRC247 cells positively stained for Annexin V after treatment with etoposide for 48 hours. Annexin V binding to DMSO control treated cells is statistically significantly different from treatment with 5, 25 or 50 μ M etoposide. ** p=0.001, *** p=0.0001.

2.4 Significance

In Chapter 2, we presented the optimized purification method, product characterization data, and *in vitro* potency of the DRA. These studies replicated the results from Swers and colleagues, and provided further evidence that the hexavalent DRA has maximal apoptotic potency, likely through promotion of multimeric receptor crosslinking and optimized pathway engagement. Without this information, the DRA could not be further utilized as a model protein for our delivery and drug combination platform.

We also demonstrated that TRAIL sensitivity cannot be explained simply by differential gene expression of extrinsic pathway proteins. Notably, we further showed that DRA resistance cell lines retain functional machinery for apoptosis. Together, these data motivate the use of a CRISPR/Cas9 knockout screen to identify functional drivers of DRA resistance.

In summary, the results in this chapter confirm (1) activity of the DRA, (2) superior cytotoxicity of DRA in comparison to TRAIL, and (3) presence of DRA-resistant colorectal cancer cells. In the following two chapters, we systematically address the issues of delivery and resistance that hinder DRA efficacy.

3. Engineering ELP-DRA fusions for *in vivo* sustained release

3.1 Introduction

As suggested by the discussion of the pitfalls of TRAIL in the clinic, optimization of a targeted protein's potency dramatically improves its anticancer efficacy, but if unaddressed, inadequate drug delivery can still prevent clinical translation. In the case of the super-potent multivalent death receptor agonist (DRA) used in our studies, the short half-life (approximately 36 minutes) necessitates daily injections for *in vivo* efficacy (14). Since proteins must be injected, the need for chronic outpatient therapy and reduced patient compliance diminish their appeal when compared to small molecule drugs (71, 72). Improving delivery of protein therapeutics is crucial to reduce injection frequency and improve clinical feasibility. In this study, we aimed to develop a sustained release formulation of the DRA that demonstrated antitumor efficacy *in vivo* after a single injection.

Our delivery method utilizes elastin-like polypeptides (ELPs), a versatile class of stimulus-responsive biopolymers. ELPs are repetitive polypeptides comprised of repeats of the pentapeptide sequence VPGXG, where guest residue X is any amino acid except proline (47). These biopolymers exhibit inverse temperature phase transition- they are soluble below their inverse transition temperature (Tt) and aggregate into an insoluble gel-like "coacervate" phase above the Tt (73, 74). Importantly, this phase transition is

reversible, such that the coacervate can be resolubilized when the temperature is lowered again below the T_t . Although synthetic polymers such as poly(N-isopropylacrylamide) (PNIPAAm) exhibit similar inverse temperature phase transition behavior, ELPs provide some key advantages over such polymers. Specifically, ELPs are genetically encoded polypeptides, enabling precise control over properties such as chain length and T_t through manipulation of sequence length and identity of the guest residue. Moreover, ELPs can be easily appended to therapeutic proteins of interest through recombinant DNA methods, and these fusions retain the thermal responsiveness of the attached ELP. The biocompatibility and lack of toxicity of ELPs are also advantageous for *in vivo* applications (47, 75).

ELP fusion to therapeutic proteins increases overall molecular size, and can improve protein pharmacokinetics and biodistribution. ELP attachment to some proteins can drive self-assembly into nano-scale micelles optimal for drug delivery into solid tumors (76, 77). For prolonged residence of therapeutic proteins and sustained release into the circulation, ELP fusions can be tuned to aggregate into gel-like depots at physiological temperatures, such that the formulation is soluble in the syringe, and transitions upon subcutaneous injection (Figure 14) (50, 51). The ELP protein fusion slowly diffuses from the depot, enabling sustained release over time (78).

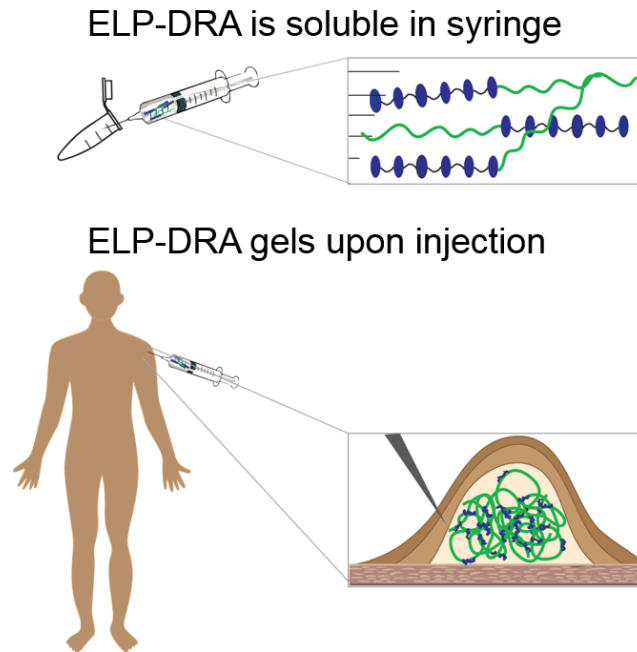


Figure 14: Fusion of thermally responsive ELPs to death receptor agonists enables depot formation for sustained release.

We hypothesized that by fusing elastin-like polypeptide (ELP) biopolymers to the DRA, the advantages of polymer conjugation could be integrated with the unique characteristics of these protein-based thermally responsive polymers to generate gel depots for slow release of the DRA. To test this hypothesis, we first designed, purified, and characterized an ELP-DRA fusion that could be effectively formulated for depot formation. We then tested the fusion *in vivo* to evaluate its antitumor efficacy.

3.2 Materials and methods

3.2.1 ELP-DRA fusion molecular biology

The genes for ELP (VPGVG)₆₀, depot-forming ELP (VPGVG)₁₂₀, or soluble ELP (VPG[A/G]G)₁₂₀ were recombinantly fused to the Tn3s using plasmid reconstruction recursive directional ligation (pre-RDL) (69). The recursive directional ligation method for this particular vector called for digestion of the oligomerized Tn3 in modified pET24(+) with *AcuI* and *BglII*, and digestion of ELP in pET24(+) with *BseRI* and *BglII*. The digested fragments of DNA were separated using agarose gel electrophoresis, and the DNA bands at the appropriate molecular weights were excised and gel-purified. The resulting fragments were ligated using *QuickLigase* and successful clones were obtained. The restriction digest scheme mentioned refers to fusion of ELP to the C-terminus of the multimeric agonist, but the scheme was flipped if N-terminal fusion was desired.

3.2.2 ELP-DRA fusion purification

The multivalent depot-forming ELP-DRA fusion constructs were expressed in SHuffle T7 Express cells (New England Biolabs) in 2XYT media in 1 L shake flasks. Overnight cultures were used to inoculate the 1 L shake flasks and cells were grown shaking at 200 rpm at 30°C for 4-5 hours, then induced with 1 mM sterile IPTG and incubated at 25°C for another 6-12 hours. Cells were pelleted, resuspended in 50 mM Tris pH 8, sonicated, and centrifuged at 4°C to separate cell debris from the soluble

fraction. Proteins were purified from the cell lysate using inverse transition cycling (ITC), which requires repeated cycles of protein precipitation and solubilization. Specifically, the “hot spin” of ITC was performed by addition of <2 M ammonium sulfate until the solution became opaque and salt was fully dissolved and centrifuged at 14000 rpm at 35°C for 20 minutes to pellet the protein. The transitioned protein pellet was then resuspended in 20 mM Tris, 300 mM Arginine pH 7 and placed in a rotator at 4°C. The “cold spin” of ITC was performed by centrifuging the protein and preserving the supernatant, which contained the ELP-DRA fusion. The hot spin/cold spin process was repeated before further purification by size exclusion chromatography by ÄKTA Superdex HiLoad 26 60/200 in PBS. Pure eluate then underwent buffer exchange into 20 mM Tris 300 mM Arginine pH 7 using 10 kDa Amicon Ultra centrifugal filters (EMD Millipore). All purified proteins were analyzed by SDS-PAGE on Biorad Mini-PROTEAN TGX Tris-HCl Stain-Free gels for correct molecular weight bands.

The multivalent soluble oppA-ELP-DRA-His₈ fusion constructs were expressed in BL21(DE3) cells in 2XYT media in 1 L shake flasks (New England Biolabs). Overnight cultures were used to inoculate the 1 L shake flasks and cells were grown at 37°C for 4-5 hours, then induced with 1 mM sterile IPTG and incubated in 37°C shaker for another 6-12 hours. Cells were then pelleted and resuspended in 100 mL ice-cold 10 mM Tris 1 mM EDTA pH 8 buffer and placed on a rotator at 4°C for 1-2 hours to complete protein extraction from periplasmic space. The periplasm extraction samples were then

centrifuged at 14000 rpm for 15' at 4°C to pellet cell debris. Proteins in solution were precipitated with ammonium sulfate (60% weight/volume) and centrifuged for 15' to pellet the precipitated protein. Protein pellet was then placed on ice and resuspended in ice-cold PBS. Nickel-NTA agarose resin was then used to purify His-tagged soluble ELP-DRA from other periplasmic proteins (manufacturer's protocol, Thermo Fisher Scientific). Pure eluate then underwent buffer exchange into 20 mM Tris 300 mM Arginine pH 7 using 10 kDa Amicon Ultra centrifugal filters (EMD Millipore).

3.2.3 Dynamic light scattering

Dynamic light scattering (DLS) was performed on the purified depot-forming ELP-DRA construct to measure the radius of particles in our sample as a function of temperature. Sharp increases in reported R_h at a given temperature are indicative of nanoparticle assembly. DLS data collection examined the behavior of the hydrophobic ELP-DRA fusion suspended in Tris/Arg buffer. 200 μ L of the depot-forming ELP-DRA in Tris/Arg (concentration: 10 μ M, filtered through a 0.2 μ m Whatman Anotop sterile syringe filter) was loaded into the Wyatt DynaPro temperature-controlled microsampler in a 12 μ L quartz crystal cuvette (Wyatt Technology, Santa Barbara, CA). Measurements were taken as the sample was heated in 5°C increments from 20°C to 55°C. Acquisition time was set to 20 seconds, and 5 data acquisitions were taken for each recording temperature. Error bars represent the polydispersity percentage determined from these 5 data points at each temperature.

3.2.4 ELP-DRA optical turbidity

To evaluate the transition temperature (Tt) of the ELP-DRA fusion proteins, a spectrophotometer was used to slowly heat 25 μ M solution of the proteins (by 1°C/minute) and measure the optical turbidity at 350 nm. A sharp transition is indicated by the sudden increase in absorbance, and the inflection point of the absorbance by temperature curve is used to calculate the Tt.

3.2.5 ELP-DRA fusion *in vitro* testing

All cell lines were grown at 37°C in 5% CO₂. Colo205 were cultured in RPMI (10% FBS, HEPES, pyruvate, 1% Pen/Strep (P/S)). FBS: fetal bovine serum (GIBCO); P/S: penicillin/streptomycin (Thermo Fisher). Media was purchased from GIBCO or Sigma Aldrich.

For cytotoxicity evaluation, all ELP-DRA proteins were tested *in vitro* using a colorimetric formazan assay (MTT) as follows. The cells were plates in 96 well plates at a density of 2,000-10,000 cells/well in 90 μ L of complete media (RPMI 1640+10% FBS) and incubated for 1-18 hours at 37°C with 5% CO₂. The cells were then treated with 10 μ L additional media containing a serial dilution of the drug(s) of interest. The treatments were done in triplicate to account for technical variability. After 18-20 hours, the Promega CellTiter 96 Aqueous One Solution Reagent G3581 kit was used according to manufacturer's instructions to assay the number of viable cells; it is an accepted method. The inhibition of cell viability was determined using measurements of the

absorbance at 490, the absorbance maximum of the formazan product. The dose response curves were generated by plotting inhibition v. compound concentration. The dose response curve was approximated from the scatter plot using a four-parameter logistic model calculation, and EC₅₀ was calculated as the concentration of drug required to kill 50% of the cells.

3.2.6 Tumor regression analysis *in vivo*

All tumor studies were completed in athymic nude/nude female mice 5-7 weeks old (Jackson Labs). Colo205 engraftment was performed by subcutaneous injection of 1x10⁶ cells in the right flank. Colo205 xenografted mice were treated with one single injection on Day 0. In the pilot study, treatment was administered when tumor size reached approximately 80-120 mm³ (as measured by digital caliper and calculated as LxWx0.5). In the main study, treatment was administered when tumor size reached approximately 150 mm³. All mice were monitored daily to ensure weight loss did not occur beyond 15%; mice were also evaluated for general body condition and mobility. Mice were monitored for visible distress and unacceptable (>15%) weight loss.

3.3 Results and discussion

3.3.1 Design of ELP fusions to death receptor-binding domains

The hexavalent DRA is a repetitive fusion of a Tn3 scaffold-based death receptor-binding domain (14). The monovalent and bivalent fusions are not bioactive due to insufficient valency for death receptor 5 (DR5) homotrimerization, which is required for

apoptotic signaling (11). To ensure that these characteristics of DR5-binding domain fusions were maintained upon ELP fusion, we designed a collection of ELP-(Tn3)_x fusions, in which x refers to the number of Tn3 domains in the fusion (Figure 15a). Between each Tn3 fusion, we inserted a flexible glycine/serine linker. Initially, we chose a hydrophobic ELP, with the sequence (VPGVG)₆₀ because the T_t of this ELP is approximately 35°C at 25 μM. We surmised that if fusion of this 25 kDa carrier polypeptide does not significantly alter the bioactivity of the appended DRA, then this drug delivery approach is viable. Each ELP-(Tn3)_x fusion was recombinantly expressed in *E. coli*.

Fusions of the hydrophobic 60-repeat VPGVG to bivalent and tetravalent repeats of the DR5 domain resulted were designed and expressed in *E. coli*. Each Tn3 domain contains a cysteine, and expression of these fusions in the reducing conditions of the *E. coli* cytoplasm likely contributed to some aggregation, as seen in SDS-PAGE (Figure 15b). The ELP fusion to the bivalent Tn3 protein (ELP-(Tn3)₂) had no effect on cell viability over a range of concentrations in human colorectal cancer cell (CRC) line Colo205 (Figure 15c). This is due to the fact that DR5-induced apoptosis requires homotrimerization of the receptor, which is not achievable with a bivalent DR5-binding fusion. However, as expected, the ELP fusion to the tetravalent Tn3 protein (ELP-(Tn3)₄), demonstrated proapoptotic bioactivity, with EC₅₀ in the picomolar range when tested in Colo205s (Figure 15). While multivalent Tn3 protein activity was retained upon ELP

fusion, the Tn3 domains increased the Tt of the hydrophobic (VPGVG)₆₀ above physiological range, thus prompting the design of fusions to a larger VPGVG chain with a lower Tt. While the bivalent and tetravalent Tn3 repeat fusions were useful as proof-of-concept for these ELP fusions and validated previous bioactivity studies, the hexavalent chains demonstrate maximal pro-apoptotic activity, and are the focus of the remainder of this chapter.

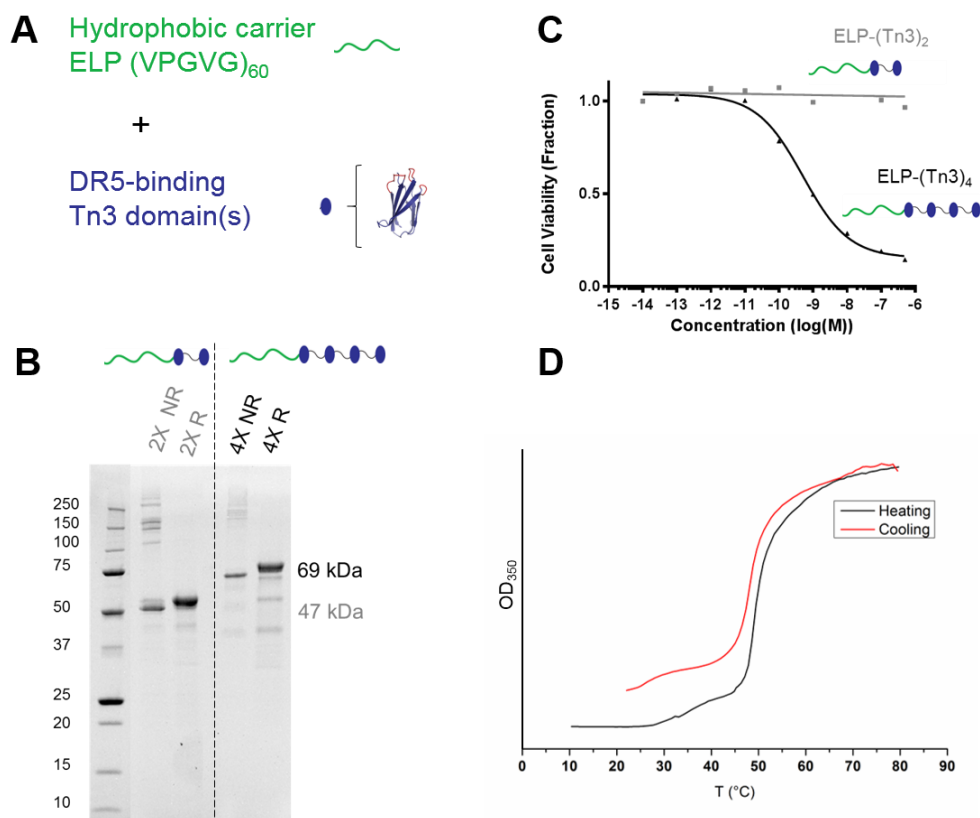


Figure 15: Fusion of thermally responsive ELPs to bivalent and tetravalent DR5-binding Tn3 domains.

(A) A hydrophobic ELP is recombinantly fused to DR5-binding Tn3 domain(s). (B) SDS-PAGE of purified ELP-(Tn3)₂ and ELP-(Tn3)₄. NR: non-reducing; R: reducing agent. (C) Cell cytotoxicity assay demonstrates cytotoxic activity of ELP-(Tn3)₄ compared to inactive ELP-(Tn3)₂. (D) Optical turbidity assay demonstrates phase transition of ELP-(Tn3)₄ at approximately 50°C.

3.3.2 Purification of ELP-DRA

After establishing the feasibility of ELP fusion to Tn3s, we focused on designing ELP fusions to the hexavalent DRA, the most potent of the multivalent Tn3 fusions. Specifically, we synthesized DRA fusions to a hydrophobic ELP (VPGVG)₁₂₀ for depot formulation, and for a non-depot-forming molecular weight control, a hydrophilic ELP (VPGXG)₁₂₀ where X alternates between A and G (Figure 16A). Although the purification method for the hydrophilic ELP-DRA fusion was similar to the previously established approach for the DRA, the purification method for the hydrophobic ELP-DRA fusion proved much more difficult. The reasons for these purification challenges are twofold: (1) the DRA contains a disulfide bond in each of its six DR5-binding domains, and the reducing environment of the *E. coli* cytoplasm is not conducive to correct folding and disulfide formation; (2) the hydrophobic ELP does not traverse easily to the periplasmic space, even when directed by the oppA secretion signal.

Table 1 provides a summary of the various approaches for purification of the hydrophobic ELP-DRA fusion and the most effective purification scheme is described in Figure 16B. This scheme requires the use of Shuffle T7 express *E. coli* which have been engineered to enhance protein folding and disulfide bond formation. Since hydrophobic ELPs with low transition temperature (T_t) can easily transition upon addition of salt or heat, they can be used as purification tags for the attached bioactive protein. Upon addition of salt or heat, the ELP fusion transitions to form an insoluble coacervate that can be separated from the liquid phase by centrifugation. This is referred to as the “hot

spin". The coacervate can then be resuspended in buffer and cooled below its Tt, taking advantage of the reversibility of the phase transition. Contaminant proteins remain insoluble and can be separated from the resolubilized ELP fusion by centrifugation in a process referred to as the "cold spin". A final purification step involves size exclusion chromatography to remove remaining higher molecular weight aggregates. Figure 16C presents data demonstrating purity of the hydrophobic depot-forming ELP-DRA by SDS-PAGE and a chromatogram of the 100 μ M final product validates purity by size exclusion chromatography.

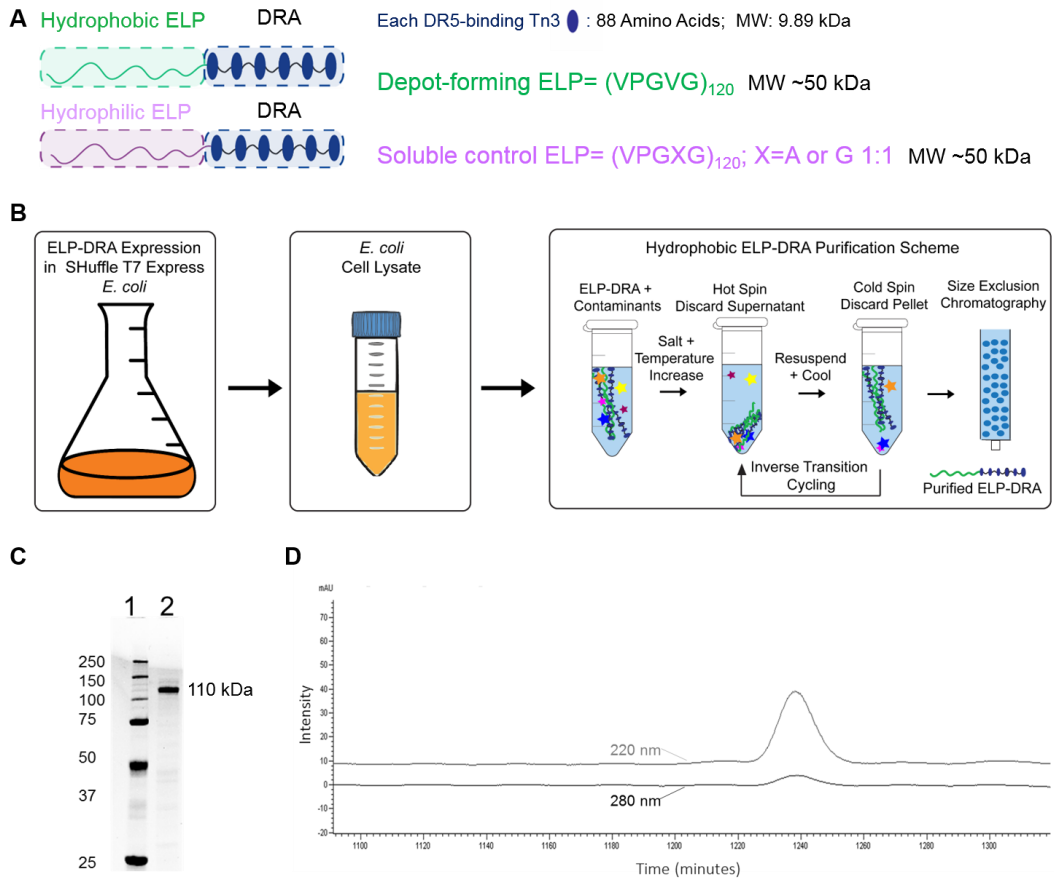


Figure 16: Schematic of ELP-DRA fusion purification and final product.

(A) The hydrophobic ELP and hydrophilic ELPs selected for DRA fusion are approximately 50 kDa and used for depot formation and soluble control respectively. (B) The depot-forming ELP-DRA fusion protein must be expressed in Shuffle T7 express *E. coli*, and protein is purified from cell lysate by inverse transition cycling and size exclusion chromatography. (C) SDS-PAGE of the purified depot-forming ELP-DRA. (D) Size exclusion chromatography confirms protein purity and absence of large aggregates. Absorbance curves are 220 nm (top) and 280 nm (bottom).

Table 1: Summary of expression and purification approaches for depot-forming ELP-DRA fusion.

Expression and Purification	Motivation for Strategy	Product Properties
Expression in BL21(DE3) <i>E. coli</i> strain and purification by inverse transition cycling	ELP can be used as a purification tag	Free of contaminants but high molecular weight aggregates likely due to mispairing of cysteines
Signaling to periplasm of BL21(DE3) <i>E. coli</i> strain, and purification by inverse transition cycling	Secretion to non-reducing environment of periplasm can promote proper disulfide formation	Free of contaminants but very low yield presents a major challenge
Signaling to periplasm of BL21(DE3) <i>E. coli</i> strain, addition of reducing agent, and purification by inverse transition cycling	Addition of reducing agent enables separation of aggregates that have occurred due to mispairing of cysteines.	Free of contaminants but <i>in vitro</i> pro-apoptotic potency of the product is reduced. Properly formed disulfide bonds promote structural stability of each domain.
Expression in Shuffle T7 express <i>E. coli</i> strain followed by purification by inverse transition cycling	Shuffle T7 express strain has enhanced capacity to correctly fold proteins with multiple disulfide bonds within the cytoplasm and expresses a disulfide bond isomerase (DsbC) to promote the correction of mispaired proteins.	Free of contaminants but approximately 10% higher molecular weight aggregates remain.

Expression in Shuffle T7 express E. coli strain followed by purification by inverse transition cycling and size exclusion chromatography	Same as above but added step of size exclusion chromatography to remove remaining high molecular weight aggregates and any truncation products	Free of contaminants and aggregates. Purest product at highest yield (2-3 mg/L).
--	--	--

3.3.3 Characterization and depot formulation of ELP-DRAs

ELP-DRA fusions were purified as discussed in the previous section and tested for bioactivity in cell cytotoxicity experiments. Both the soluble and depot-forming ELP-DRAs are highly cytotoxic in in DRA-sensitive Colo205 human CRC cells, with an EC₅₀ of approximately 1 pM; (Figure 17).

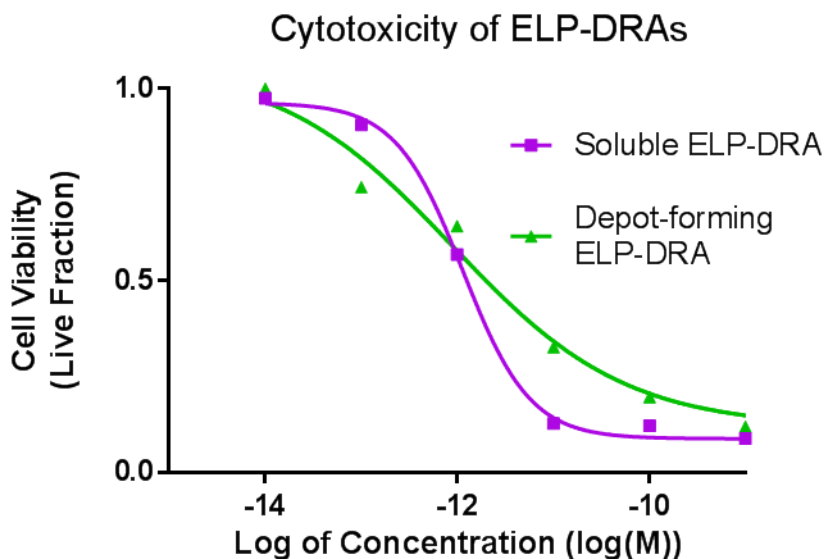


Figure 17: ELPs fusion to the DRA does not affect DRA potency in cytotoxicity assays.

The hydrophobic ELP and hydrophilic ELPs selected for DRA fusion do not affect the DRA's potency in human colorectal cancer cell line Colo205. The EC₅₀ of these fusions is approximately 1 pM.

Once the bioactivity of the ELP-DRA fusions was established, the transition temperature (T_t) of the proteins were evaluated by spectrophotometry. The hydrophilic ELP-DRA, chosen for molecular weight-controlled comparison to the hydrophobic ELP-DRA fusion, has a high transition temperature ($T_t > 50^\circ\text{C}$), so it was soluble at physiological temperature (Figure 18). The hydrophobic ELP (VPGVG)₁₂₀-DRA, however was selected because the free ELP (no DRA) is characterized by a T_t at approximately 28.6°C . This range is ideal, as it is above room temperature (25°C) and below body temperature (37°C), enabling formation of a depot upon subcutaneous injection. The presence of the DRA, however, significantly impacted the transition temperature of the hydrophobic ELP, such that a full transition did not occur at physiological temperature for this fusion (Figure 18). We observed that a mixture of the hydrophobic ELP-DRA with the free hydrophobic ELP at a 1:1 molar ratio resulted in the formation of a mixed depot of ELP-DRA and free ELP that transitions at approximately 30°C (Figure 18).

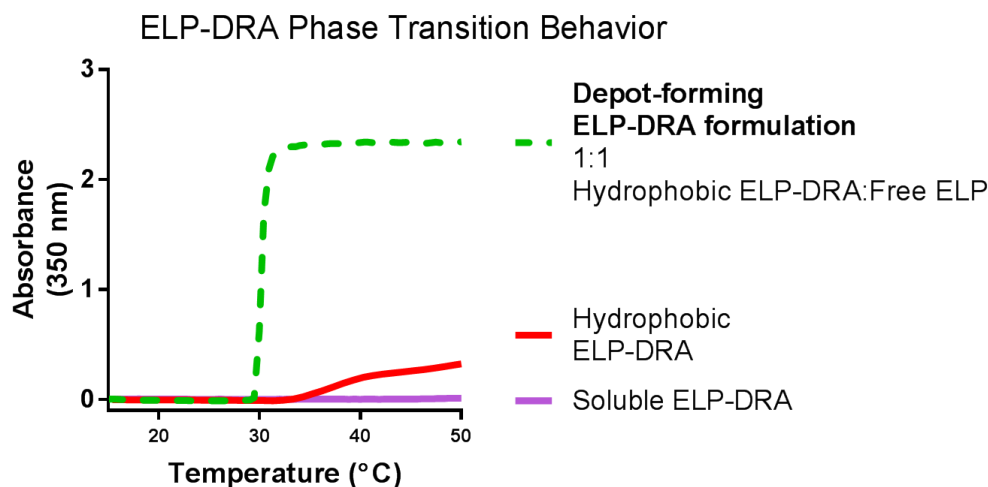


Figure 18: ELP-DRA formulation demonstrates appropriate phase-transition behavior for gel depot formation.

Optical turbidity measurements (OD_{350}) reveal that soluble ELP-DRA does not undergo phase transition below 50°C , hydrophobic ELP-DRA does not fully transition between room temperature at 37°C , and a mixture of free hydrophobic ELP with the hydrophobic ELP-DRA fusion at a 1:1 molar ratio undergoes a phase transition at approximately 30°C .

Prior to *in vivo* testing of the ELP-DRAs, we conducted further analysis on the hydrophobic ELP-DRA, as its phase transition behavior was unexpected. Specifically, we used dynamic light scattering (DLS) to evaluate the hydrodynamic radius (R_h) of the particles in solution at a range of temperatures (Figure 19). DLS showed that the protein existed primarily as monomers/dimers of relatively stable radii around 10-13 nm between 20 - 30°C . A radius of 13 nm is relatively large for a monomer, which suggests that the protein may exist as a dimer over this temperature range. Between 30 - 35°C , the protein self assembles to form a nanoparticle with a radius of about 50 nm, which stabilized to about 42-45 nm as the temperature was increased to 55°C . Since the R_h

remained stable as the sample was heated to its peak temperature of 50°C, it appears that the protein does not aggregate to a large extent at high temperatures.

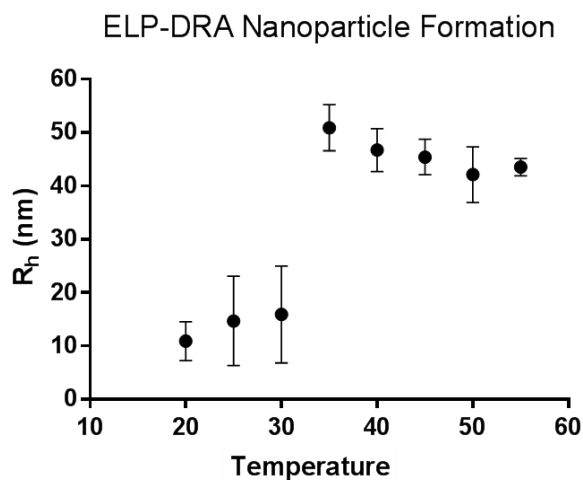


Figure 19: Fusions of hydrophobic ELP to DRA form nanoparticles at physiological temperature.

DLS results reveal that fusion of hydrophobic ELP to DRA results in formation of 40-50 nm nanoparticles at physiological temperature.

3.3.4 Depot-forming ELP-DRA formulation abolishes tumors *in vivo*

The depot-forming ELP-DRA mixture with free ELP is henceforth referred to as the depot-forming ELP-DRA formulation. A pilot study, in which nude mice with subcutaneous Colo205 xenografts were intratumorally injected once with 3 mg/kg or 30 mg/kg of this formulation, demonstrated the efficacy of the depot formulation (Figure 20).

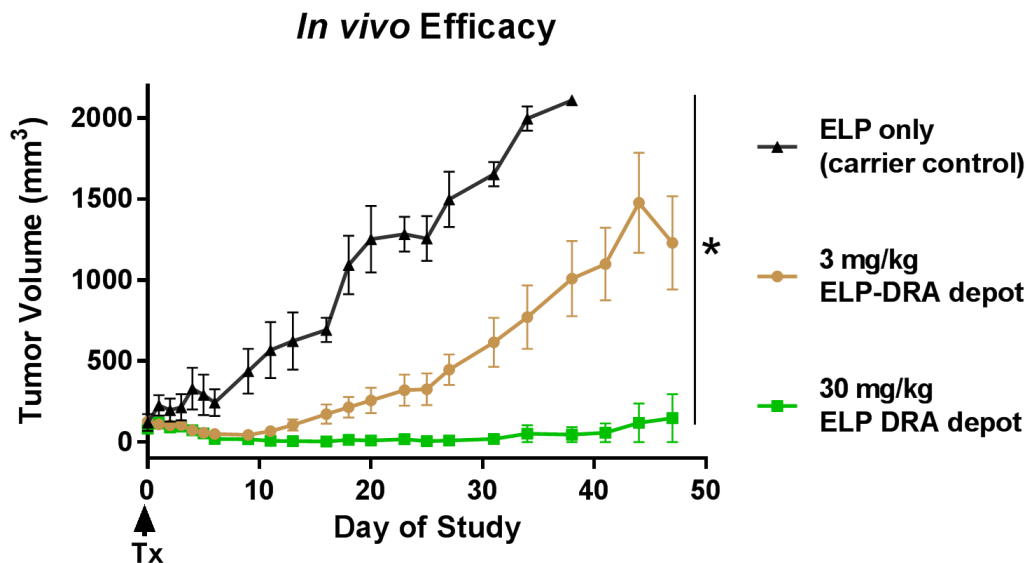


Figure 20: Pilot tumor regression study confirms ELP-DRA depot efficacy *in vivo*.

Nude mice were xenografted with DRA-sensitive human CRC cell line Colo205 and treated with 3 mg/kg (brown) or 30 mg/kg ELP-DRA (green) depot formulation or ELP control (black) and tumor volumes were monitored for about 50 days (n=4 in each group). Three of the four mice treated with a single intratumoral injection of 30 mg/kg ELP-DRA formulation experienced complete tumor regression. Data were analyzed using two-way analysis of variance (ANOVA) of matched values followed by Fisher's LSD multiple comparisons test to establish significance ($p < 0.05$) of the difference between groups at each day of treatment. Results indicate statistically significant differences in tumor volumes between and including days 14 and 47 for depot-forming 30 mg/kg ELP-DRA treatment group compared to other groups including the 3 mg/kg ELP-DRA treatment group. * $p < 0.05$.

Encouraged by these introductory results, we conducted a much larger and comprehensive *in vivo* study to evaluate the depot-forming ELP-DRA formulation compared to a molecular weight controlled soluble ELP-DRA, free DRA, and TRAIL. Data from this study demonstrates that a single injection with the depot-forming ELP-DRA fusion formulation promotes regression of sensitive tumors and improved survival

compared to treatment with TRAIL, soluble hydrophilic ELP-DRA, and soluble DRA without ELP fusion (Figure 21). Each treatment group was injected only on day 0 at 30 mg/kg.

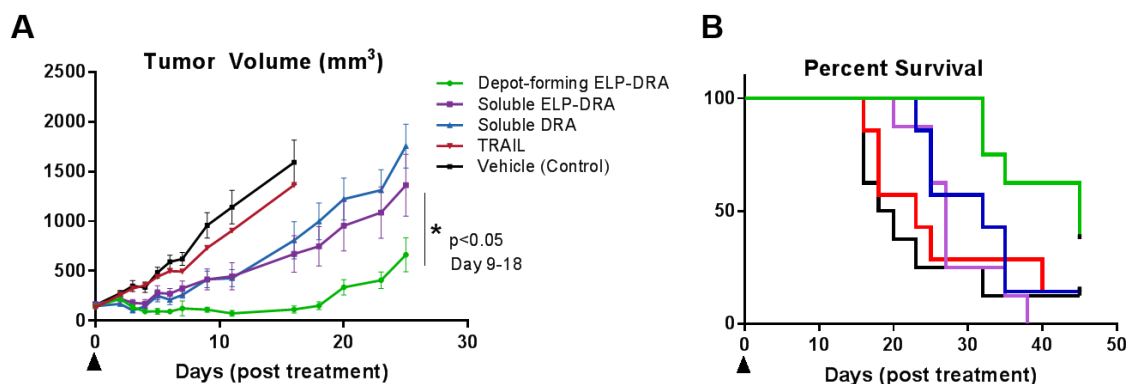


Figure 21: ELP-DRA depot demonstrates superior in vivo efficacy.

Tumor growth data plotting tumor volume vs. time. Data were analyzed using two-way analysis of variance (ANOVA) of matched values followed by Fisher’s LSD multiple comparisons test to establish significance ($p < 0.05$) of the difference between groups at each day of treatment. Results indicate statistically significant differences in tumor volumes between and including days 9 and 18 for depot-forming ELP-DRA compared to other groups including soluble ELP-DRA. (F) Kaplan-Meier survival results demonstrate prolonged survival in depot-forming ELP-DRA group. Evaluation of survival data with log-rank test suggests significant differences ($p < 0.05$) between depot-forming ELP-DRA and other treatment groups, with approximately 16 days increased median survival for the slow release formulation compared to the soluble version.

Having confirmed the potency of ELP-DRA and the efficacy of the sustained release formulation *in vivo*, we performed an experiment to establish the efficacy of the depot upon subcutaneous injection instead of direct intratumoral injection. The importance of this study lies in the fact that translatability of ELP-DRA for a disease such as colorectal cancer requires delivery from an easily accessible injection. Intratumoral administration was useful as proof-of-concept of depot efficacy, but a

follow-up *in vivo* study was conducted in which the ELP-DRA depot formulation was injected subcutaneously. This study confirmed the efficacy of the depot formulation using a clinically relevant administration approach (Figure 22).

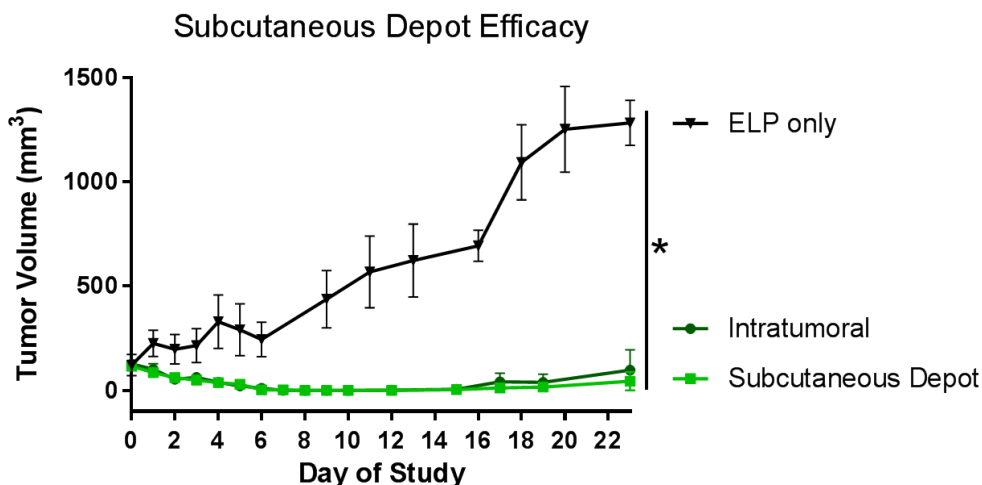


Figure 22: ELP-DRA formulation is efficacious when injected subcutaneously and does not require intratumoral injection for *in vivo* tumor regression.

ELP-DRA depot formulation was injected once on Day 0 at 30 mg/kg in nude mice xenografted with Colo205 tumor cells. Subcutaneous injection of the depot was performed on the left flank, as the tumor was located on the right flank (light green). Intratumoral injection was performed at the dosage (dark green). ELP vehicle control is plotted for comparison. Two-way ANOVA followed by Fisher's LSD test results indicate statistically significant differences ($p < 0.05$) in tumor volumes between and including days 4 and 23 for both depot-forming ELP-DRA formulations in comparison to the ELP only control.

3.4 Significance

We have applied an ELP-based protein delivery strategy to prolong DRA residence time *in vivo*, as demonstrated by significant anti-tumor efficacy of the ELP-DRA gel depot formulation in the DRA-sensitive Colo205 model following only with a single injection. First, we demonstrated that ELP fusion to the DRA does not affect pro-

apoptotic bioactivity of the DRA *in vitro*. We then designed, produced, and purified ELP-DRA fusions that increase the size of the molecule from 66 kDa to approximately 110 kDa, reducing the rate of renal clearance. We selected a molecular weight control soluble ELP and a hydrophobic depot-forming ELP for fusion to the DRA. Upon investigation of the hydrophobic ELP-DRA fusion by light scattering, we discovered that this fusion likely self-assemble into 40-50 nm nanoparticles at physiological temperature. To drive gel depot formation of this fusion, free hydrophobic ELP was mixed in, and this mixed depot was observed to undergo phase transition between room temperature and body temperature. The ELP-DRA depot formulation was then tested *in vivo*. The mouse xenograft model of Colo205 tumors validated ELP-DRA depot efficacy. Mice treated with the ELP-DRA depot experienced superior tumor regression and extended survival compared to mice treated with vehicle, TRAIL, DRA, or soluble ELP-DRA. With this ELP-based approach, we successfully addressed the delivery challenge of the DRA. The next step, as discussed in Chapter 4, focused on the development of effective drug combinations to overcome drug resistance in DRA-resistant colorectal cancers.

4. Rational design of drug combinations to overcome DR5 agonist resistance in cancer cells

4.1 Introduction

In parallel to effective drug delivery, cancer treatment must account for inevitable tumor resistance. Increasingly, genomics research can provide a spatially and temporally resolved portrait of the mutations and cell types in individual cancers, allowing for tumor profiling and the discovery of therapeutic vulnerabilities (54). Functional genomics can reveal new targets for precision therapy by revealing the genetic drivers of drug resistance to targeted therapeutic agents.

Recent studies suggest that multivalency and potency are necessary but insufficient for a successful pro-apoptotic therapeutic, as many cell lines and most primary cancers are actually resistant to TRAIL (36, 37). To systematically map the resistance pathways that confer death receptor agonist (DRA) resistance, we took advantage of two complementary experimental screening methods: (1) a gain-of-function (GOF) open reading frame (ORF) screen and (2) a loss-of-function (LOF) clustered regularly-interspaced short palindromic repeats (CRISPR) screen.

4.1.1 ORF gain-of-function screen

A pathway-centric ORF screen was used to determine potential modes of resistance to TRAIL. The library accounts for 17 major signaling pathways that influence cancer cell proliferation, survival, differentiation, and apoptosis. Each of the 17 pathways is represented by 1-3 mutant cDNAs that, upon overexpression in the cells,

constitutively activate or inactivate the pathway. These cDNAs encode proteins that are at core pathway nodes, and are tumor-promoting (pathway-activating mutants) or tumor-suppressive (pathway-inhibition mutants). This screening approach was previously validated in a BRAF-mutant melanoma cell line to identify pathways that promote resistance to a MEK1/2 inhibitor (79). The results of the screen aligned well with other published studies and led to additional previously unreported findings. Unlike comprehensive gene expression analysis techniques, this approach focuses exploration efforts using a rational process that probes the mechanisms of drug resistance in intrinsically sensitive cell lines (59, 80). Thus, we conducted the screen in a TRAIL- and DRA-sensitive colorectal cancer cell line. The CRISPR/Cas9 loss-of-function screen delineated in the next section complements this method, as it identifies genetic sensitizers in intrinsically drug resistant cell lines.

4.1.2 CRISPR/Cas9 loss-of-function screen

The LOF screen uses the CRISPR/Cas9 system to target nearly 400 genes that may sensitize cancer cells to the drug. Using RNA-guided CRISPR-associated nuclease Cas9, it is possible to introduce specific, targeted loss-of-function mutations into the cancer cell genome. Synthetic short-guide RNAs (sgRNAs) can be generated to target specific locations in genes of interest, guiding Cas9 to induce DNA double-stranded breaks at those locations (63). The approach used in our studies is based on work by Wang and colleagues, in which short-guide RNA (sgRNA)-expressing lentivirus was

used to knock out expression of over 7000 genes, generating a library of cells that could be screened under both positive and negative selection. After application of the desired selection pressure, the number of surviving cells carrying each sgRNA can be determined using high-throughput sequencing (81).

Recently, the Wood lab at Duke University has developed a library of 2000 sgRNA constructs targeting about 400 genes (5 sgRNA representing each gene) that are implicated in cell survival and tumor resistance (82). This library can be screened in resistant cell lines to identify specific knockouts that confer drug sensitivity (Figure 23). The genes represented in the library comprise key known genes in chromatin modification, chemoresistance, apoptosis, tumorigenesis, and DNA repair. Key kinases and common cancer therapeutic targets are also represented.

We hypothesized that information gleaned from the LOF CRISPR/sgRNA screens (Figure 23), along with the GOF ORF screen results, could facilitate the design of drug combinations that reverse or prevent resistance by inhibiting prohibitive pathways (83). Specifically, the result of these screens informed the rational selection of small molecule sensitizers for combination testing with the DRA and evaluation of efficacy in DRA-resistant colorectal cancer cells. These methods, as outlined in the next section, enabled the design of DRA drug combinations that overcome resistance in patient-derived colorectal cancer cells.

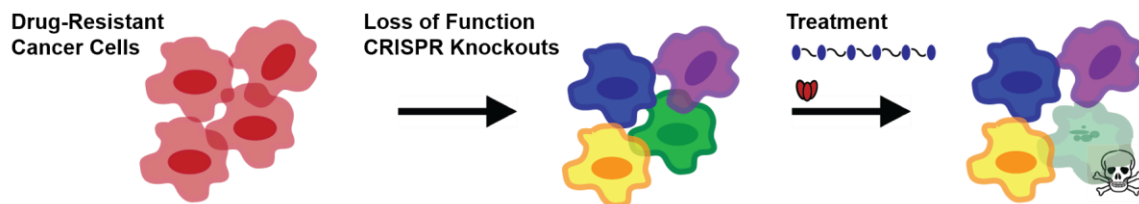


Figure 23: Schematic of CRISPR/Cas9 knockout screen.

CRISPR/Cas9 technology is used to inhibit signaling pathways in drug-resistant cancer cells and the library is screened to identify genes that sensitize the cells to TRAIL and DRA.

4.2 Materials and methods

4.2.1 ORF gain-of-function screen

We used a library of 37 pathway-activating constructs and controls in lentiviral form. This library, recently developed in the Wood lab at Duke University, uses a phosphoglycerase kinase 1 (PGK) promoter for lentiviral expression in vesicular stomatitis virus G (VSV-G) pseudotyped lentivirus (84). All lentivirus particles corresponding to each construct were produced by transfection of 293T cells and individually titered in HCT116s by limiting dilution. The multiplicity of infection (MOI) was approximately equal to 1 for each construct. An overview of the experimental process is shown in Figure 24. The screen was performed by seeding HCT116s at 500,000 cells/well in six-well plates. The following day, each well was infected with a different pathway-activating or control vector, to produce 37 isogenic cell lines. After 24 hours, puromycin was added to the media to select for successfully infected cells. Cells were incubated with puromycin for two days, after

which cells from each well were trypsinized, counted, and seeding into 96-well plates at 5000 cells/well. The next day, cells were treated with vehicle or TRAIL at various concentrations spanning seven orders of magnitude to generate dose response curves. After 2-3 days of incubation with the drug, cell viability was measured as previously described using the AQueous One MTS assay (Promega).

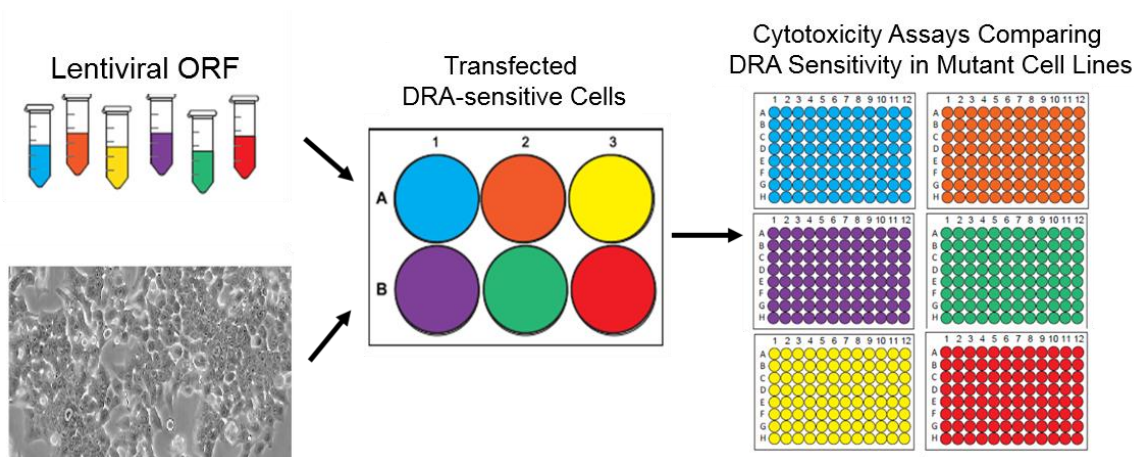


Figure 24: Overview of the gain-of-function ORF library screen.

First, viral vectors for constructs of interest are produced (left). DRA-sensitive HCT116s are seeded in 6-well dishes and each well is infected with a different vector and successfully infected cells are selected with puromycin (center). Finally, cell viability assays are performed with the new array isogenic cell lines to obtain dose response curves upon treatment with TRAIL (right).

4.2.2 CRISPR/Cas9 loss-of-function screen

Lentiviral production and titration of CRISPR/Cas9 loss-of-function library

Lentivirus were produced from HEK293T cells, which were grown to 50% confluence in 6 cm plates and transfected using Fugene6 (Promega), 5.6 mg of psPAX2, 0.625 mg of pVSVg, and 6.25 mg of library plasmid. After 30 min of incubation at room

temperature, the transfection mixture was added to the cells and incubated overnight at 37°C. The next day, harvest media was added (DMEM, 30% FBS). After 24 h and 48 h collection points, harvested virus was passed through a 0.45- μ m filter. Viral titers and transductions were performed as previously described (79). Thus a pooled library of viral vectors encoding LOF sgRNA inserts that targeted a panel of 378 druggable genes and signaling pathways was obtained.

CRISPR/Cas9 loss-of-function screen

To identify genetic drivers of CRC resistance to DRAs, we performed a CRISPR/Cas9-based loss-of-function (LOF) screen, as previously described (82). A brief overview of the procedure follows (Figure 25). A library of viral vectors encoding LOF sgRNA inserts were cloned into a lentiviral expression vector encoding Cas9, packaged with a psPAX2 plasmid, and pseudotyped with VSV-G. Once the pooled lentiviral library was produced by transfection of 293T cells, titered, and used to infect DRA-resistant RKO cancer cells. RKO cells were seeded at 500,000 cells per well in 6 well plates, incubated overnight, and transduced at a multiplicity of infection (MOI) of 0.3 the next day. After puromycin selection, a sample was taken to verify representation of the various knockout genes. The transduced population was maintained under puromycin selection for one week, after which the library of cells was then exposed to vehicle, TRAIL (10 nM), or the DRA (1 nM), each treatment condition in duplicate, for two weeks. Cell samples were obtained, genomic DNA was extracted (DNeasy Blood &

Tissue Kit; QIAGEN), sgRNA barcodes were isolated, and indexing primers were appended by PCR (63). The samples were sequenced by next-generation Illumina sequencing (Hudson Alpha), and the raw data was processed to identify “hits” that sensitized RKO cells to each treatment, as evidenced by their depletion in drug versus vehicle treatment conditions. The fractional representation (FR) for a given guide in the final condition after vehicle treatment was compared to its FR final condition after TRAIL or DRA treatment. The depletion level of each sgRNA barcode (drug versus vehicle conditions) was calculated; depleted barcodes represent sensitizer genes, as they were specifically depleted in the drug-treated cell populations. Depletion comparisons were used to generate a scoring metric called the “3 score” which represents the average of the three most depleted sgRNAs for a particular gene. The genes were ranked by their 3 scores; top hits are those that sensitized the cells to TRA treatment when knocked out by the CRISPR/Cas9 machinery. Data are presented as the depletion metric (FR from treated population normalized to FR from vehicle control, both at final timepoint) mean of the 3 score per gene in the library. “Hits” are genes with low 3 score. All data extractions and calculations were coded and completed using R. The hits were subsequently filtered to retain genes that encoded proteins for which specific inhibitors are commercially available.

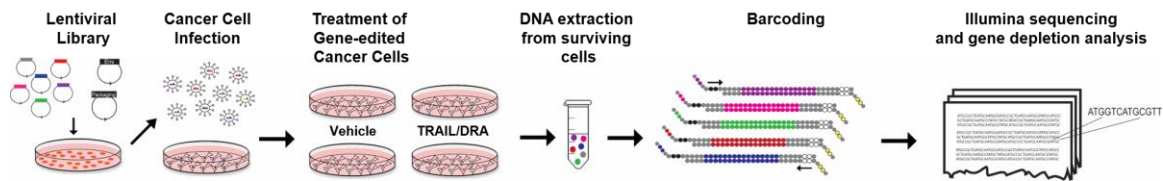


Figure 25: Overview of loss-of-function CRISPR screen experimental set-up.

First sgRNA expression, packaging, and envelope plasmids were transfected into 293T cells and lentiviral particles were harvested. The RKO cell line was then infected with the pooled lentiviral library and puromycin selection was completed. The transfected cell line was subcultured for each desired condition (in duplicate) and treatment continued for 2-3 weeks, after which DNA was extracted from all samples. Constructs were barcoded by PCR and the product was then sent for Illumina sequencing.

4.2.3 Short-term drug combination studies

Cell lines. All cell lines were grown at 37°C in 5% CO₂. RKO were cultured in MEM Earle's (10% FBS, pyruvate, NEAA, 1% P/S). Cell lines were purchased within 6 months from Duke CCF or ATCC and patient-derived lines were obtained from David Hsu (Duke University) and passaged less than 10 times. All cell lines were authenticated using Promega PowerPlex 18D kit for short tandem repeat (STR) analysis or were purchased within 6 months from Duke CCF. All cell lines were tested for mycoplasma by Duke CCF. FBS: fetal bovine serum (GIBCO); P/S: penicillin/streptomycin (Thermo Fisher). Media was purchased from GIBCO or Sigma Aldrich.

In Vitro Cell Viability Testing. For single-agent cytotoxicity evaluation, drugs were tested *in vitro* using a luminescent cell viability assay method as follows. The cells were plated in white 96 well plates at a density of 2,000-10,000 cells/well in 90 µL of complete media (RPMI 1640+10% FBS) and incubated for 12-18 hours at 37°C with 5% CO₂. The

cells were then treated with 10 μ L additional media containing a serial dilution of the drug(s) of interest. All treatments were done in triplicate. After 72 hours, the Promega Cell Titer Glo reagent was used according to manufacturer's instructions to assay the number of viable cells; it is an accepted luminescent cell viability assay method. The cell viability was determined using measurements of luminescence using a plate reader. The dose response curves were generated by plotting percent viable cells v. compound concentration. The dose response curve was approximated from the scatter plot using a four-parameter logistic model calculation, and EC₅₀ was calculated as the concentration of drug required to kill 50% of the cells.

For combination treatments, the cell viability assays were carried out as follows. Colorectal cancer cells were plated in white 96 well plates at a density of 2,000 cells/well in 90 μ L of complete media (RPMI 1640+10% FBS) and incubated overnight at 37°C with 5% CO₂. Drugs used to enhance the sensitivity of cells to the death receptor agonists (DRAs) are referred to as "sensitizing drugs." Sensitizing drugs were dosed at a single concentration, or "background dose", which was chosen below the EC₂₅ in each cell line. The cells were treated with 10 μ L media containing the serial dilution of death receptor agonist and a background dose of sensitizing drug(s). The treatments were done in triplicate to account for technical variability. After 72 hours, the Promega Cell Titer Glo reagent was used according to manufacturer's instructions to assay the number of viable cells; it is an accepted luminescent cell viability assay method. The cell viability was

determined using measurements of luminescence using a plate reader. The dose response curves were generated by plotting per cent viable cells v. DRA concentration. Cell viability was normalized to the viability of the cells treated with the background dose of sensitizer only such that the effects seen are truly associated with DRA. The dose response curve was approximated from the scatter plot using a four-parameter logistic model calculation, and EC₅₀ was calculated as the concentration of DRA required to kill 50% of the cells.

Flow Cytometry for Annexin-V Apoptosis Quantification. Cells were seeded in six-well plates overnight. The next day, cells were treated with the indicated amount of drug(s) or vehicle control (DMSO). Incubation was conducted for 15 hours with etoposide or for 48 hours with DRA ± sensitizers. To prepare for flow cytometry analysis, each well of cells was washed twice with ice-cold PBS and resuspended in 1X annexin V binding buffer (10 mM HEPES, 140 mM NaCl, 2.5 mM CaCl₂; BD Biosciences). APC-conjugated Annexin V was used to measure surface exposure of phosphatidylserine and 7-AAD was used as a viability probe (BD Biosciences). Experiments were analyzed at 20,000 counts/sample using BD FACSVantage SE.

4.2.4 Long-term drug combination studies

2D Clonogenic Growth Assay. Cells were seeded in 6-well plates at 500 cells per well. The next day cells were drugged at the indicated doses and drug media was replaced every 3-4 days. Approximately 1.5 week after treatment, plates were rinsed

with PBS and fixed and stained with 0.5% (wt/vol) crystal violet in 6.0% (vol/vol) glutaraldehyde solution (ThermoFisher Scientifics) for 20 min at room temperature. Plates were rinsed in diH₂O, dried overnight, and photographed the following day. Percent colony area covered by crystal violet was quantified using the ImageJ Software colony area plugin.

In vitro time to progression assay. An *in vitro* time to progression assay was used to evaluate the efficacy of combination treatments compared to monotherapy over the course of four weeks. Colorectal cancer cells were trypsinized, counted, and seeded at a density of 50,000 cells per 6 cm² plate; each treatment condition was tested in triplicate. The following day, cells were treated with vehicle, monotherapy, dual drug treatment, or triple drug combinations of interest. Media and drug were replenished every 2-3 days and cells were counted, seeded, and treated twice a week. Calculation of growth rate allowed for estimation of total cell count over time for each condition.

4.2.5 Immunoblotting

Cells were seeded in at 500,000 cells per 10 cm² dish and treated the next day. After treatment for 6 and 16 hours, cells were scraped off of wells in cold PBS, centrifuged at 5,000 rpm for 3 minutes at 4°C, separated from supernatant, washed with PBS once, and frozen at -80°C until processed for Western blot. then lysed with cold RIPA buffer (20 mM Tris-HCl pH 8.0, 137 mM NaCl, 10% glycerol, 1% NP-40, 0.1% SDS, 0.5% Nadeoxycholate, 2 EDTA pH 8.0) supplemented with protease and phosphatase

inhibitors (Roche protease inhibitor cocktail; Phosphatase Inhibitor Cocktail I and Phosphatase Inhibitor Cocktail II from Sigma-Aldrich) and centrifuged at 4°C, 13,300 rpm for 10 minutes. Protein concentration in supernatant lysates were determined using Bradford assay (Biorad). Proteins from each lysate (10 µg) were resolved on SDS-PAGE (NuPAGE 4-12%), transferred to PVDF membranes, blocked with 5% milk in TBS+0.1% Tween, and probed with primary antibodies in 5% BSA overnight at 4°C. Primary antibodies (1:1,000-1:2,000 dilution) recognized BCL-XL (CST#2764), BIM (CST#2933), BID (CST# 2002), Caspase 3, 8, 9, and β-actin.

4.3 Results and discussion

4.3.1 ORF GOF screen results

With the gain-of-function ORF screen, we interrogated 17 pathways that frequently play important roles in oncogenic processes. The focus of this study was to identify the pathways that conferred TRAIL resistance to a TRAIL-sensitive human colorectal cancer cell line, HCT116. Resistance was measured by determining the change in EC₅₀ of TRAIL in cell viability assays. To analyze and compare the EC₅₀ results from the cell viability assays, we identified constructs that resulted in at least a 2-fold increase in EC₅₀; these mutant cells lines were at least twice as resistant to TRAIL as the parent cell line. As shown in Figure 26, three key pathways of resistance stood out in these results: Wnt/β-catenin, p38 MAP kinase, and the intrinsic apoptotic pathway. A

literature survey was then conducted to understand the known roles of these signaling pathways in the context of TRAIL resistance.

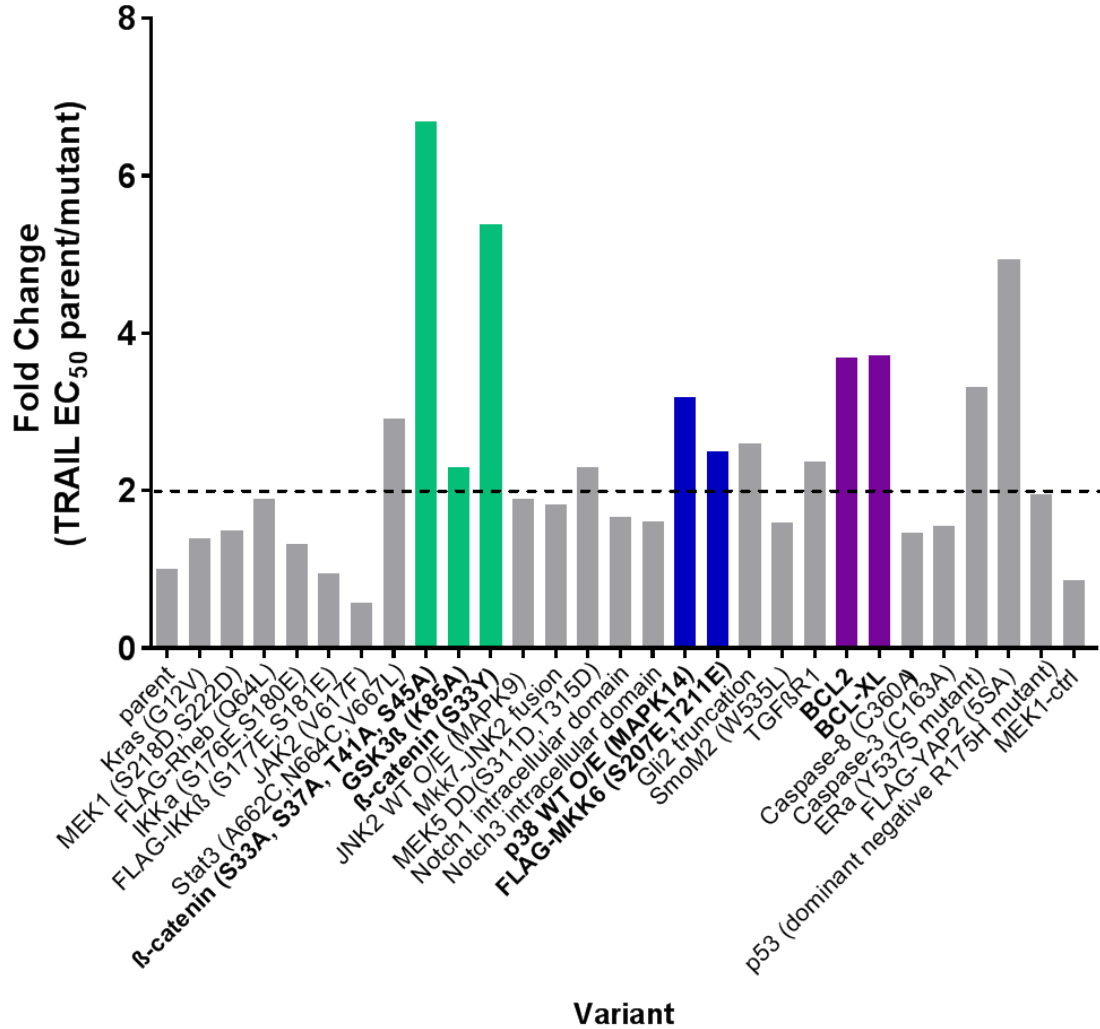


Figure 26: GOF ORF screen results reveal key players in TRAIL resistance.

EC₅₀ values were obtained from cell viability assays. A 2-fold change in EC₅₀ was chosen as the lower limit of altered sensitivity. Cell lines expressing mutant genes (x-axis) in the Wnt/β-catenin (green), p38 MAP kinase (blue), and intrinsic apoptosis (purple) pathways consistently showed resistance (>2-fold change compared to parent cell line).

Recent studies suggest that Wnt signaling can affect TRAIL sensitivity in colon cancer. In one study, De Toni and colleagues showed that silencing β -catenin expression with siRNA resulted in a strong reduction in osteoprotegerin (OPG), a soluble decoy receptor for TRAIL. Importantly, this translates to significant TRAIL sensitivity in colon cancer cells, including HCT116s (85). In another study, Kaler and colleagues reported that IL-1 β release from tumor-associated macrophages results in enhanced Wnt signaling and subsequently increases TRAIL resistance in colon cancer cells, including HCT116s (86). Our results align well with these findings, so follow-up experiments will be conducted with small molecule inhibitor niclosamide, an anti-helminthic that inhibits Wnt signaling. Niclosamide is also known to inhibit proliferation in colon cancer cell lines, including HCT116 cells (87).

TRAIL can also induce non-canonical kinase signaling in cancer cells (88). According to Son and colleagues, inhibition of p38 with the small molecule inhibitor SB203580 led to increased TRAIL sensitivity in prostate cancer cells (89). In our experiments, p38 signaling led to increased TRAIL resistance, suggesting that HCT116s exhibit a similar response. It is important to note that in some colon cancer cells, such as DLD-1s, p38 activation does not alter TRAIL sensitivity (88). We conducted a few preliminary follow-up studies in which CRC cells were treated with combinations of TRAIL and p38 signaling pathway small molecule inhibitors; these drug combinations did not increase cytotoxicity of TRAIL or exhibit synergistic effects.

The third key pathway identified in our screen was the intrinsic apoptosis pathway. Bcl-2a1 and Bcl-2l1 encode an anti-apoptotic BCL-2 family protein and anti-apoptotic BCL-X_L, both of which promote cell survival. It is no surprise, then, that these proteins emerged as important players in HCT116 TRAIL resistance. In fact, HCT116 cells are known to depend on the pro-apoptotic Bax protein for TRAIL-induced apoptosis (90). To follow up on our results, we can perform combination studies with TRAIL or DRA and BCL2 or BCL-X_L inhibitors, which can neutralize the functional activity of anti-apoptotic members of the Bcl-2 family of proteins.

4.3.2 CRISPR/Cas9 LOF screen results

A CRISPR/Cas9 loss-of-function (LOF) screen to map the genetic landscape of resistance to a multivalent DRA (62, 91, 92). Specifically, the screen identified genes that, when knocked out, confer sensitivity to the DRA in resistant colorectal cancer (CRC) cells. It used a recently created lentiviral short guide RNA (sgRNA)/Cas9 library targeting key nodes in major oncogenic growth, survival, and DNA damage response pathways, as well as many other potential drug targets and sensitivity modifiers (e.g., kinases, histone deacetylases, metabolic enzymes, BCL-2 family proteins, etc.). We previously demonstrated that by coupling the results of resistance pathway screening with newly developed, long-term culture methods, it is possible to discover and credential combination therapies that delay resistance evolution (82).

Briefly, after exposure of library-transduced cells to TRAIL or DRA for two weeks, cell samples were isolated, DNA was extracted, and PCR was used to amplify and index barcode sgRNA amplicons. Depletion scores for each sgRNA was first determined by normalizing the relative abundance of each construct in the control group (vehicle treatment) at week 2 to the same quantity at the beginning of the screen. sgRNA-level scores were converted to gene-level scores using the “3-score” which represents the average of the three most depleted sgRNAs for a particular gene (93). In Figure 27, each point represents an individual gene plotted at the 3-score value obtained for replicate 1 (x-axis) and replicate 2 (y-axis). The 3-score values corresponding to vehicle at the final timepoint compared to the initial timepoint are called essentiality. Genes with low 3-scores are essential for inherent cell viability. The essentiality data show that the screen was reproducible (3-scores of the 2 replicates fall along the $y=x$ line), and allow for differentiation of those genes that are inherently important for RKO survival from those that sensitize RKO to drug (Figure 27).

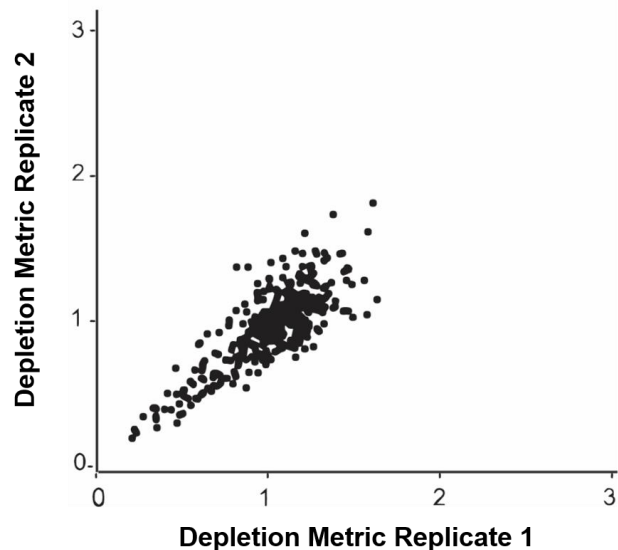


Figure 27: Replicate comparison of gene-level essentiality phenotypes in the CRC cell line RKO.

The 3-score depletion metric ($t = 2 \text{ weeks}/t = \text{initial}$) for each gene in the library is plotted. Essentiality was calculated by assessing depletion of constructs at the beginning of the study (pre-treatment time zero compared to the end of the study (in vehicle control)). Each point is a different gene, and is plotted at the depletion score for each replicate. Genes that are not essential for RKO survival have a depletion value of ≥ 1 .

Next, sensitizer genes were identified using sgRNAs depletion scores as determined by normalizing the relative abundance of each construct in the presence of TRAIL or DRA to the same quantity in the presence of vehicle. The 3-score was used to rank genes that, when knocked out, sensitize the cell to drug treatment. Close correspondence between the results of technical replicate screens is indicated in replicate plots, and hits were identified as those genes reproducibly depleted in replicate screens. The 3-score of the depletion metric for each gene from the TRAIL and DRA sensitizer

screens is plotted in Figure 28 and the readout of these values is provided in Appendix

B.

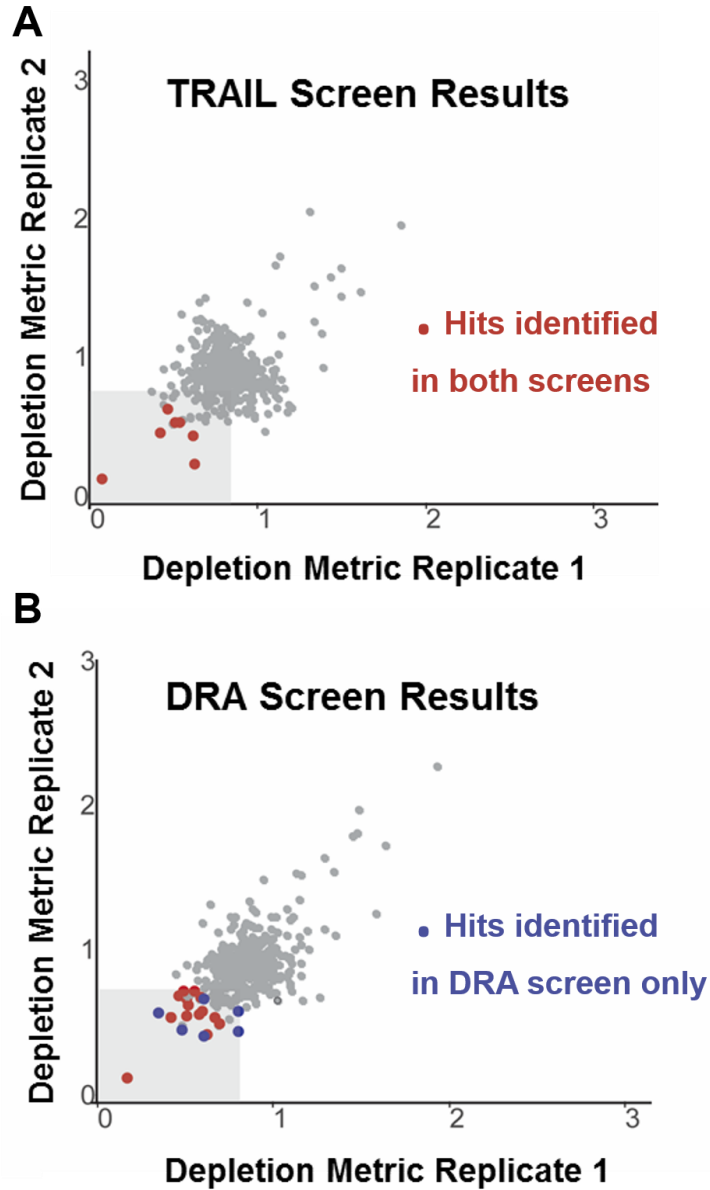


Figure 28: CRISPR/Cas9 loss-of-function screen results for TRAIL and DRA. Gray box indicates genes with depletion metric scores <0.8. Each dot represents a gene and is plotted on the depletion metric of each of its two replicates (replicate 1 on x axis,

replicate 2 on y axis). Red dots indicate common hits between (A) TRAIL and (B) DRA screens. Blue dots indicate hits uniquely generated in the DRA screen.

All genes with depletion 3-score below 0.8 for both replicates were extracted; this threshold ensures that knockout of the gene results in at least 20% loss in cell viability upon drug treatment. These genes were considered “hits”, and examined to identify possible small molecule inhibitors that target their associated proteins. Examples of key top scoring genes and their corresponding 3-scores for each replicate are shown in Table 2, alongside candidate small molecule drugs targeting their encoded protein products. Interestingly, the strongest hit in both TRAIL and DRA resistance screens was the gene for X-linked inhibitor of apoptosis protein (XIAP), a result that corroborates recent findings reporting XIAP's involvement in TRAIL resistance (94-98). Other top hits included anti-apoptotic proteins like BCL-X_L and kinases such as CDK6.

Table 2: Examples of hits from sensitizer screen.

The following are examples of genes that, when knocked out, sensitized RKO cells to the DRA. Importantly, the genes encode protein products that can be targeted by existing small molecule inhibitors. Rep1 and Rep2 refer to the 3 score of each of the 2 replicates in the DRA sensitizer screen.

Hit	Rep1	Rep2	Drug
XIAP	0.1645	0.1170	BV6
NFKB2	0.4057	0.5488	Niclosamide
CDK6	0.4650	0.6860	Palbociclib
HDAC8	0.5081	0.5456	PCI-34051
MCL1	0.5178	0.6218	A-1210477
YAP1	0.5509	0.7157	Verteporfin
SRC	0.5959	0.5735	Saracatinib
BCL2L1	0.6213	0.7249	WEHI-539

4.3.3 Genetically credentialed targeted inhibitors potentially sensitize cancer cells to DRA in short-term *in vitro* studies

To validate and extend the hits from the screens, we performed drug sensitization studies by evaluating the *in vitro* cytotoxicity of DRA in combination with each small molecule drug. The cells were treated with a “background dose” of the small molecule drug and increasing doses of DRA. The selected background doses were chosen to be high enough to engage the target yet lower than or equal to the EC₂₅ of the drug in the cell line. Cellular viability measurements associated with each combination treatment were then normalized to the viability measurement associated with the background dose alone, and as such all leftward shifts in the viability plots represent sensitization and not additive toxicity. Since DRA monotherapy resulted in no cytotoxicity regardless of dose, effective combination treatment results were dramatic. Guidelines were set to identify the most effective sensitizers; cytotoxicity of at least 50% at 100 nM (68) and an EC₅₀ of less than 1 nM were required (Figure 29A).

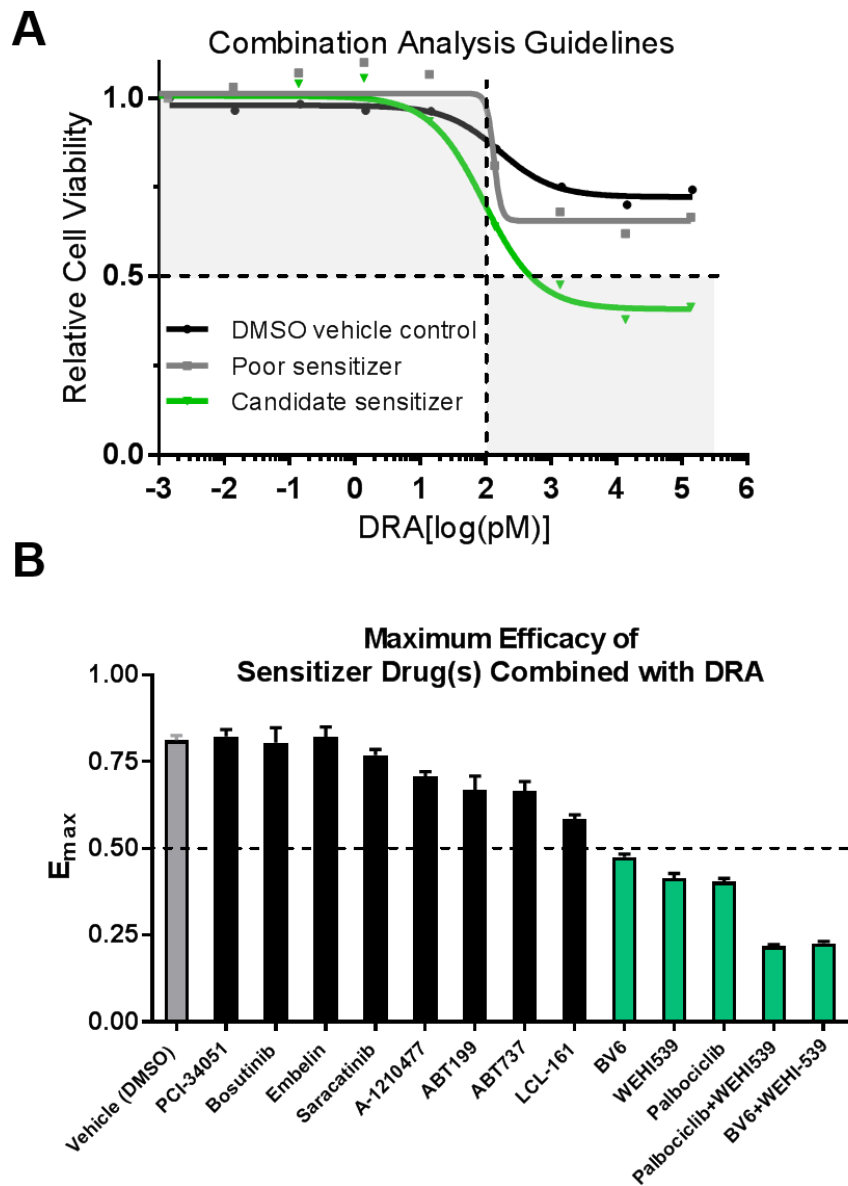


Figure 29: Drug combination guidelines and efficacy summary.

(A) The combination analysis guidelines require DRA EC_{50} in the picomolar range and maximum efficacy (E_{max}) below 0.5 upon combination with sensitizer in DRA-resistant RKO cells. (B) E_{max} (y axis) is shown for drug combinations in RKO cell viability assays; sensitizer is defined on the x axis. Green bars indicate data for sensitizer(s) that exhibit E_{max} below 0.5.

A condensed summary of the small molecule inhibitors and their target proteins is provided in Table 3. Upon combination of these inhibitors with the DRA, cell viability was assayed in DRA-resistant RKO cells and these results are also included in Table 3. Interestingly, the most efficacious drug combinations were not those targeting the hits with the best scores. This is likely due to limitations of the small molecule drugs and genetic pleiotropy. The robustness of the screen lies in its ability to provide a pool of potential sensitizer drugs for combination with the drug of interest. Drugs resulting in the lowest cell viability (described as the maximum effect, or E_{max}) were identified as the XIAP inhibitor BV6, the CDK4/6 inhibitor palbociclib, and the BCL-X_L inhibitor WEHI-539 (Fig. 29B).

Table 3: Summary of sensitizer drugs and observed DRA EC_{50} and E_{max} in combination cell viability assays.

The sensitizers were tested at the indicated background doses in combination with the DRA at a range of concentrations. EC_{50} and E_{max} are provided. R=resistant ($EC_{50} > 1nM$).

Sensitizer Target	Drug	Dose (μM)	DRA EC_{50} (pM)	E_{max}
XIAP, cIAP	BV6	1	0.83	0.50
CDK4/6	Palbociclib	2	72	0.41
BCL-X_L	WEHI-539	2	94	0.38
XIAP	Embelin	10	R	0.95
IAPs	LCL-161	3	R	0.58
Tyrosine Kinase	Bosutinib	1	R	0.82
Src Kinase	Saracatinib	1	R	0.77

Tyrosine Kinases	Desatinib	1	R	0.73
BCL-X _L , BCL-2	ABT737	1	R	0.67
BCL-2	ABT199	1	R	0.67
MCL-1	A-1210477	10	R	0.71
HDAC8	PCI-34051	1	R	0.80

The most effective sensitizers were then paired to evaluate the most potent 3-drug combinations comprising DRA and 2 small molecule inhibitors. As seen in Figure 29B and 30A, Palbociclib/WEHI-539/DRA, and BV6/WEHI-539/DRA are the most efficacious drug combinations in RKO cells, resulting in picomolar DRA EC₅₀ concentrations. These drugs were then tested in three human patient-derived colorectal cancer cell lines with a range of baseline sensitivities to DRA. In each case, the Palbociclib/WEHI-539/DRA, and BV6/WEHI-539/DRA triple combinations were extremely potent, sensitizing cells to picomolar concentrations (EC₅₀ values) of DRA and corroborating the results obtained in RKO cells (Figure 30B-D).

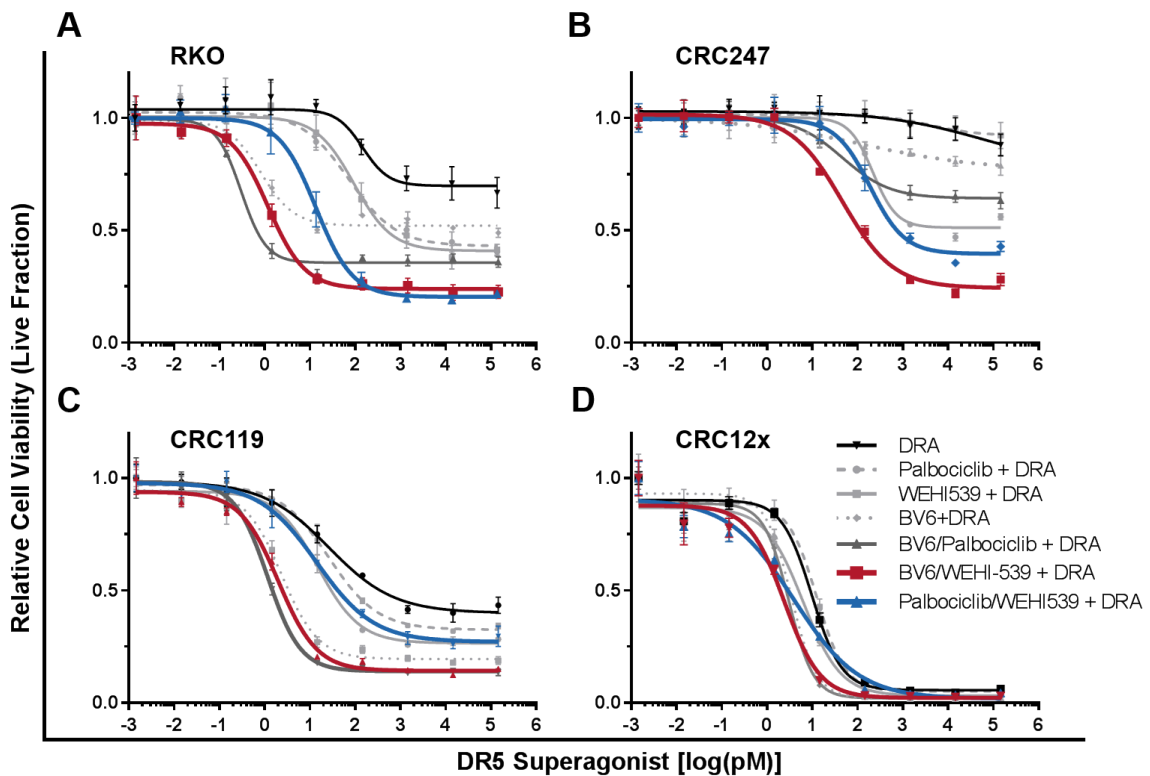


Figure 30: Cell viability assay results of combination treatment of DRA with targeted sensitizer drugs in RKO and three patient-derived cell lines.

Treatment with CDK4/6 inhibitor Palbociclib, XIAP inhibitor BV6, BCL-XL inhibitor WEHI-539, and DRA in (A) RKO cells and (B-D) three human patient derived cell lines. DRA concentration on x-axis and cell viability on y-axis.

4.3.4 Long-term *in vitro* studies confirm efficacy of sensitizers in combination with DRA in patient-derived DRA-resistant cells

Before testing the effective drug combinations in animals, we evaluated their potency and robustness in longer-term 2-dimensional (2D) growth assays. The 2D assays consist of a matrix in which DRA-resistant RKO and CRC247 cells are treated with increasing doses of the sensitizing drugs and DRA. Cell density was quantified for each treatment condition, and the percent colony area, demonstrate the efficacy of DRA when

combined with sensitizers (Figure 31). In short-term *in vitro* studies, WEHI539 was used to inhibit BCL-X_L, but this drug could only be used as an *in vitro* tool due to the presence of a labile and potentially toxic hydrazone moiety and poor physicochemical properties. Fortuitously, as our long-term *in vitro* studies commenced, A-1155463, a potent BCL-X_L inhibitor with *in vivo* activity became commercially available (99). The triple drug combinations of A-1155463 (A-11) + BV6 + DRA are the most efficacious inhibitors of cell growth, as seen in the bottom right of the 2D growth assay matrices (Figure 31A, B). The DRA drug concentrations were chosen as the minimum concentration required for complete growth inhibition (MinC) and two times MinC, as identified from cell viability assays. As shown in the bar graphs, the maximum concentration of each triple drug combination results in <5% colony growth area in both cell lines and triple drug combinations (Fig. 31C, D).

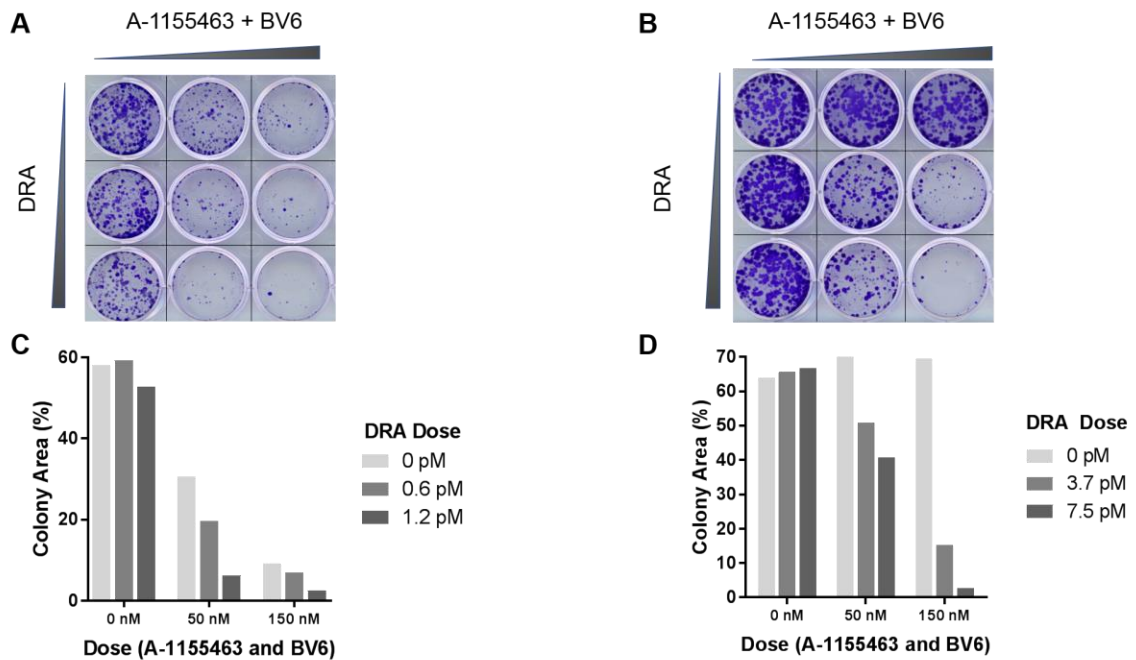


Figure 31: Clonogenic 2D growth assay experiments in human colorectal cancer cells demonstrate long-term potency of drug combinations.

Clonogenics in RKO (A, C) and CRC247 (B, D) cells indicates dramatically slower cell growth upon treatment with DRA in combination with increasing doses of A-1155463 and BV6 (left to right) and DRA (top to bottom). (C, D) Percent colony area has been graphed for visual purposes below the primary result.

A time-to-progression experiment with patient-derived CRC247 suggested that the triple drug combinations significantly slow tumor cell proliferation over 4.5 weeks. Figure 32 shows the cell number graphed on a log scale over time. The triple drug combinations of A-11/BV6/DRA and A-11/Palbociclib/DRA dramatically reduce growth rate in comparison to the corresponding double drug combinations. The slopes of the lines suggest that the A-11/Palbociclib/DRA combination slows growth most

significantly while the values indicate the efficacy of both drug combinations in reducing proliferation rate.

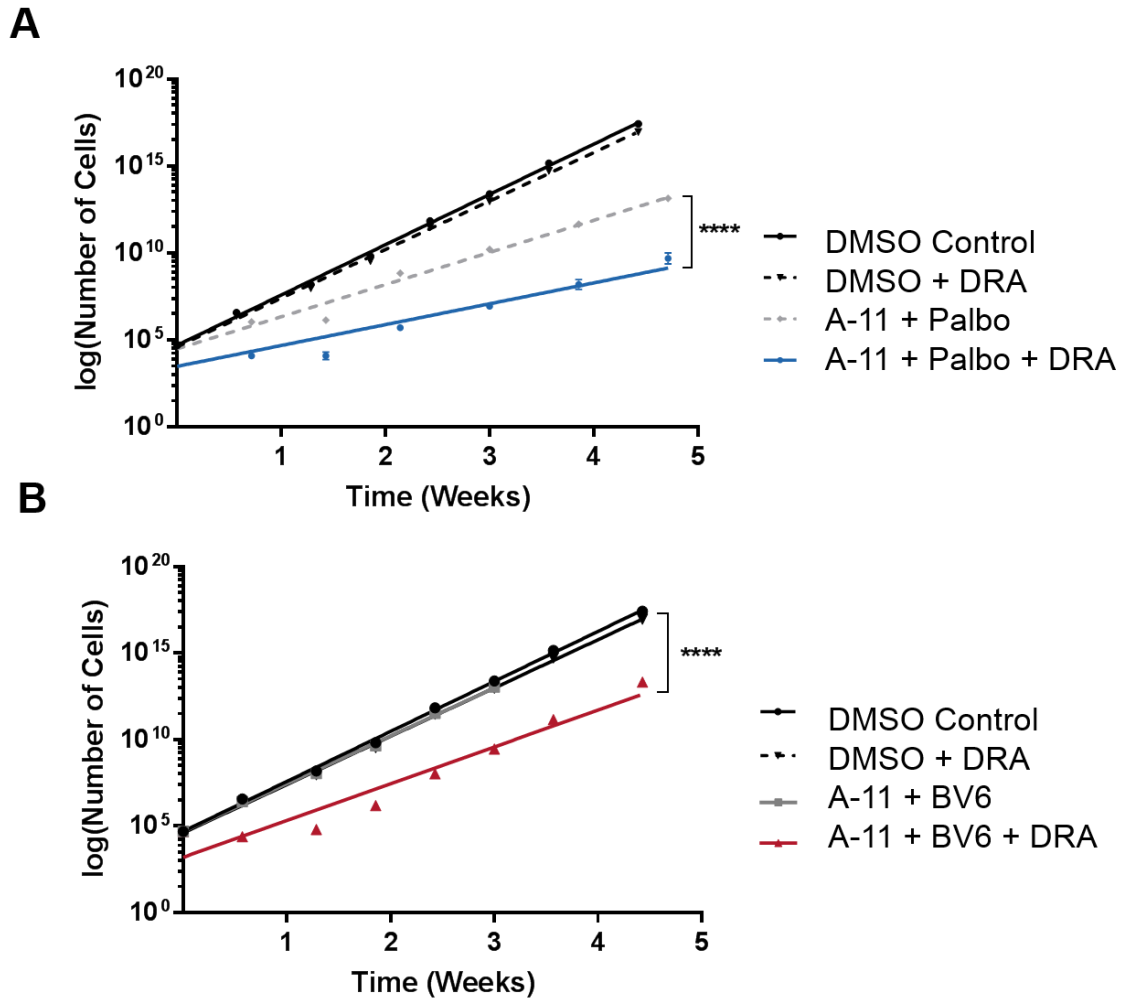


Figure 32: Time-to-progression assay in patient-derived CRC247s.

Cells are continuous cultured in different treatment conditions. (A) The double combination of A-1155463 (A-11) and Palbociclib (Palbo) is highly potent compared to DRA alone or DMSO control, and the triple combination of A-11 and Palbo with DRA results in the best time to progression result over 4.5 weeks. (B) Growth rates indicate slowed time to progression with triple combination treatment of A-11+BV6+DRA. One-way ANOVA at each timepoint at and after day 4 confirms statistically significant differences between A-11+BV6 and A-11+BV6+DRA with $p < 0.0001$, and between A-11+Palbo and A-11+Palbo+DRA with $p < 0.0001$.

4.3.5 DRA combination with key sensitizers promotes apoptotic pathway signaling

Confirmation of cellular apoptosis was provided by quantification of Annexin V positive cells using flow cytometry; RKO cells incubated with triple drug combinations of DRA, the BCL-X_L inhibitor A-1155463, and BV6 resulted in increased apoptotic cells compared to single or double drug treated cells (Figure 33).

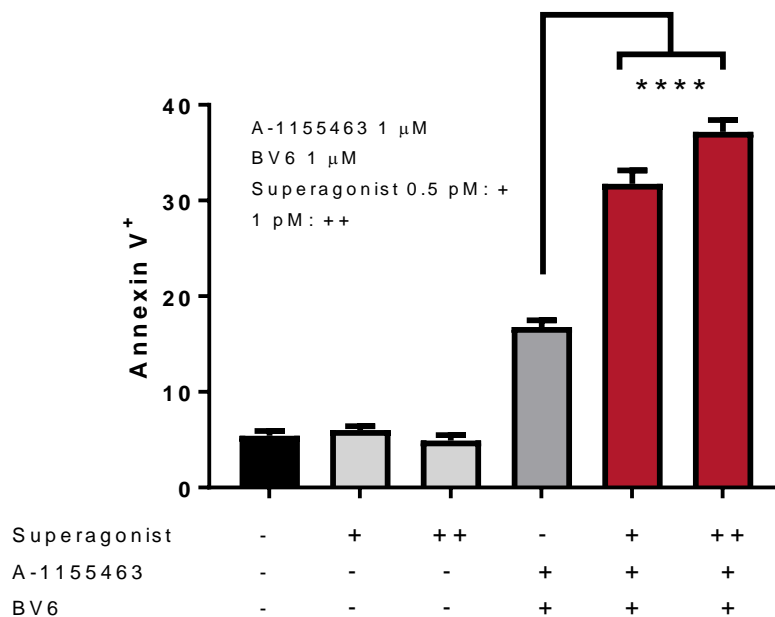


Figure 33: Flow cytometry data shows increased cytotoxicity (positive Annexin V staining) in for combination treatment conditions in RKO cells.

A-1155463 (A-11) is BCL-X_L inhibitor. One-way analysis of variance (ANOVA) followed by Bonferroni multiple comparisons test was used to establish significance between A-11/ BV6 (dark gray) and A-11/BV6/DRA for both DRA concentrations (red). ****p<0.0001.

Immunoblotting from extracts derived from RKO cells treated with DMSO control, A-1155463 (A-11), BV6, DRA, and dual/triple combinations reveal that proapoptotic extrinsic and intrinsic pathway caspases 3, 8, and 9, and Bid, are activated by the drug combinations (Figure 34). Activation of these proapoptotic proteins is assessed by increased appearance of their cleavage products. For instance, comparing blots at 6 h and 16 h, DRA combination with BV6 increases the appearance of lower molecular weight fragments (19 kDa and 17 kDa) of pro-apoptotic protein caspase 3 (35 kDa).

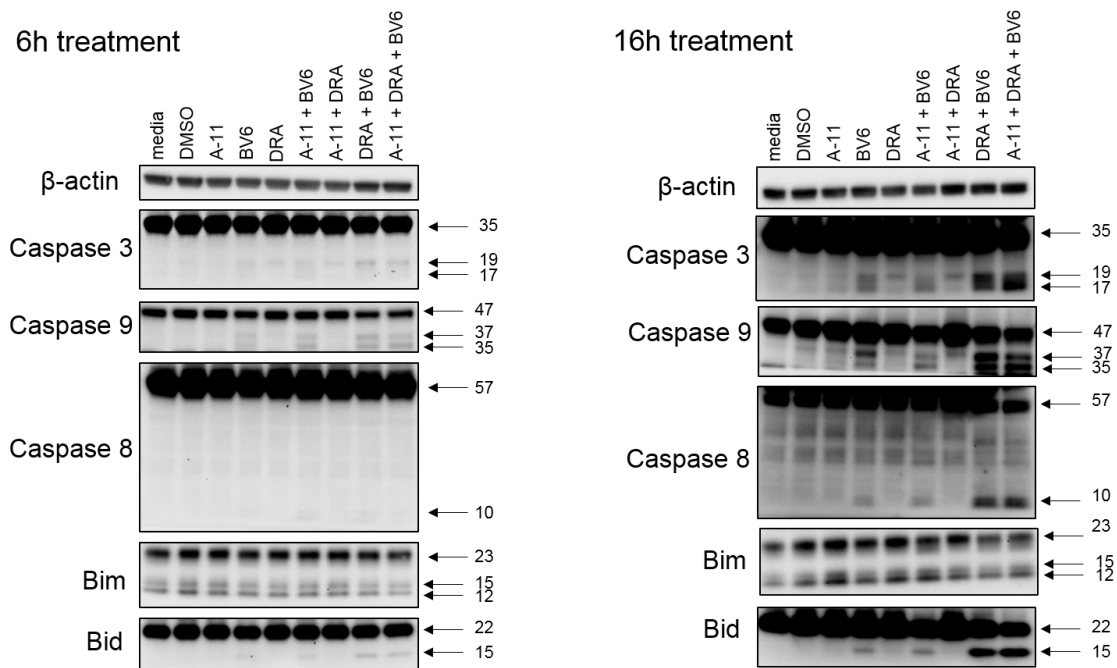


Figure 34: Increased extrinsic and intrinsic pathway activation observed with combination treatments.

Immunoblots of apoptotic pathway proteins in RKO cells 6 h (left) and 16 h (right) after treatment. Vehicle control was DMSO, A-11 refers to BCL-X_L inhibitor A-1155463, and BV6 is the XIAP inhibitor. Cell were treated for 6 h (left) or 16 h (right) as follows: 1.5 pM DRA; 2 μM each A-11 and BV6. β-actin was used as a loading control. Numbers to the right of each blot indicate full-length protein size (higher molecular weight) and

cleavage products resulting from activation of protein (lower molecular weight fragments).

4.4 Significance

Interestingly, among the many cancer pathways interrogated in the screens, a number of primary hits were genes within the extrinsic/intrinsic pathways, suggesting that failure of DRA monotherapies is driven by an inability to fully engage the cell death machinery. The screen nominated the gene for XIAP, an antiapoptotic protein, as the greatest driver of resistance to both TRAIL and DRA in human colorectal cancer cell line RKO. This result validates the robustness of the screen, as many studies in the literature have suggested XIAP as a key driver of TRAIL resistance (94-98, 100). The genetic screen then streamlined the testing of potential targeted small molecules that specifically inhibit proteins associated with DRA resistance instead of simply combining DRA with standard-of-care chemotherapeutics.

The “druggable” targets were linked to associated, clinically viable small molecule drugs and tested in combination with DRA to identify the cocktails that most effectively overcome DRA resistance. This unbiased approach does not tailor combination options to conventional knowledge of signaling pathways associated with the drug of interest, and instead scans a plethora of potential cancer death and survival pathways to evaluate the most important mechanisms of resistance. In Chapter 5, we integrate the results from Chapter 3 and 4 to evaluate the efficacy of our delivery and drug combination strategies in an *in vivo* patient-derived xenograft model.

5. Integration of delivery and genomics to improve DRA efficacy in patient-derived xenografts

5.1 Introduction

Upon establishing the efficacy of our delivery and drug combination design strategies individually, we set about testing the combination treatments and ELP-DRA depot in a DRA-resistant patient-derived xenograft (PDX) model, CRC247. We hypothesized that PDX treatment with optimized combination(s) of sensitizers discussed in Chapter 4 and the sustained release ELP-DRA depot formulation would result in tumor regression and improved survival rates compared to treatment with single agents.

5.2 Materials and methods

5.2.1 Cell lines and cell viability assays

Cell lines. All cell lines were grown at 37°C in 5% CO₂. RKO were cultured in MEM Earle's (10% FBS, pyruvate, NEAA, 1% P/S). Cell lines were purchased within 6 months from Duke CCF or ATCC and patient-derived lines were obtained from David Hsu (Duke University) and passaged less than 10 times. All cell lines were authenticated using Promega PowerPlex 18D kit for short tandem repeat (STR) analysis or were purchased within 6 months from Duke CCF. All cell lines were tested for mycoplasma by Duke CCF. FBS: fetal bovine serum (GIBCO); P/S: penicillin/streptomycin (Thermo Fisher). Media was purchased from GIBCO or Sigma Aldrich.

In Vitro Cell Viability Testing. For single-agent cytotoxicity evaluation, drugs were tested *in vitro* using a luminescent cell viability assay method as follows. The cells were plated in white 96 well plates at a density of 2,000-10,000 cells/well in 90 μ L of complete media (RPMI 1640+10% FBS) and incubated for 12-18 hours at 37°C with 5% CO₂. The cells were then treated with 10 μ L additional media containing a serial dilution of the drug(s) of interest. All treatments were done in triplicate. After 72 hours, the Promega Cell Titer Glo reagent was used according to manufacturer's instructions to assay the number of viable cells; it is an accepted luminescent cell viability assay method. The cell viability was determined using measurements of luminescence using a plate reader. The dose response curves were generated by plotting percent viable cells v. compound concentration. The dose response curve was approximated from the scatter plot using a four-parameter logistic model calculation, and EC₅₀ was calculated as the concentration of drug required to kill 50% of the cells.

For combination treatments, the cell viability assays were carried out as follows. Colorectal cancer cells were plated in white 96 well plates at a density of 2,000 cells/well in 90 μ L of complete media (RPMI 1640+10% FBS) and incubated overnight at 37°C with 5% CO₂. Drugs used to enhance the sensitivity of cells to the death receptor agonists (DRAs) are referred to as "sensitizing drugs." Sensitizing drugs were dosed at a single concentration, or "background dose", which was chosen below the GI₅₀ in each cell line. The cells were treated with 10 μ L media containing the serial dilution of death receptor

agonist and a background dose of sensitizing drug(s). The treatments were done in triplicate to account for technical variability. After 72 hours, the Promega Cell Titer Glo reagent was used according to manufacturer's instructions to assay the number of viable cells; it is an accepted luminescent cell viability assay method. The cell viability was determined using measurements of luminescence using a plate reader. The dose response curves were generated by plotting per cent viable cells v. DRA concentration. Cell viability was normalized to the viability of the cells treated with the background dose of sensitizer only such that the effects seen are truly associated with DRA. The dose response curve was approximated from the scatter plot using a four-parameter logistic model calculation, and EC₅₀ was calculated as the concentration of DRA required to kill 50% of the cells.

5.2.2 *In vivo* patient-derived xenograft study

All tumor studies were completed in athymic nude/nude female mice 5-7 weeks old (Jackson Labs), and treatment commenced when tumor size reached approximately 100-120 mm³ (as measured by digital caliper and calculated as LxWx0.5). Colo205 engraftment was performed by subcutaneous injection of 1 million cells in the right flank. Colo205 xenografted mice were treated with one single injection on Day 0. CRC247 patient-derived cells were engrafted subcutaneously at 3 million cells per mouse. On Day 0, treatment commenced with daily oral gavage for A-1331852 in previously described vehicle (101), twice weekly i.p. injection of BV6 in sterile saline,

and/or weekly subcutaneous injection of ELP-DRA. All mice were monitored daily to ensure weight loss did not occur beyond 15%; mice were also evaluated for general body condition and mobility. Doses were chosen based on a small pilot study in which drug combinations were administered and mice were monitored for visible distress and unacceptable (>15%) weight loss.

5.3 Results and discussion

5.3.1 Selection of drug combinations for *in vivo* studies

Prior to *in vivo* efficacy studies, a series of cell viability assays were conducted to confirm activity of the intended drug combinations (Figure 35). An improved BCL-X_L inhibitor, A-1331852 had become available; this drug is orally bioavailable and exhibits 10X the potency of A-1155463 (101). Thus, testing of A-1331852 in combination with DRA and BV6 or Palbociclib was necessary to ensure *in vitro* efficacy before proceeding with tumor regression studies. These studies were first conducted with DRA-resistant RKO cells, as this was the original cell line used for the CRISPR/Cas9 knockout screen. The cell viability studies confirmed that A-1331852 (A-13) is a potent sensitizer of RKO cells to the DRA, and addition of Palbociclib (Palbo) or BV6 result in picomolar or subpicomolar DRA EC₅₀ respectively (Figure 36).

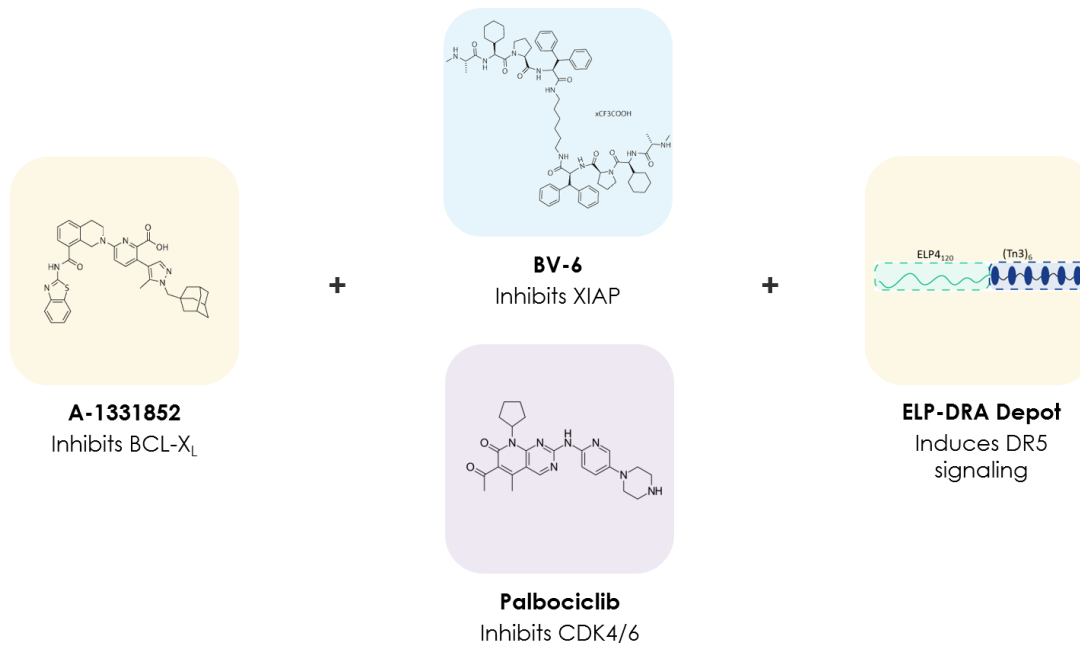


Figure 35: Selected drug combinations for *in vivo* tumor regression studies. BCL-X_L inhibitor A-1331852 was paired with XIAP inhibitor BV6 or CDK4/6 inhibitor palbociclib. Sensitizer pairs were administered in combination with the sustained release depot of ELP-DRA.

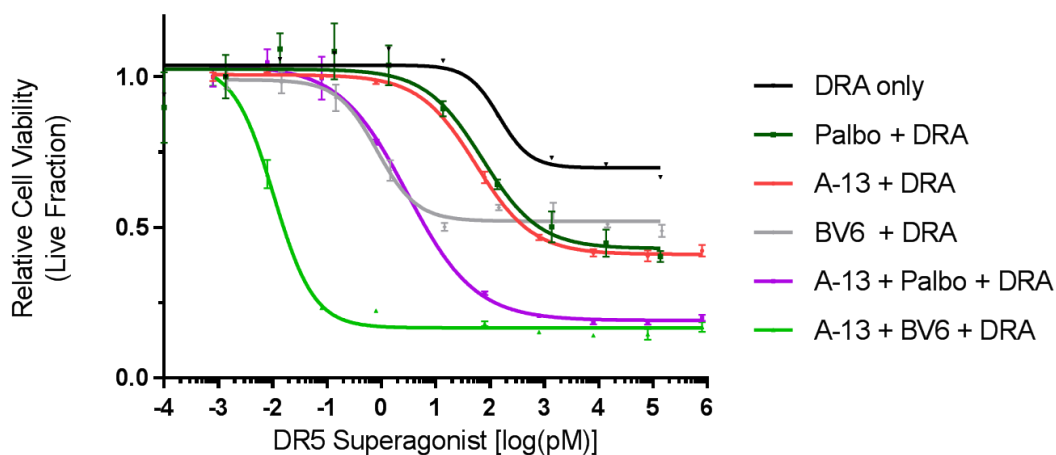


Figure 36: A-1331852 potently sensitizes RKO cells to DRA *in vitro*. Cell viability assay confirms efficacy of BCL-X_L inhibitor A-1331852 (A-13) in human CRC cell line RKO. Combination of A-1331852 and palbociclib (Palbo) or BV6 results in DRA EC₅₀ of 3 pM (purple) or 0.01 pM (green) respectively.

We selected CRC247 DRA-resistant patient-derived xenografts as the *in vivo* model for drug combination evaluation. While *in vitro* combination studies were underway, a small *in vivo* pilot study was conducted in nude mice to assess toxicity of double drug combinations BV6+A-13 and Palbo+A-13. As discussed in section 5.3.2, Palbociclib combination with A-13 was extremely toxic. Thus, the remainder of the *in vitro* studies described in this section focus primarily on A-13 + BV6 combinations. The DRA has poor efficacy in the CRC247 cell line derived from the same tumor, but as predicted by the RKO drug combination studies, *in vitro* treatment with the XIAP inhibitor BV6 (B) or the orally bioavailable BCL-X_L inhibitor A-13 resulted in sensitization to DRA. Treatment with all three drugs, A-13+BV6+DRA resulted in subpicomolar EC₅₀ and >96% cell kill in a three-day *in vitro* assay (Figure 37). Importantly, no toxicity was observed at these background doses of A-13 and BV6 (Figure 38).

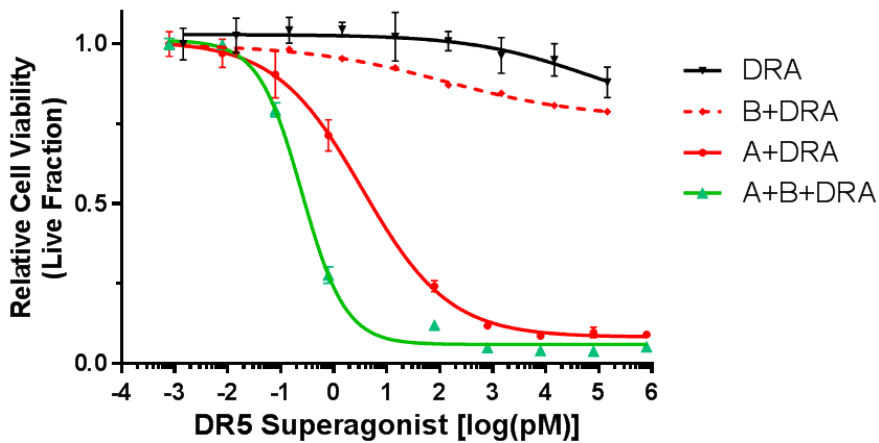


Figure 37: A-1331852 potently sensitizes patient-derived CRC247 cells to DRA.

Cell viability data shows efficacy of triple drug treatment with A-1331852, BV6, and DRA (A+B+DRA, green) compared to double drug treatments (red).

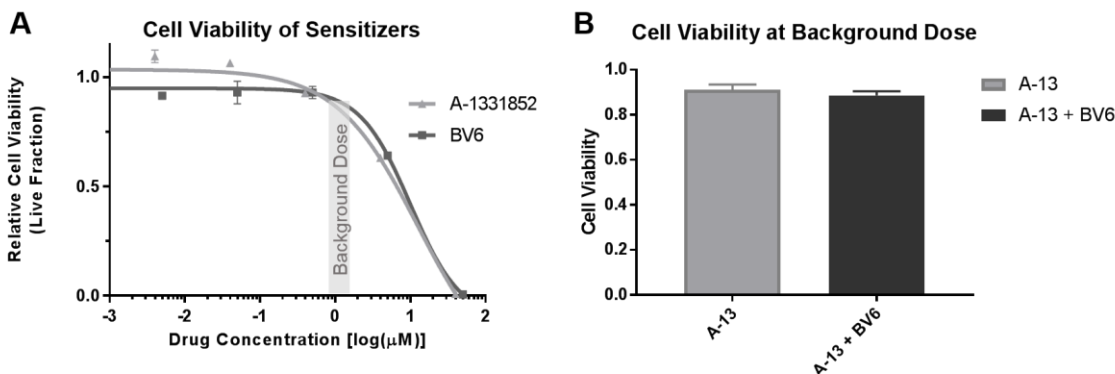


Figure 38: Cell viability assay of single agent sensitizers in CRC247 cells.

(A) Doses of BV6 and A-1331852 (A-13) chosen for background dose of sensitizers in combination treatments with DRA *in vitro* were minimally toxic to CRC247s. (B) Combination of A-1331852 and BV6 at the chosen background doses (2 μ M and 1 μ M respectively) is not toxic to CRC247s.

Finally, the ELP-DRA used for depot formulation was validated for *in vitro* efficacy when combined with A-13 and/or BV6. As shown in Figure 39, triple drug combination of A-1331852 + BV6 with either DRA or ELP-DRA exhibit nearly identical EC_{50} of 3.3 or 3.8 pM in DRA-resistant patient-derived CRC247 cells. ELP-DRA will be used for sustained release of the DRA from a subcutaneous depot in drug combination studies *in vivo*. Section 5.3.2 describes a small *in vivo* pilot study assessing the toxicity of various doses of sensitizer drugs before addition of ELP-DRA.

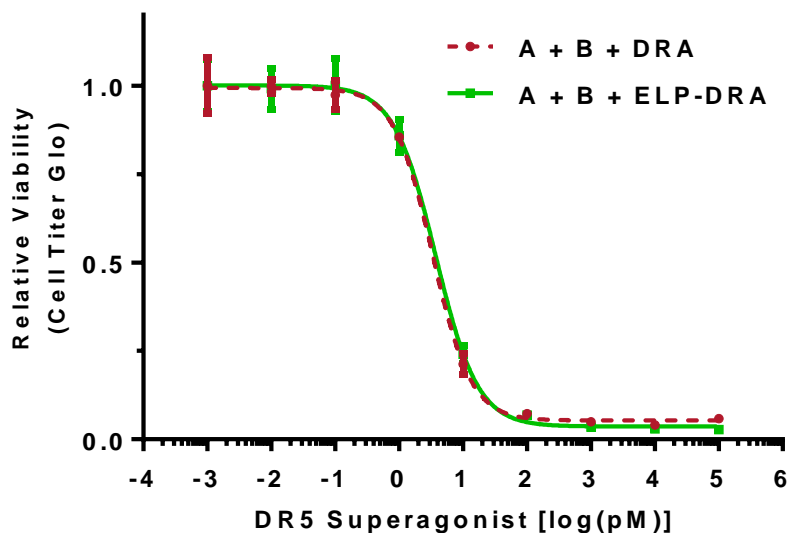


Figure 39: ELP-DRA is equally potent as DRA when combined with sensitizer drugs in patient-derived CRC247 cells.

Cell viability assays confirm the potency of ELP-DRA when combined with A-1331852 and BV6 sensitizers in human CRC247 cells.

5.3.2 Pilot *in vivo* study for toxicity evaluation

A small pilot study was conducted in nude mice to evaluate toxicity of double sensitizer combinations at a range of doses. A-1331852 (A-13) is an oral drug, and its vehicle is different from Palbociclib, which can be administered orally or intraperitoneally. To avoid potential trauma associated with multiple daily dosing of these drugs, we administered Palbociclib intraperitoneally and A-13 orally. We chose a dose of 25 mg/kg for A-13, as this dose ensures *in vivo* activity according to data available in the literature (101). Daily administration of A-13 at this dosage did not affect body weight or cause visible signs of toxicity. Palbociclib dosing was first tested at 50 mg/kg in combination with A-13. Unfortunately, this combined dose of Palbociclib and

A-13 caused visible toxicity in the mice, resulting in lowered body temperature, reduced mobility, closed eyes, and/or sudden death. Thus, lower doses (25 mg/kg and 12.5 mg/kg) of Palbociclib were tested in combination with 25 mg/kg A-13 (Figure 40). However, these doses were still too toxic, as mice continued to lose weight each day, never recovering to compensate for the previous day (Figure 40). Within one week, mice lost more than 15% of their body weight; the 25 mg/kg and 12.5 mg/kg doses were therefore too toxic for drug combination studies. A lower 6.25 mg/kg dosage of Palbociclib was also tested in combination with A-13, and an introductory test in which 30 mg/kg ELP-DRA was added to the treatment combination caused rapid deterioration in body condition over the course of 2 weeks. Change in dosing frequency was also considered, but the half-life of Palbociclib is only a few hours, making this option infeasible (102).

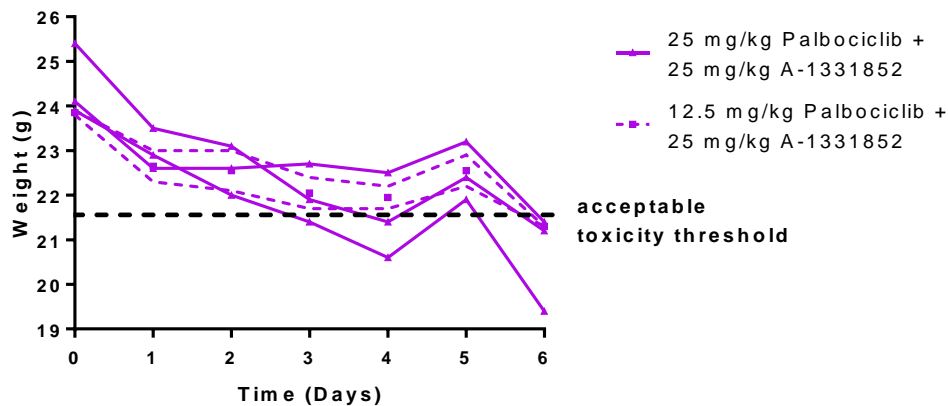


Figure 40: Weight loss data for animals treated with A-1331852 in combination with palbociclib.

Nude mice were given daily doses of 25 mg/kg A-1331852 (p.o.) and 25 mg/kg or 12.5 mg/kg palbociclib (i.p.). Toxicity defined as weight loss >15% of pre-treatment weight.

These results prompted a shift of focus to the sensitizer combination of A-1331852 with BV6 for the remainder of the *in vivo* studies. Mice treated daily with oral A-1331852 at 25 mg/kg and twice weekly with BV6 (*i.p.*) did not experience visible changes in body condition or movement, and despite initial weight loss, regained and maintained acceptable body weight for the duration of the study. Addition of weekly subcutaneous administration of ELP-DRA did not significantly affect weight (Figure 41).

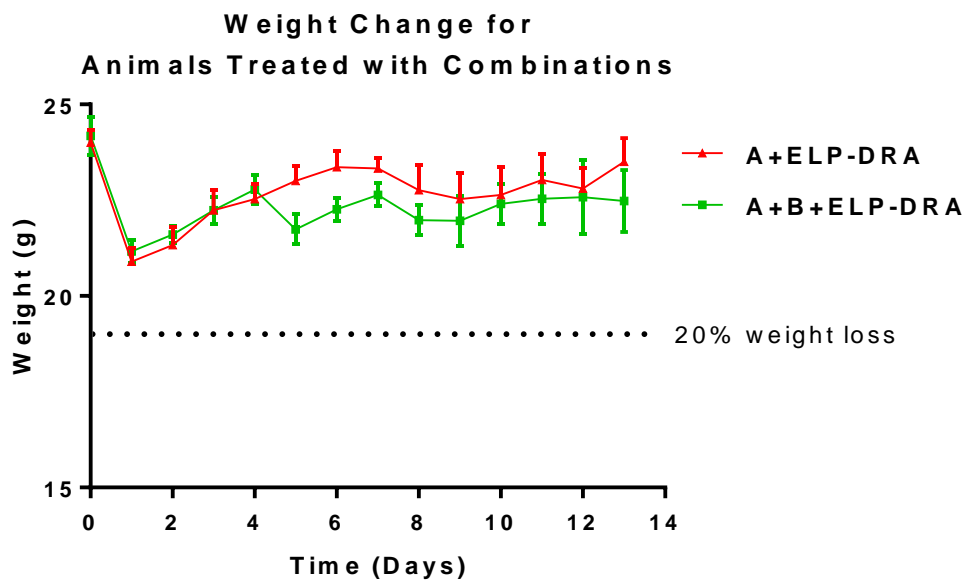


Figure 41: Combination of DRA with XIAP and BCL-X_L inhibitors is tolerable *in vivo* in patient-derived xenografts.

The mice in the double (A-1331852+ELP-DRA, red) and triple (A-1331852+BV6+ELP-DRA, green) treatment groups experience some weight loss (<15%) the day after treatment commences, but as the study continues, they experience weight gain and plateau. Weight loss does not exceed 20%. A: A-1331852; B: BV6.

5.3.3 *In vivo* tumor regression study confirms superior efficacy of rationally designed drug combinations

To assess *in vivo* efficacy of the triple treatment compared to single drugs or double combinations, we performed a tumor growth study in CRC247 patient-derived xenografts. The triple combination effectively shrank tumors for one week and slowed tumor growth in the following days, with significant differences between the triple drug combination and all other groups between days 5 and 13 (Figure 42A, B). Treatment with single drugs A-13 (daily p.o. 25 mg/kg), BV6 (q4d i.p. 5 mg/kg), or DRA (30 mg/kg s.c. weekly) resulted in slowed tumor growth compared to mice in the vehicle control group, but the A+B+DRA triple drug treatment suppresses tumor growth significantly more effectively (Figure 42A). Treatment with double drug combinations A-13+BV6, BV6+DRA, and A-13+DRA are well tolerated and slow tumor growth, but addition of the third drug in the A-13+BV6+DRA treatment group results in shrinkage and significantly slower tumor growth over time (Figure 42B, Appendix C).

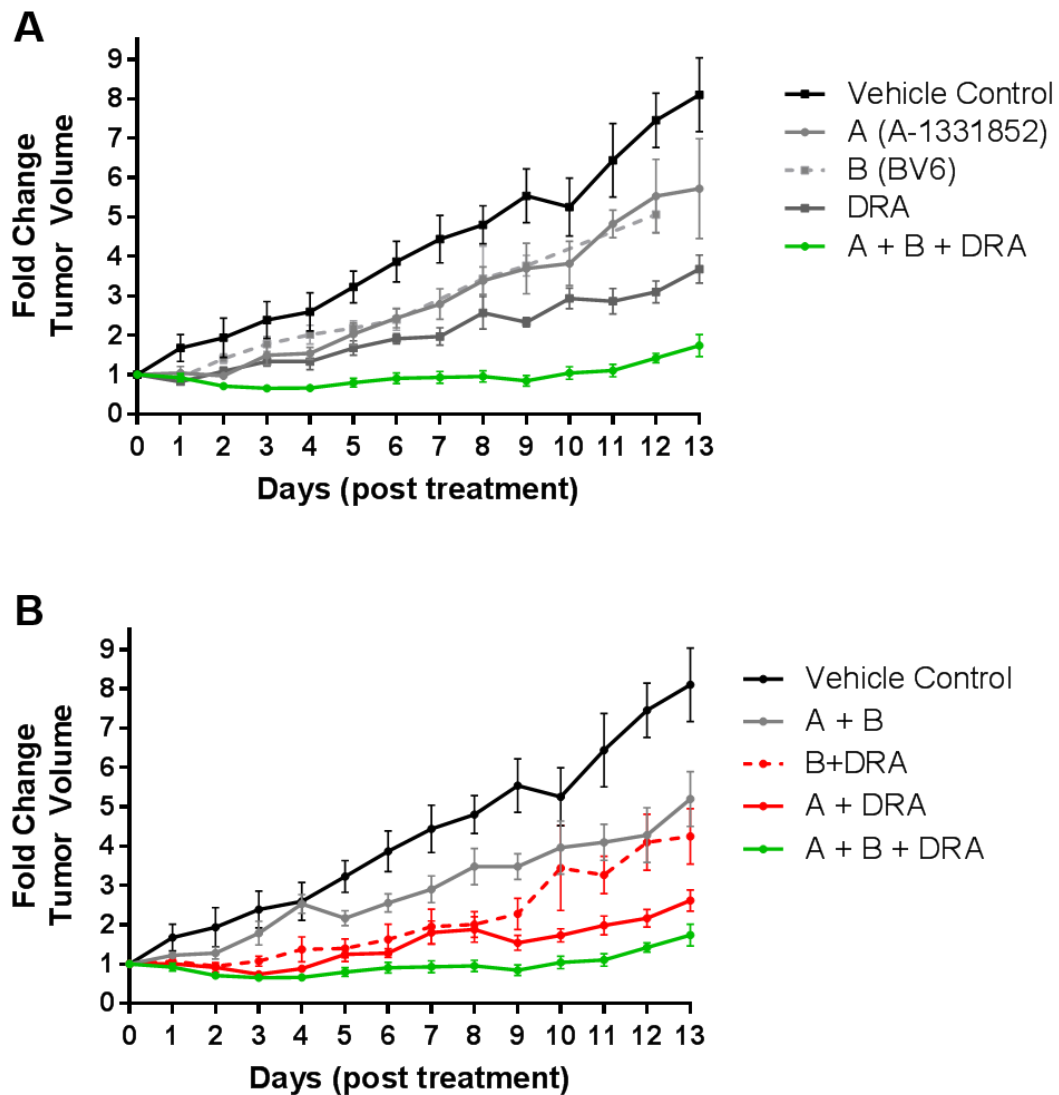


Figure 42: CRC247 PDX data demonstrates in vivo efficacy of the A+B+DRA compared to other treatment groups.

DRA formulation used in these plots was ELP-DRA and abbreviated to “DRA” in descriptions. Tumor regression data; mice were treated with A-1331852 (25 mg/kg daily p.o.) and/or BV6 (5 mg/kg q.4.d.), and/or ELP-DRA (30 mg/kg weekly s.c.). (A) Comparison of treatment triple drug combination with single agents. (B) Comparison of treatment with triple drug combination with double agents. Data were analyzed using two-way analysis of variance (ANOVA) of matched values followed by Fisher’s LSD multiple comparisons test to establish significance ($p < 0.05$) of the difference between groups at each day of treatment. Results indicate statistically significant tumor volumes between and including days 5 and 13 for triple combination of A-1331852 + BV6 + ELP-DRA compared to other groups.

Survival data corroborates the advantage of having all three drugs in combination, as mice in this group outlived those in all other groups (Figure 43). These *in vivo* results recapitulate those seen *in vitro*, providing affirmative evidence for the potential utility of this platform.

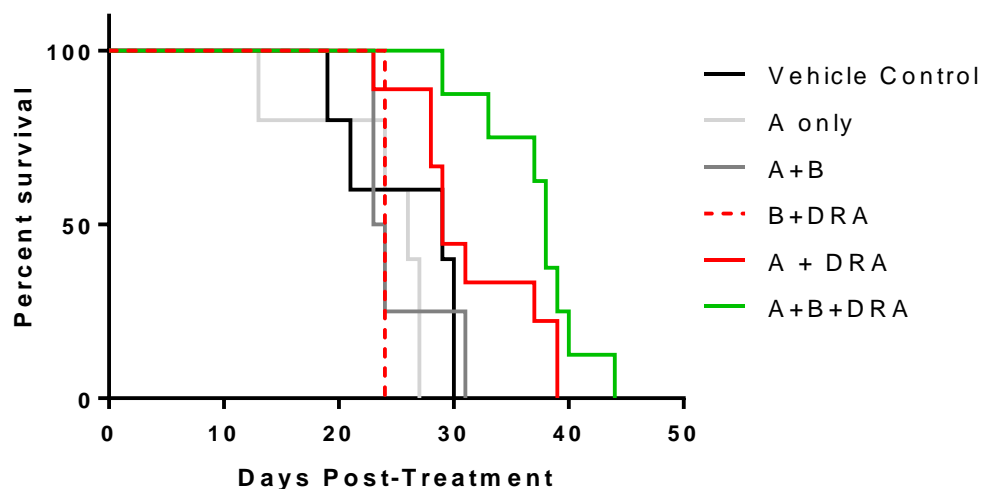


Figure 43: Kaplan-Meier survival analysis results.

Comparison of key treatment groups indicates that median survival increases from 29 to 38 days when BV6 (B) is added to the A-1331852 (A) + ELP-DRA (“DRA”) combination. A Gehan-Beslow-Wilcoxon test demonstrated statistically significant difference in survival between double drug combination of A-1331852 + ELP-DRA and triple drug combination A-1331852 + BV6 + ELP-DRA ($p < 0.05$).

5.4 Significance

In this chapter, we have simultaneously addressed the delivery, potency, and resistance issues of the DRA. An ELP-based protein delivery strategy was used to prolong DRA residence time *in vivo*. Functional genomics screens had revealed the genetic drivers of resistance to the DRA, and informed the selection of drug

combinations to overcome DRA resistance. Here, we integrated the two strategies to achieve *in vivo* tumor regression of DRA-resistant patient-derived xenografts (PDX), demonstrating significant anti-tumor efficacy when combining BCL-X_L inhibition with A-1331852, with or without the XIAP inhibitor BV6, with the ELP-DRA conjugate.

A major potential limitation of most combination anti-tumor therapies like A-1331852/BV6/DRA is toxicity. The doses used in this study were based on a small pilot maximum tolerated dose (MTD) experiment and not fully optimized, and a rigorous optimization study may enable lowering of drug doses. Even so, we achieved encouraging *in vivo* results with lower doses of each drug compared to doses used in the literature. For instance, A-1331852 was given twice daily in combination with venetoclax in order to achieve effective tumor regression *in vivo* (101), while we administered the drug only once a day to reduce potential toxicity. Similarly, BV6 was administered at 10 mg/kg for synergism with another death receptor agonist that had not been modified for improved delivery(96). Here, mice were treated with only 5 mg/kg BV6 at each injection. In addition, instead of daily dosing of the death receptor agonist, the slow release formulation enabled DRA administration only once per week(14). This aspect of our work is encouraging, especially because the major reported dose-limiting toxicities (DLTs) for each class of drug used in this study do not overlap with one another. For instance, IAP inhibitor DLTs have been associated with cytokine release syndrome in patients, while BCL-X_L inhibition is limited by thrombocytopenia due to the induction of

platelet death (103, 104). DRAs, on the other hand, have historically been associated with potential hepatotoxicity concerns (104). Thus, by taking advantage of their highly synergistic anti-tumor activities, the therapeutic combinations described here have the potential to be safely administered to patients at active doses. Further, next generations of this system will combine the ELP-DRA with small molecule encapsulation to promote targeted tumor uptake and minimization of toxicities in non-tumor tissues.

Finally, the approaches described here may serve broadly as a springboard for the design of other protein drug-based combination therapies that combine high specific activity, favorable delivery properties, and minimal resistance barriers, thereby unlocking the potential of agents that may otherwise fail to exhibit single-agent activity.

6. Conclusions

6.1 Platform summary and application for broad use

Targeted protein drugs can be powerful anti-cancer agents, as their specificity and selectivity make them ideal for manipulation of tumor cell signaling. Current approaches to preclinical development of protein therapeutics often overlook the inevitable issue of cancer drug resistance. This dissertation presents a platform that maximizes translatability of targeted protein drugs and is broadly applicable for use by the biomedical community. A collaborative approach for addressing resistance and delivery issues at the preclinical level, the platform uses genetic screening and protein engineering respectively. Our proof-of-concept studies explored CRC treatment with a pro-apoptotic death receptor agonist (DRA). Despite the preclinical promise of pro-apoptotic DRAs over the past two decades, this class of drugs has repeatedly failed at the clinical stage, primarily due to cancer drug resistance and inadequate drug delivery, making it an excellent model protein for our approach.

To identify genetic drivers of CRC resistance to the DRA, an ORF gain-of-function screen and CRISPR/Cas9 loss-of-function screen were used. Screen results guided the design of highly potent drug combinations that overcame CRC cell resistance. A series of *in vitro* experiments revealed two optimal formulations that, with remarkable synergism, effectively reversed DRA resistance in patient-derived CRC cells:

combination of DRA with anti-apoptotic inhibitors and/or cyclin dependent kinase inhibitors.

Although rationally designed drug combinations could dramatically improve the clinical outcome of new drugs, severe systemic toxicity may preclude their use. As seen in Chapter 5, *in vivo* tumor regression studies combining DRA with a BCL-X_L inhibitor confirm dramatic synergy, while addition of a third drug demonstrated dose-limiting toxicity. Maximum tolerated dose (MTD) studies would enable design of drug regimens that delay disease progression in highly DRA-resistant patient derived xenograft (PDX) murine models. A natural and necessary extension of the platform is the development of multimodal nanoparticles, in which small molecule inhibitors are encapsulated in the core of targeted DRA nanoparticles. Nanoparticle encapsulation could improve pharmacokinetic properties of the small molecule drugs and reduce their systemic toxicity.

Our multipronged strategy is broadly applicable, as it enables the identification and optimization of potent combinations that overcome drug resistance to a protein drug of interest. Functional genomics screens are used to identify genetic drivers of resistance to the protein drug in human cancer cells, and the results of the screens are used to select commercially available small molecule inhibitors to test in combination with the protein drug. Cytotoxicity assays, clonogenics, and time-to-progression experiments reveal optimal formulations that effectively reversed DRA resistance in

patient-derived human cancer cells. A sustained release formulation of the protein drug can improve its chances of clinical feasibility. To address potential toxicity issues associated with potent drug combinations, the strategy can be extended to include nanoparticle formulations of the small molecule drugs.

6.2 Future Perspectives: Integrating genomics and drug delivery

Genomic tools, such as single-cell and deep sequencing, allow for high-throughput monitoring of tumor microenvironment, immune composition, mutational load, and tumor neoantigens. These data can be used to determine the most important factors for treatment of individual tumors. While recent advances in immuno-oncology demonstrate the promise of targeted therapies to overcome cancer immune evasion, it has become increasingly clear that a one-size-fits-all approach is incompatible with the diversity of immunophenotypes. Structural genomics can effectively select for predictive determinants of patient response and elucidate targets for individualized therapy within the tumor and tumor microenvironment. For example, recent work demonstrates the power of using gene set enrichment analysis (GSEA) to dissect the tumor microenvironment in a large cohort of colorectal cancer patients. This high resolution genomic analysis revealed the diversity of tumor escape mechanisms and cancer-germline antigens and identified novel immunotherapeutic targets (105).

Although integrated genomic analysis provides novel and clarifying insights into the interactions between tumor biology and the immune system, translation of the

results to clinical benefit requires drug delivery considerations. For instance, although CCR8 inhibition could block metastasis, there is an inevitable challenge of balancing desired efficacy with acceptable toxicity. To combat this challenge, incorporation of drug delivery strategies can dramatically affect feasibility and clinical relevance. For example, a recent study illuminated the power of drug delivery in overcoming dose-limiting toxicity associated with combinations of immunotherapeutic agents anti-CD137 and IL-2 (106). While these immunostimulatory agents generated effective anti-tumor immunity, deadly systemic toxicity thwarted clinical application. To address this issue, Irvine and colleagues anchored the two proteins on the surface of nanoliposomes, promoting rapid accumulation in the tumor, reducing systemic exposure, maintaining anticancer efficacy, and demonstrating desired immunostimulatory effects in the tumor microenvironment (106). Another immunotherapy strategy, adoptive T-cell therapy, has led to exceptional responses in patients with B cell malignancies and disappointing results in those with solid tumors. Whole exome- and transcriptome sequencing for evaluation of neoantigen load and mutational burden may predict clinical benefit; early stage evaluation can guide T-cell therapy design, elicit efficient epitope expansion, and improve clinical response. Mooney and colleagues have directly demonstrated the ability to use synthetic scaffolds to mimic antigen-presenting cells and cue expansion of desired T-cell types, highlighting the potential for greater overlap between biomaterials, genomics, and immunotherapy (107).

We propose that collaboration between drug delivery and genomics experts can streamline the path to clinical translation and success. While drug delivery can transform the clinical feasibility of the desired drugs, structural genomics can predict and identify correct targets and individualized therapies for patients. Inevitably, however, cancer drug resistance impedes long-term efficacy of treatment. There is a monumental effort to overcome this challenge using integrated functional genomics.

Functional genomics assays such as gain-of-function open reading frame (ORF) library screens and loss-of-function small interfering RNA (siRNA) or CRISPR Cas9 screens have been used to identify genetic drivers of cancer drug resistance (83). Despite the success of these screens in identifying potential combination targeted drug candidates for overcoming or forestalling drug resistance at the preclinical level, translation of these opportunities to clinical use has proved difficult. One common reason for the disconnect between preclinical promise and clinical feasibility is intolerable additive or synergistic on-target toxicity. In a recent study, a pathway-activating genetic screen was used to investigate acquired resistance of acute myeloid leukemia (AML) to Bcl-2 inhibitor ABT-199. Mcl-1 upregulation was identified as a key mediator of resistance, and its inhibition reversed or completely forestalled acquired ABT-199 resistance of AML cell lines (108). Subsequent work by another group demonstrated that combination of ABT-199 and targeted Mcl-1 inhibitor A-121047 synergistically induces apoptosis between in AML cell lines (109). Unfortunately, this

combination was also toxic to normal peripheral mononuclear cells (PMNCs), and the authors suggested that direct Mcl-1 inhibition may not be a clinically viable approach. We offer an alternative perspective: perhaps the drug combination would be clinically relevant with the right drug delivery system. A diverse assortment of nanoparticle drugs has been combined with laser treatments to allow for modulation of the tumor or its microenvironment and improved drug delivery. In a recent study, pyruvate-targeted nanoparticles were used to produce reactive oxygen species (ROS) in mitochondria upon irradiation of tumor cells with a near-infrared laser. This approach reduced expression of efflux pumps that caused multidrug resistance in cancer cells, generating a therapeutic window for treatment of cells with the chemotherapeutic drug doxorubicin (64). Although this drug is adequate for proof-of-concept, the choice is symptomatic of a common pattern in drug delivery research: new delivery strategies are often applied to established, clinically approved drugs. We believe that direct collaborations between oncologists, pharmacologists, and biomedical engineers will result in faster, more meaningful progress. The most promising new targeted therapies should be top priority for drug delivery experts once proof-of-concept studies are completed. Importantly, this streamlined approach of using genomics to identify rational drug combinations and following through with drug delivery optimization would promote the use of drug cocktails that would be otherwise overlooked.

Ultimately, time is of the absolute essence for cancer patients, and the fusion of strategies between the fields of genomics and drug delivery could accelerate the timeline of preclinical and clinical testing. Instead of clinical trials failing due to lack of patient stratification, acquired drug resistance, or toxicity, collaborative drug development can help us anticipate these issues at the preclinical level, providing a more solid foundation for clinical testing and a higher likelihood of success. Serial tumor profiling throughout a patient's process can be crucial for determining robust biomarkers that predict response or portend resistance. This genetic information can inform prioritization of desired treatment strategies and unveil the most clinically desirable drug combinations, pointing drug delivery experts to the most impactful research. Last year, The Cancer Genome Atlas research network published its findings from genomic and molecular characterization of over 200 primary cervical cancers (110). The authors concluded that a majority of cervical cancers exhibited genomic alterations in the PI3K–MAPK and/or TGF β signaling pathways, suggesting that modulatory drugs affecting these pathways could have tremendous clinical benefit. Unfortunately, the toxicity-induced adverse effects have severely limited the therapeutic window of many PI3K inhibitors. Thus, there is an urgent need for drug delivery researchers to shift toward choosing such problematic but promising small molecule drugs for testing or application of delivery systems. To offset the cost of doing so, funding agencies should place heavier weight on direct collaborations between pharmacologists and biomedical engineers.

Here, we offer some guiding principles that have come to light through the course of the work presented in this dissertation. Below, we have listed key questions for researchers in each field, and hope that these considerations will provide each side with a more holistic view of cancer research.

Drug delivery experts:

-How can I apply enhanced drug delivery vehicles to incorporate rationally selected targeted therapies, consistent with structural and functional genomics information for the tumor type(s) of interest?

-How will my drug delivery platform affect the tumor's signaling pathways and resistance mechanisms?

Genomics experts:

-If dose-limiting toxicity was not a factor, what would be the most successful small molecule drug combination based on my genetic screens and functional assays?

-Are there opportunities to combine standard therapies with those that manipulate the tumor microenvironment or infiltrating immune cells?

Appendix A

TRAILR-2-Specific Tn3 Amino Acid Sequence

GAIEVKDVTDTTALITWAKPWVDPPLWGCELTYGIKDVPGDRTTIDLQQKHTAY

SIGNLKPDEYEVS LICFDPYGMRSKPAKETFTT

Flexible GlySer Linker Amino Acid Sequence

GGGSGGGSGGGGS

His-8 Tag Amino Acid Sequence

HHHHHHHH

Periplasmic Secretion Signal OppA Amino Acid Sequence

MTNITKRSLVAAGVLAALMAGNVALAG

Appendix B

TRAIL

REP1

Gene	DM_mean	DM_median	three_score	GARP_score	sb_score	cum_rank
XIAP	0.2100	0.1044	0.0685	0.0505	0.0518	5
TKT	0.5978	0.4843	0.3605	0.2986	0.4666	21
BCL2L1	0.5857	0.4693	0.4187	0.3934	0.4096	23
CDK6	0.5733	0.4993	0.4360	0.4043	0.4920	31
NFKB2	0.5750	0.5300	0.4624	0.4286	0.4409	33
CDK2	0.6428	0.6163	0.4863	0.4213	0.5183	55
CDK9	0.6577	0.5795	0.5019	0.4632	0.4881	56
RAD21	0.6043	0.7386	0.4304	0.2763	0.3909	56
ENO3	0.6156	0.6141	0.4977	0.4395	0.5228	58
SPOP	0.6545	0.6565	0.4786	0.3896	0.5780	61
FGFR2	0.6219	0.6893	0.5325	0.4541	0.5003	69
SKP2	0.7017	0.6064	0.5066	0.4567	0.5153	69
HDAC8	0.6569	0.7421	0.4884	0.3615	0.4937	78
BCL2A1	0.6770	0.6019	0.5469	0.5194	0.5789	96
YAP1	0.6704	0.6727	0.5775	0.5300	0.5373	104
BDH1	0.8075	0.5676	0.5142	0.4875	0.4937	105
PPP2R1A	0.7729	0.6251	0.5319	0.4853	0.6022	113
PAF1	0.7903	0.7327	0.5400	0.4436	0.5050	121
ADSS	0.8037	0.6855	0.5426	0.4711	0.5809	125
PARP10	0.7695	0.7095	0.5631	0.4899	0.5487	127
SRSF2	0.8481	0.8174	0.4341	0.2425	0.2809	158
TALDO1	0.7598	0.7156	0.6110	0.5587	0.5888	162
TSHZ2	0.7260	0.7377	0.5804	0.5017	0.6889	185
MCL1	0.6887	0.7099	0.5967	0.5401	0.6898	189
TBL1XR1	0.7783	0.7638	0.5939	0.5090	0.6476	194
CDK8	0.6970	0.7218	0.6149	0.5614	0.6763	196
POU5F1	0.7235	0.7031	0.6234	0.5835	0.6834	212
PRKAB1	0.7111	0.7835	0.6394	0.5673	0.6271	218
GLI1	0.7056	0.6946	0.6238	0.5884	0.6929	221
MPL	0.7691	0.8257	0.6225	0.5210	0.6194	222
MAPK9	0.8574	0.6773	0.6099	0.5762	0.6223	227
CDK1	0.7597	0.7384	0.6354	0.5839	0.6633	232
MAP2K4	0.8558	0.8135	0.6175	0.5195	0.5198	235

VEZF1	0.7822	0.8069	0.6238	0.5323	0.6559	241
EPHA2	0.7528	0.7079	0.6549	0.6284	0.6336	242
USP9X	0.7402	0.8235	0.6532	0.5680	0.6123	245
SNAI1	0.7229	0.7506	0.6048	0.5319	0.7314	251
SLC2A1	0.8976	0.7199	0.6100	0.5550	0.6140	266
NCOA3	0.8533	0.7469	0.5893	0.5104	0.7048	269
PGAM1	0.7603	0.6769	0.6598	0.6512	0.6686	273
MAPK7	0.7741	0.7773	0.6733	0.6213	0.6254	282
CREBBP	0.8516	0.7217	0.6359	0.5930	0.6671	284
GLI3	0.7474	0.7724	0.6702	0.6191	0.6823	292
SLC16A3	0.7693	0.7068	0.6575	0.6329	0.6987	294
MAPK8IP1	0.7882	0.7660	0.6327	0.5661	0.7206	295
BCL2	0.8916	0.7330	0.6314	0.5807	0.6366	303
PKN3	0.8444	0.9047	0.6227	0.4817	0.5457	303
TSHR	0.7654	0.8319	0.6877	0.6156	0.6248	315
EPHA3	0.7941	0.8223	0.6768	0.6040	0.6617	324
KAT6A	0.8057	0.8437	0.6825	0.6018	0.6092	325
SF3B1	0.8472	0.9480	0.5553	0.3590	0.6069	325
HDAC6	0.8687	0.8355	0.6347	0.5343	0.6612	330
FH	0.8742	0.7032	0.6684	0.6510	0.6728	356
ACVR1B	0.8243	0.7969	0.6803	0.6219	0.7039	361
EPHB3	0.8435	0.8826	0.6743	0.5701	0.6226	363
HDAC4	0.8646	0.7436	0.6731	0.6379	0.6783	366
ENO1	0.7665	0.7906	0.6994	0.6538	0.6855	368
ESR1	0.7835	0.9534	0.6455	0.4916	0.6373	368
SMAD1	0.9637	0.7125	0.5851	0.5214	0.7087	373
ZEB1	0.9242	0.8492	0.6509	0.5517	0.5896	376
PGD	0.8421	1.0413	0.6000	0.3793	0.3805	377
CCNE1	0.7896	0.7355	0.6830	0.6567	0.7213	379
SMAD3	0.7267	0.8007	0.6651	0.5973	0.7778	379
EPHA10	0.9106	0.7582	0.6675	0.6222	0.6465	382
EPHA8	0.8045	0.8733	0.7040	0.6194	0.6328	389
EGR3	0.8522	0.7714	0.6856	0.6427	0.6958	391
RPIA	0.9762	0.7675	0.6389	0.5746	0.6101	393
MUSK	0.9507	0.7973	0.6211	0.5330	0.6960	399
HSP90AA1	0.7961	0.7694	0.6920	0.6533	0.7227	402
G6PD	0.8411	0.8824	0.6322	0.5070	0.7521	413
BMPR1B	0.7817	0.7357	0.6974	0.6783	0.7283	417

MAP3K1	0.8175	0.9438	0.6971	0.5737	0.6095	420
RAF1	0.8641	0.8775	0.6873	0.5922	0.6689	421
PKN1	0.7592	0.7623	0.6959	0.6627	0.7590	422
CDKN2C	0.8746	0.8510	0.6973	0.6204	0.6417	427
RPL5	0.8788	0.8884	0.6900	0.5908	0.6290	436
HDAC3	0.7993	0.8101	0.6932	0.6347	0.7531	439
DNMT1	0.9274	0.6921	0.6785	0.6717	0.6907	447
CDC42	0.8356	0.8728	0.7200	0.6435	0.6687	457
NOTCH4	0.8786	0.7534	0.6874	0.6545	0.7398	467
PDK3	0.8303	0.9071	0.7230	0.6310	0.6457	468
PRKACG	0.8953	0.8569	0.7086	0.6345	0.6440	473
HSP90AB1	0.9514	0.7090	0.6771	0.6611	0.6973	476
FGFR3	0.8518	0.8027	0.7286	0.6916	0.6996	490
RET	0.8699	0.7651	0.7087	0.6805	0.7393	504
GAPDH	0.8742	1.0085	0.6949	0.5381	0.6556	521
CDK3	0.8171	0.8214	0.7334	0.6894	0.7504	530
HIST1H3B	0.9531	0.8636	0.6823	0.5916	0.7100	530
CTNNA1	0.8297	0.9321	0.7246	0.6208	0.7126	532
DNMT3A	0.8915	0.8179	0.7238	0.6767	0.7160	537
CCND1	0.8549	0.8602	0.7290	0.6634	0.7313	549
EPHB2	0.9068	0.8704	0.7166	0.6397	0.7094	550
KIT	0.9178	0.8293	0.7247	0.6724	0.6911	550
ESRRB	0.8340	0.8218	0.7394	0.6982	0.7492	551
NEDD9	0.8843	1.0133	0.7173	0.5693	0.6246	551
ELF3	0.8326	0.9050	0.7246	0.6344	0.7429	552
MYCL	0.8915	0.8361	0.6899	0.6168	0.7993	552
HDAC5	0.8733	0.8863	0.7304	0.6524	0.7059	554
PRX	0.8473	0.9174	0.7482	0.6636	0.6670	554
BRD4	0.8309	0.8097	0.7398	0.7049	0.7613	559
MAPK8	0.8701	0.9265	0.7269	0.6271	0.7008	561
BLK	0.8268	0.8836	0.7190	0.6367	0.7825	565
SOX17	0.8845	0.7776	0.7128	0.6804	0.7753	565
PRKAR2B	0.8756	0.9519	0.7139	0.5950	0.7151	575
SMC1A	0.9639	1.0101	0.6896	0.5293	0.5942	576
FOXA2	0.9230	0.8409	0.6972	0.6253	0.7750	579
CTCF	0.8042	0.8154	0.7461	0.7115	0.7769	580
DDR1	0.8600	0.7641	0.7447	0.7351	0.7384	586
ACVR2A	0.9057	0.8434	0.7401	0.6885	0.7142	595

ERCC2	1.0123	1.0281	0.6693	0.4899	0.5407	600
SLC16A7	0.8430	0.9072	0.7528	0.6756	0.7229	608
SMC3	1.0663	0.9003	0.6243	0.4864	0.7245	611
MAP3K8	0.8912	0.8591	0.7446	0.6873	0.7361	619
SYK	0.8441	0.9031	0.7544	0.6800	0.7331	619
ACLY	0.8160	0.8142	0.7618	0.7356	0.7694	621
MYD88	0.8578	0.9170	0.7123	0.6099	0.8158	623
ControlA3	0.9090	0.9438	0.6921	0.5662	0.7763	623
TAF1	1.0701	0.8198	0.6565	0.5748	0.7651	630
HIST1H1C	0.8581	0.8544	0.7536	0.7032	0.7516	631
HDAC11	0.9443	0.8182	0.7050	0.6483	0.8129	639
GATA3	0.8545	0.7858	0.7632	0.7519	0.7592	648
TERT	0.8297	0.8329	0.7744	0.7451	0.7482	648
MYC	1.0405	1.0040	0.6526	0.4769	0.6963	651
HDAC10	0.8973	0.9722	0.7425	0.6277	0.7175	656
PRKAR2A	0.9729	0.8946	0.7353	0.6557	0.6948	660
REL	0.9017	0.8758	0.7541	0.6933	0.7363	662
NKX2-1	0.8708	0.8823	0.7693	0.7128	0.7200	663
PRKAG2	0.9531	0.8976	0.7089	0.6146	0.7837	672
PTCH1	0.8780	0.8537	0.7560	0.7072	0.7725	672
E2F3	0.9858	0.9432	0.7045	0.5852	0.7236	674
FGFR4	0.8819	0.8489	0.7602	0.7158	0.7608	680
PDK1	0.8251	0.8162	0.7812	0.7638	0.7756	680
PRKACA	0.9350	0.8685	0.7611	0.7073	0.7104	683
ERBB3	0.9251	0.9408	0.7412	0.6414	0.7318	685
ControlB2	0.8562	0.8369	0.7664	0.7311	0.7842	688
ALK	0.8419	0.8902	0.7515	0.6822	0.8499	705
SIN3A	0.9728	1.0649	0.7521	0.5957	0.6016	715
B4GALT3	0.8376	0.8290	0.7824	0.7590	0.8053	724
IDH3A	1.0088	0.8463	0.7484	0.6994	0.7171	728
CDK7	1.1576	0.8835	0.7143	0.6298	0.6850	730
CS	0.9409	1.0992	0.6965	0.4952	0.7647	732
PRKAR1A	0.8844	0.9347	0.7825	0.7063	0.7179	737
NOTCH1	0.8958	0.8652	0.7823	0.7408	0.7489	743
EPHA4	0.9404	0.8283	0.7640	0.7318	0.7662	745
MYCN	0.9050	0.8541	0.7640	0.7189	0.7935	746
TWIST1	0.8781	0.8698	0.7703	0.7206	0.8194	757
ESR2	0.8809	0.8814	0.7853	0.7372	0.7594	760

EPHA1	1.0136	0.7933	0.7410	0.7148	0.7877	766
ABL1	0.9129	1.0253	0.7918	0.6750	0.6805	777
DVL1	0.8749	0.8821	0.7796	0.7284	0.8108	779
INSR	0.9545	0.8315	0.7515	0.7114	0.8226	779
THAP11	0.9054	0.9304	0.7900	0.7198	0.7234	781
STAT6	0.9704	0.8215	0.7612	0.7310	0.7863	783
PKN2	0.9802	0.9808	0.7440	0.6256	0.7525	784
MAPK10	0.9277	1.1120	0.7709	0.6004	0.7101	786
TGFBR1	0.9024	0.8800	0.7744	0.7216	0.8072	790
CDK4	0.9154	1.0063	0.7906	0.6828	0.7043	791
HDAC7	0.9288	1.0658	0.7898	0.6518	0.6705	792
SETBP1	0.8835	0.8459	0.7775	0.7433	0.8428	793
LMO1	0.8982	0.8591	0.7862	0.7497	0.7883	796
DNMT3B	0.8656	0.9009	0.7822	0.7229	0.8413	811
DVL2	0.8595	0.8333	0.8029	0.7878	0.8091	811
ControlB5	1.0445	0.9179	0.7623	0.6846	0.7126	824
PCK1	0.9530	0.8026	0.7853	0.7766	0.7884	829
KDR	0.9429	0.9606	0.7932	0.7094	0.7159	833
HDAC2	0.9982	0.8514	0.7498	0.6991	0.8453	835
MST1R	0.9822	0.9264	0.7535	0.6671	0.8125	838
TGFBR2	0.9561	1.0429	0.7930	0.6681	0.6841	842
SLC25A1	0.9350	0.8427	0.7796	0.7480	0.8379	844
KLF4	0.9287	0.8785	0.7715	0.7180	0.8564	845
HK1	1.0966	0.8479	0.7591	0.7147	0.7421	847
CAD	0.8563	0.9286	0.7733	0.6956	0.9191	855
CDKN1B	0.8870	0.9154	0.7905	0.7280	0.8418	859
AKT1	1.0446	1.1167	0.7571	0.5772	0.6910	862
BTK	0.9458	0.9661	0.7998	0.7167	0.7276	871
TYRO3	0.9676	1.1038	0.8046	0.6550	0.6668	872
CDK12	1.0609	0.8807	0.7744	0.7213	0.7399	882
PRKCB	0.9068	0.9113	0.8046	0.7513	0.7897	884
SLC2A3	0.8905	0.9537	0.7839	0.6990	0.8709	888
EP300	0.9067	0.8293	0.8167	0.8103	0.8206	894
KRAS	0.9538	0.9813	0.7721	0.6676	0.8432	906
KMT2A	0.9102	0.9262	0.8127	0.7559	0.7930	915
TSHZ3	0.9797	0.9733	0.7730	0.6729	0.8350	919
PAK1	1.0031	1.0069	0.7899	0.6815	0.7477	920
RORA	0.9753	0.8359	0.7934	0.7722	0.8333	921

SMAD4	0.8593	0.9205	0.8039	0.7455	0.8945	924
CSF1R	0.9127	0.9174	0.8242	0.7776	0.7886	939
STAT1	1.0351	0.8187	0.7942	0.7820	0.7996	942
LRRK2	1.0073	0.9437	0.7519	0.6561	0.9024	945
SRC	0.9742	0.9884	0.7946	0.6977	0.7922	945
CRKL	0.9522	0.9980	0.8216	0.7334	0.7439	954
RICTOR	0.9190	0.9040	0.8100	0.7630	0.8539	957
PRKAG3	0.8990	0.9896	0.8289	0.7485	0.7922	965
MAP2K5	0.9767	0.9587	0.8135	0.7409	0.7537	968
ACVR1C	1.0549	1.1148	0.7737	0.6032	0.7707	973
SLC16A1	0.9161	0.9751	0.7924	0.7011	0.9057	974
SMAD9	0.9416	0.8788	0.8070	0.7710	0.8762	974
TBX3	0.9272	0.8877	0.8294	0.8002	0.8410	982
PGK2	0.8994	0.8977	0.8409	0.8125	0.8498	992
MAPK11	0.9250	0.8786	0.8355	0.8140	0.8569	1001
FLT3	0.9981	0.9315	0.8090	0.7477	0.8096	1008
HCK	0.9974	0.9399	0.7763	0.6945	0.9287	1016
MAPK12	0.9519	0.9404	0.8341	0.7810	0.8006	1020
IDH2	1.1414	0.9476	0.7948	0.7184	0.7520	1021
PFKFB3	1.0010	1.2065	0.8241	0.6329	0.7460	1023
SMAD7	0.9504	0.9486	0.8125	0.7444	0.8654	1023
PIK3CB	0.9490	0.9314	0.8222	0.7676	0.8507	1025
LTK	0.9347	0.8752	0.8406	0.8233	0.8679	1027
PRKAB2	0.9445	1.0714	0.7991	0.6629	0.8897	1029
RGN	0.9269	0.9202	0.8184	0.7675	0.9006	1032
CDKN2A	0.9511	0.9533	0.8067	0.7334	0.8881	1033
TIE1	1.0367	1.0162	0.7993	0.6909	0.8109	1036
ACVRL1	0.9772	0.9150	0.8266	0.7824	0.8305	1043
CDC37	0.9117	1.0159	0.7995	0.6912	0.9614	1043
RELB	0.9180	0.9986	0.8044	0.7073	0.9415	1043
RPTOR	1.2288	1.0624	0.7962	0.6631	0.7114	1043
PGK1	0.9582	0.9102	0.8154	0.7680	0.8837	1044
GATA2	0.9383	0.9499	0.8456	0.7934	0.8160	1045
FLT1	0.9394	0.9521	0.8080	0.7359	0.9108	1046
CBL	0.9074	0.9240	0.8253	0.7760	0.9238	1052
LCK	1.0427	0.9313	0.8082	0.7467	0.8215	1054
PIK3CG	0.9419	0.8788	0.8528	0.8399	0.8586	1054
NRAS	1.1328	1.0384	0.8146	0.7027	0.7143	1056

PCBP1	1.6158	0.9786	0.7309	0.6070	0.9075	1066
DHFR	1.2346	1.5396	0.8667	0.5302	0.6308	1072
PIK3R1	0.9494	1.0777	0.8396	0.7205	0.8274	1081
CARD11	0.9906	1.1906	0.8449	0.6720	0.7809	1083
SLC2A2	1.0223	1.0351	0.8258	0.7211	0.7851	1084
PAX8	0.9702	0.8950	0.8495	0.8268	0.8509	1088
PIK3CD	0.9669	0.9182	0.8531	0.8205	0.8461	1096
AR	0.9292	0.9803	0.8144	0.7315	0.9607	1097
IGF1R	1.0982	0.8639	0.8127	0.7871	0.8510	1102
PRKAA1	1.0219	0.9053	0.8103	0.7628	0.9048	1102
PRKAR1B	1.0650	0.8827	0.8221	0.7918	0.8523	1112
FOXL2	0.9375	0.9110	0.8582	0.8318	0.8981	1116
PRKCG	0.9991	1.1030	0.8607	0.7395	0.7527	1122
ROCK1	1.0127	0.8910	0.8396	0.8139	0.8739	1122
IKBKE	0.9176	0.9345	0.8561	0.8168	0.9250	1129
NFE2L3	0.9907	1.1115	0.8427	0.7083	0.8232	1129
LIFR	1.0014	1.0139	0.7948	0.6852	0.9941	1138
TYK2	0.9432	0.8943	0.8810	0.8743	0.8837	1143
PGAM2	1.0560	1.1163	0.8453	0.7097	0.7730	1150
PRKCH	0.9862	1.0161	0.8618	0.7847	0.8157	1152
FBP1	1.0621	1.1484	0.8541	0.7070	0.7607	1159
RHOA	1.0107	0.9370	0.8601	0.8216	0.8458	1160
ERBB4	0.9974	0.9744	0.8642	0.8091	0.8477	1174
ARAF	0.9544	0.9167	0.8760	0.8556	0.9010	1176
PRKCA	0.9940	0.9055	0.8719	0.8552	0.8812	1181
EIF4A2	0.9609	0.9113	0.8859	0.8732	0.8890	1190
PRKCE	1.0627	1.0387	0.8557	0.7641	0.7981	1197
SLC16A4	1.1944	0.9791	0.8337	0.7610	0.8455	1222
JAK1	1.0240	0.9592	0.8685	0.8231	0.8688	1225
SOX2	1.0014	0.9558	0.8622	0.8155	0.9072	1229
EGFR	1.0590	1.0352	0.8636	0.7778	0.8198	1232
HK2	0.9972	1.0561	0.8898	0.8066	0.8217	1232
HRAS	0.9998	0.9416	0.8852	0.8570	0.8796	1234
MTOR	0.9934	0.9803	0.8890	0.8433	0.8604	1234
FGR	1.0561	1.0559	0.8510	0.7485	0.8717	1244
PDGFRA	0.9973	1.0545	0.8579	0.7596	0.9189	1246
SMO	1.0763	1.0220	0.8756	0.8024	0.8226	1261
FYN	0.9847	1.0404	0.8630	0.7743	0.9338	1263

RALB	0.9585	1.0306	0.8829	0.8091	0.9302	1264
NOTCH3	1.0267	0.9948	0.8708	0.8088	0.9012	1265
EPHB4	0.9803	0.9480	0.8940	0.8670	0.9255	1280
EPHA7	0.9658	1.0102	0.8984	0.8425	0.9204	1288
SMAD2	1.0154	1.0162	0.8884	0.8245	0.8766	1288
YES1	1.0240	1.0315	0.8878	0.8160	0.8795	1294
PRKCD	1.0257	0.9621	0.8918	0.8566	0.9009	1301
RPL22	1.3393	1.0971	0.8546	0.7333	0.8340	1309
CDK5	1.0488	1.0972	0.8813	0.7733	0.8724	1310
PRKCZ	1.0171	0.9850	0.8839	0.8334	0.9423	1320
GPI	1.5461	1.5333	0.9447	0.6503	0.7606	1327
HIF1A	1.0087	1.0876	0.8766	0.7710	0.9579	1333
JAK3	1.0438	1.1562	0.8858	0.7506	0.8878	1334
ControlA4	1.0474	0.9815	0.8809	0.8306	0.9446	1341
GLI2	0.9826	0.9797	0.9158	0.8838	0.9564	1344
MOS	1.0409	1.1877	0.9052	0.7639	0.8761	1352
PTK2	1.2239	1.1125	0.8879	0.7756	0.8134	1359
STK11	1.0635	0.9650	0.8895	0.8517	0.9413	1359
AURKB	1.1085	1.0373	0.8474	0.7524	1.0167	1363
FRK	0.9916	1.0007	0.9332	0.8994	0.9241	1366
UQCR10	1.0347	1.0757	0.9209	0.8435	0.8713	1367
MAP2K2	1.0674	1.1969	0.9339	0.8024	0.8072	1371
AURKC	1.1097	0.9454	0.9125	0.8961	0.8987	1374
PCK2	1.0416	1.1138	0.9267	0.8332	0.8476	1375
JAK2	1.1286	1.3202	0.9184	0.7176	0.8620	1380
MECOM	1.0353	1.1294	0.9247	0.8224	0.8655	1381
H3F3C	1.0186	1.0346	0.9201	0.8629	0.9221	1385
STAT5A	0.9702	1.0032	0.9340	0.8994	0.9800	1386
POLQ	1.0580	1.0598	0.9265	0.8598	0.8658	1391
PKM	1.0292	1.1535	0.9261	0.8124	0.8797	1392
EPHB6	1.0293	1.0327	0.9104	0.8492	0.9491	1396
EPAS1	1.0202	1.0207	0.9182	0.8669	0.9633	1407
LDHC	1.1300	0.9943	0.9129	0.8721	0.9083	1417
NANOG	1.0408	1.1467	0.9126	0.7956	0.9448	1426
AXL	1.0735	1.1001	0.9175	0.8263	0.9045	1429
LYN	1.0290	1.0469	0.9282	0.8689	0.9389	1429
PRKAA2	1.1812	1.0120	0.9133	0.8640	0.8963	1432
NOTCH2	1.0944	1.0027	0.9001	0.8488	0.9953	1437

ControlB1	1.0856	1.0179	0.9378	0.8978	0.9043	1450
NSD1	1.0097	1.0419	0.9596	0.9184	0.9267	1457
SMAD6	1.2461	1.2791	0.9500	0.7855	0.7996	1458
U2AF1	1.2273	0.9664	0.9226	0.9007	0.9062	1460
STAT3	1.1635	1.1955	0.9350	0.8048	0.8589	1465
PTPN11	0.9972	1.0099	0.9723	0.9536	0.9919	1468
TET1	1.0687	1.1459	0.9188	0.8052	0.9603	1470
ControlB3	1.0425	1.0261	0.9562	0.9213	0.9403	1473
BMPRI1A	1.0474	1.1472	0.9354	0.8295	0.9317	1476
EPHA6	1.1463	1.3338	0.9652	0.7808	0.8509	1479
MDM4	1.1068	1.0980	0.9473	0.8719	0.8956	1486
GNA11	1.0830	0.9997	0.9505	0.9259	0.9426	1487
PDGFRB	1.0568	1.0744	0.9501	0.8880	0.9354	1493
CRIPAK	1.0669	1.0307	0.9338	0.8853	0.9959	1494
CDK11A	1.3532	1.0379	0.8909	0.8174	0.9873	1504
ACVR2B	1.2281	1.2501	0.9352	0.7778	0.8957	1515
ACVR1	1.1545	0.9862	0.9566	0.9418	0.9579	1529
DDR2	1.1098	1.0472	0.9488	0.8996	0.9430	1530
FBP2	1.0772	1.0324	0.9688	0.9369	0.9673	1542
SDHA	1.0868	1.1121	0.9797	0.9136	0.9170	1553
WT1	1.0759	1.1629	0.9441	0.8347	1.0108	1553
MAPK3	1.1075	1.1488	0.9479	0.8474	0.9820	1559
ERBB2	1.0931	1.1076	0.9573	0.8821	0.9860	1565
NFKB1	1.0689	1.0915	0.9715	0.9114	0.9920	1572
EPHB1	1.0891	1.1746	0.9398	0.8225	1.0815	1574
MED12	1.3827	1.2092	0.9533	0.8254	0.8942	1576
PRKAG1	1.0435	1.0589	0.9913	0.9575	1.0416	1577
STAT2	1.2638	1.0839	0.9318	0.8557	1.0386	1588
DVL3	1.1522	1.0852	0.9694	0.9115	0.9944	1608
ZNF217	1.0974	1.0818	0.9845	0.9359	1.0412	1615
ControlB4	1.1288	1.1159	0.9890	0.9256	0.9584	1618
RALA	1.1100	1.1377	0.9671	0.8818	1.0542	1623
PRKCQ	1.0755	1.0615	1.0161	0.9935	1.0599	1624
GNAQ	1.0915	1.1091	0.9875	0.9267	1.0408	1625
NFE2L2	1.2370	1.1415	0.9560	0.8633	0.9893	1625
FASN	1.1097	1.0614	1.0252	1.0070	1.0253	1633
BMPRI2	1.2742	1.0661	0.9735	0.9273	0.9717	1638
STAT5B	1.2235	1.2167	0.9994	0.8908	0.9162	1642

H3F3A	1.2611	1.1268	0.9592	0.8754	1.0039	1644
TET2	1.1930	1.3379	1.0183	0.8585	0.9323	1645
IDH1	1.2072	1.1801	0.9815	0.8823	0.9645	1648
AKT3	1.0954	1.0868	1.0283	0.9991	1.0538	1650
LDHA	1.1405	1.0976	0.9819	0.9240	1.0862	1650
RAC1	1.1481	1.2593	1.0143	0.8918	0.9524	1654
HDAC9	1.1892	1.0854	1.0090	0.9709	1.0106	1661
AJUBA	1.1139	1.1680	1.0270	0.9565	0.9774	1663
HIST1H2BD	1.2885	1.4534	1.0520	0.8514	0.9381	1686
PRKACB	1.1128	1.1066	1.0519	1.0245	1.0869	1698
EPHA5	1.2583	1.2278	0.9955	0.8793	1.0127	1701
MAPK13	1.1849	1.2042	0.9943	0.8893	1.1012	1705
TEK	1.1393	1.1502	1.0728	1.0340	1.0403	1714
TUBD1	1.1682	1.1920	1.0406	0.9650	1.0277	1716
ControlA5	1.1493	1.1984	1.0272	0.9416	1.0761	1719
PRKCI	1.1690	1.1268	1.0488	1.0098	1.1183	1732
ABL2	1.2143	1.3056	1.0330	0.8967	1.0595	1734
BCL2L2	1.1827	1.1780	1.0636	1.0064	1.0438	1738
AKT2	1.1451	1.2139	1.0378	0.9497	1.1660	1741
ARID5B	1.1795	1.1324	1.0833	1.0588	1.0719	1741
FGFR1	1.1665	1.1934	1.0839	1.0291	1.0432	1745
SNAI2	1.2060	1.3331	1.0844	0.9601	0.9874	1747
GLS	1.1580	1.2223	1.0745	1.0005	1.0599	1753
AURKA	1.2196	1.3450	1.0506	0.9035	1.0790	1757
FOXA1	1.1988	1.1156	1.1097	1.1067	1.1087	1766
TLR4	1.2469	1.3487	1.0556	0.9091	1.2257	1785
LDHB	1.2061	1.1700	1.1011	1.0667	1.1677	1787
MET	1.2869	1.2947	1.0979	0.9996	1.0340	1788
IDH3G	1.1704	1.2066	1.1236	1.0821	1.1339	1795
EZH2	1.3224	1.1724	1.1068	1.0740	1.1539	1812
CBFB	1.3555	1.2220	1.1029	1.0433	1.0744	1813
STAT4	1.3200	1.5156	1.1370	0.9477	1.0458	1814
ControlA1	1.3967	1.2078	1.0957	1.0396	1.0864	1815
CHEK2	1.2109	1.2865	1.1097	1.0214	1.2542	1816
ControlA2	1.2827	1.2392	1.1191	1.0591	1.1443	1829
RPS6KB1	1.2727	1.3612	1.1580	1.0564	1.0751	1832
PHGDH	1.4448	1.5448	1.1307	0.9237	1.1076	1835
HDAC1	1.3562	1.4272	1.1375	0.9927	1.2277	1848

PIK3CA	1.3510	1.2684	1.1824	1.1394	1.2390	1859
INTS4	1.5057	1.4263	1.1753	1.0498	1.2334	1873
MDM2	1.4431	1.4027	1.2035	1.1040	1.3415	1881
IKBKB	1.3913	1.4471	1.3319	1.2742	1.3469	1889
GNAS	1.4339	1.4189	1.3917	1.3781	1.3935	1895
CHUK	1.6354	1.4578	1.3355	1.2743	1.3265	1900
RELA	1.8244	1.5754	1.3098	1.1769	1.2322	1903
IDH3B	1.4742	1.4858	1.4290	1.4006	1.4731	1908
BRAF	1.7936	1.5190	1.3751	1.3031	1.4849	1913
CDKN1A	1.7462	1.4996	1.4923	1.4887	1.4973	1920
MAP2K1	2.3699	1.5887	1.4913	1.4426	1.5520	1931
MAPK14	2.0328	2.0607	1.6116	1.3871	1.7382	1931
MAPK1	2.1929	2.1586	1.8494	1.6947	1.7433	1939

**TRAIL
REP2**

Gene	DM_mean	DM_median	three_score	GARP_score	sb_score	cum_rank
XIAP	0.4052	0.1561	0.1242	0.1083	0.1477	5
SMC3	0.6453	0.3698	0.2320	0.1631	0.3261	12
CDK8	0.6258	0.6199	0.4310	0.3366	0.3619	18
BCL2L1	0.6396	0.6973	0.4537	0.3319	0.3675	26
TUBD1	0.7527	0.6556	0.4645	0.3689	0.4968	38
KAT6A	0.6830	0.7199	0.5477	0.4616	0.5244	56
BCL2A1	0.6902	0.6038	0.5506	0.5240	0.5367	58
CDK9	0.7769	0.5883	0.5281	0.4981	0.5398	58
IDH1	0.6639	0.6778	0.5631	0.5058	0.6029	71
CS	0.7965	0.7159	0.5837	0.5176	0.5418	85
HIF1A	0.7115	0.7434	0.6115	0.5455	0.5461	93
ZEB1	0.6688	0.6718	0.5784	0.5317	0.6645	96
KRAS	0.7689	0.8137	0.5829	0.4675	0.5429	100
PGK1	0.8751	0.7904	0.5449	0.4222	0.4853	100
INTS4	0.7226	0.6572	0.6095	0.5856	0.5941	101
BMPR1A	0.6660	0.7087	0.6012	0.5475	0.6790	110
NFKB2	0.7431	0.7834	0.6303	0.5537	0.5848	114
SDHA	0.7901	0.8414	0.5849	0.4567	0.6097	129
TBL1XR1	0.7882	0.7981	0.5702	0.4563	0.7017	130
PRKAR2A	0.8704	0.7297	0.6218	0.5679	0.5697	133
CDK2	0.8990	0.8469	0.5183	0.3540	0.5066	135

LYN	0.7823	0.8497	0.6139	0.4961	0.5526	138
SLC16A4	0.8476	0.7433	0.6381	0.5854	0.6205	147
FOXA1	0.7984	0.8146	0.6441	0.5588	0.6201	151
UQCR10	0.8956	0.6965	0.6322	0.6000	0.6442	167
CDK6	0.7676	0.7810	0.6641	0.6056	0.7317	187
MCL1	1.0125	0.7688	0.5715	0.4729	0.5213	191
ACVR1	0.8564	0.7849	0.6453	0.5755	0.7286	195
IDH3A	0.7993	0.7331	0.6923	0.6719	0.6869	200
RAF1	0.8610	0.7453	0.6730	0.6368	0.6955	201
TLR4	0.9930	0.8382	0.5923	0.4694	0.5045	201
PRKAA1	0.8325	0.8463	0.6941	0.6181	0.6339	209
RPL22	0.8220	0.7613	0.6848	0.6466	0.7299	213
PRKCI	0.8405	0.8143	0.6968	0.6381	0.6564	214
ControlA2	0.8064	0.8064	0.7048	0.6540	0.6839	216
VEZF1	0.8810	0.8259	0.6906	0.6230	0.6532	220
LCK	0.8579	0.8167	0.6797	0.6112	0.7171	225
DVL3	0.8448	0.8412	0.6943	0.6208	0.7085	233
RPL5	0.9457	0.8471	0.6489	0.5497	0.6249	237
USP9X	0.8372	0.7880	0.7100	0.6711	0.7173	239
SLC25A1	0.9700	0.8351	0.6360	0.5365	0.6799	243
PDK3	0.8062	0.8875	0.7227	0.6403	0.6556	250
CDK11A	0.8359	0.9216	0.6983	0.5867	0.6586	255
PPP2R1A	1.0273	0.9344	0.5309	0.3292	0.4409	265
MDM4	1.0034	0.7933	0.6760	0.6173	0.6219	266
HDAC8	0.8657	0.8447	0.7203	0.6580	0.7091	268
SLC2A2	0.8400	0.7834	0.7375	0.7145	0.7207	274
NFE2L2	0.8202	0.8390	0.7231	0.6651	0.7599	277
LDHB	0.8658	0.7586	0.7256	0.7090	0.7575	288
ENO1	0.9573	0.7762	0.7154	0.6851	0.6959	290
PIK3CA	0.9289	0.9865	0.6576	0.4932	0.5992	291
RHOA	0.8570	0.8656	0.7356	0.6706	0.7096	292
SRC	0.9091	0.7668	0.7454	0.7346	0.7407	333
PIK3CD	0.8800	1.0225	0.7297	0.5834	0.5906	337
SKP2	0.8538	0.7997	0.7485	0.7229	0.7987	338
MECOM	0.8863	1.0272	0.7171	0.5621	0.6047	344
CSF1R	0.9119	0.7810	0.7534	0.7396	0.7569	351
TEK	0.8969	0.8355	0.7644	0.7289	0.7456	354
TSHZ2	0.9021	0.8237	0.7429	0.7026	0.8031	356

RPTOR	1.0780	0.9769	0.6007	0.4125	0.5630	358
RAD21	0.8996	1.0314	0.7305	0.5801	0.5903	361
AKT3	0.9443	0.8407	0.7402	0.6899	0.8087	386
ABL2	0.8843	0.8858	0.7828	0.7314	0.7386	392
ControlB3	0.9143	0.8481	0.7713	0.7330	0.7662	394
MDM2	1.1724	0.7391	0.6389	0.5889	0.7165	400
CTNNB1	0.8895	0.8835	0.7557	0.6918	0.8253	403
PRKCH	0.9790	0.8078	0.7592	0.7349	0.7768	410
RALA	0.9820	0.9084	0.7731	0.7055	0.7213	423
PCK1	0.9728	0.9403	0.7605	0.6706	0.7381	428
CCND1	0.9668	0.9211	0.7454	0.6575	0.8074	431
PRKAB2	0.9378	0.9895	0.7533	0.6353	0.7774	431
G6PD	0.8420	0.9133	0.7854	0.7214	0.8139	433
SNAI2	0.8962	0.9805	0.7928	0.6990	0.7282	443
AJUBA	0.9399	0.8375	0.7815	0.7534	0.8055	448
CHEK2	0.9692	0.9406	0.7747	0.6917	0.7404	448
SLC2A3	1.0011	0.9363	0.7522	0.6602	0.7677	448
GNAQ	0.8572	0.8739	0.7889	0.7465	0.8341	456
ZNF217	0.9078	0.8856	0.7931	0.7469	0.7943	456
PRKAR1A	0.9227	1.0126	0.7789	0.6621	0.7636	468
RPS6KB1	0.9552	0.8640	0.7745	0.7297	0.8340	472
MAP2K5	0.9153	0.9170	0.7761	0.7056	0.8501	479
PRKACB	0.8825	0.9063	0.7890	0.7303	0.8488	479
CARD11	0.9088	1.0319	0.7346	0.5860	0.8285	480
HK1	0.9394	0.9046	0.7722	0.7060	0.8552	481
SOX17	0.9671	0.8649	0.7911	0.7542	0.7991	494
SPOP	0.8935	0.9307	0.8034	0.7397	0.8175	495
ACLY	0.8968	0.8990	0.8059	0.7593	0.8190	498
BMPR2	0.8999	0.8091	0.8065	0.8052	0.8068	508
BMPR1B	1.0530	0.8894	0.7793	0.7242	0.7774	512
HDAC9	0.9339	1.0563	0.8059	0.6807	0.7009	513
SLC2A1	1.0720	0.9904	0.7647	0.6519	0.7225	515
CDK5	0.9955	1.0683	0.7918	0.6535	0.6561	527
EPHA5	0.9630	1.0465	0.7777	0.6432	0.8061	544
CDK7	1.8314	0.8445	0.6677	0.5793	0.6770	546
HK2	1.1297	0.8710	0.7740	0.7255	0.7432	549
HSP90AA1	0.9208	0.9026	0.8295	0.7930	0.7965	557
PRKAR2B	1.0974	0.9300	0.7845	0.7117	0.7460	562

PGK2	0.9416	0.8489	0.8139	0.7965	0.8412	569
PARP10	0.9421	0.8590	0.8192	0.7992	0.8457	582
TKT	1.1117	1.1024	0.7549	0.5812	0.6262	587
CDKN2A	0.9444	0.8978	0.8169	0.7765	0.8649	591
PDGFRB	1.1110	0.9815	0.7815	0.6815	0.7465	591
STAT5B	0.9762	1.0195	0.7831	0.6649	0.8650	592
CDK4	0.9282	0.9444	0.8244	0.7645	0.8451	593
NSD1	0.9824	0.8428	0.8185	0.8063	0.8250	593
EIF4A2	1.0383	0.9952	0.8087	0.7154	0.7847	594
TGFBR1	0.9997	0.8994	0.8171	0.7760	0.8274	594
HIST1H2BD	0.9692	0.9765	0.8279	0.7536	0.8063	596
BRD4	0.9402	0.9299	0.8206	0.7659	0.8571	597
PTPN11	0.9370	1.0227	0.8446	0.7556	0.7615	609
MOS	1.0040	0.9325	0.8210	0.7652	0.8175	610
WT1	1.0774	0.8786	0.7982	0.7580	0.8374	621
NFKB1	1.0251	0.9111	0.8138	0.7651	0.8519	629
SF3B1	1.1678	0.9417	0.7792	0.6980	0.7923	636
GATA3	0.9089	1.0091	0.7934	0.6855	0.9488	640
KDR	1.0091	0.8516	0.8251	0.8118	0.8254	643
BLK	1.0630	0.9420	0.8276	0.7705	0.7726	644
SMC1A	1.1413	1.0130	0.7409	0.6048	0.8513	646
RPIA	1.1022	1.3305	0.7400	0.4447	0.6371	650
NANOG	0.9681	0.8609	0.8347	0.8216	0.8542	663
MAPK9	1.2027	0.8548	0.7813	0.7446	0.8238	668
H3F3C	1.2336	0.8645	0.7870	0.7483	0.7810	669
EPHA3	0.9391	0.9108	0.8534	0.8247	0.8266	670
CAD	0.9916	1.0371	0.8460	0.7504	0.8035	679
TYK2	0.9571	0.9728	0.8526	0.7925	0.8330	681
YAP1	1.9061	1.0016	0.7446	0.6162	0.6280	682
GAPDH	1.1877	0.8110	0.7964	0.7891	0.8070	684
TGFBR2	0.9155	0.9164	0.8448	0.8091	0.9016	693
E2F3	1.1015	1.1993	0.8205	0.6311	0.6491	701
PIK3R1	1.0025	0.9157	0.8457	0.8107	0.8492	702
RAC1	0.9448	0.9712	0.8289	0.7578	0.9351	702
STAT4	1.0855	0.9589	0.8412	0.7823	0.7938	705
ACVR2A	1.0330	0.9140	0.8437	0.8085	0.8379	707
EPHB1	1.0584	0.9306	0.8327	0.7838	0.8771	725
PRKACA	1.0048	0.9705	0.8321	0.7628	0.9180	726

EPHA1	1.2306	0.9809	0.8063	0.7190	0.7801	728
DNMT3B	1.1235	1.1076	0.8338	0.6970	0.7005	730
PIK3CB	1.0486	0.9723	0.8223	0.7472	0.9136	731
FGFR1	1.0634	0.9051	0.8284	0.7901	0.9047	742
EPHB6	0.9514	1.0035	0.8597	0.7878	0.8854	745
MET	0.9422	0.8784	0.8692	0.8645	0.8757	745
EPAS1	1.1320	0.9325	0.8205	0.7644	0.8601	747
ROCK1	0.9438	0.9448	0.8672	0.8284	0.8602	754
SMAD6	1.0474	1.1142	0.8646	0.7398	0.7556	759
RGN	1.0049	0.8991	0.8493	0.8244	0.8982	763
PRKCG	1.0048	1.0242	0.8423	0.7514	0.9071	766
ControlA3	1.4814	0.8915	0.7962	0.7485	0.8039	767
MAPK12	0.9421	0.9336	0.8557	0.8168	0.9196	769
POU5F1	1.0442	0.9358	0.8408	0.7933	0.9131	774
FRK	1.1697	0.9739	0.8456	0.7815	0.7823	783
RALB	1.0613	1.1709	0.8645	0.7113	0.7891	792
NCOA3	0.9965	0.9907	0.8402	0.7649	0.9688	794
STAT5A	1.0137	1.0761	0.8664	0.7615	0.8589	807
FLT1	1.0453	0.9236	0.8697	0.8427	0.8655	810
RORA	0.9877	0.9855	0.8631	0.8019	0.9223	810
NOTCH3	1.1103	1.0791	0.8504	0.7361	0.8113	811
AKT2	1.0762	1.0152	0.8499	0.7672	0.8801	812
NRAS	0.9956	1.0186	0.8757	0.8042	0.8693	814
HDAC6	1.1498	0.9383	0.8380	0.7879	0.8683	816
GPI	1.2671	1.1034	0.8339	0.6992	0.7011	820
HDAC4	1.1219	1.0088	0.8524	0.7741	0.8412	820
GLI3	1.1313	1.0209	0.8604	0.7802	0.8108	828
ControlB1	1.0175	1.1040	0.8650	0.7455	0.9059	851
ACVR1B	1.1262	1.0148	0.8646	0.7895	0.8377	856
ControlA1	1.0005	0.9983	0.9000	0.8508	0.8534	861
SLC16A7	1.0679	0.9485	0.8826	0.8496	0.8546	866
FYN	0.9603	0.9918	0.8820	0.8271	0.9241	868
PTCH1	1.0237	1.0253	0.8619	0.7802	0.9425	871
HDAC11	1.2027	1.2127	0.8612	0.6854	0.7404	885
SOX2	1.0895	0.9310	0.8818	0.8573	0.8674	885
TET1	0.9775	0.9776	0.8736	0.8216	0.9685	885
HDAC5	1.0838	0.9320	0.8818	0.8567	0.8860	896
LDHC	1.2155	0.9241	0.8418	0.8006	0.9035	896

LIFR	1.1966	0.9227	0.8501	0.8138	0.8775	898
SLC16A3	1.1597	1.0866	0.8817	0.7792	0.7893	911
IGF1R	1.1110	1.0698	0.8497	0.7396	0.9306	912
EPHA7	1.0603	0.9590	0.8781	0.8376	0.9353	922
TALDO1	1.0166	1.0657	0.8967	0.8123	0.8792	922
DVL1	1.0957	1.1134	0.8942	0.7847	0.8231	926
ESR2	1.0856	1.1465	0.9071	0.7875	0.7912	927
GNA11	0.9917	1.0923	0.8923	0.7924	0.9269	929
PRKCZ	1.0052	0.9531	0.9047	0.8805	0.9234	936
PRKAA2	1.0934	1.1497	0.8845	0.7519	0.8707	944
PRKAB1	1.2332	0.8751	0.8671	0.8631	0.8723	947
FLT3	1.0454	1.0307	0.8732	0.7944	0.9819	952
LDHA	1.0471	1.0653	0.9015	0.8196	0.8778	957
ControlA5	1.0042	0.9381	0.9151	0.9035	0.9235	959
FBP1	1.0179	1.0042	0.8879	0.8298	0.9684	960
ACVR1C	1.0826	0.9929	0.8723	0.8120	0.9689	961
ACVRL1	1.0228	1.1429	0.9043	0.7850	0.9125	969
KMT2A	1.2200	1.0211	0.8735	0.7997	0.8731	980
U2AF1	1.0895	0.9784	0.9063	0.8703	0.8939	981
NOTCH4	1.1239	0.9527	0.8973	0.8697	0.8894	987
GLI2	0.9929	1.0688	0.9158	0.8392	0.9198	993
ERBB4	1.3033	1.0560	0.8647	0.7691	0.8589	995
PRKCE	1.1083	1.2179	0.9158	0.7647	0.8124	996
ARID5B	1.0522	1.1135	0.9106	0.8092	0.8847	1000
MAPK13	1.0416	1.0195	0.9257	0.8788	0.8888	1000
HDAC3	1.0954	1.0247	0.8826	0.8115	0.9453	1005
POLQ	1.1481	1.0298	0.8764	0.7998	0.9306	1010
GLI1	1.0420	1.0252	0.8945	0.8292	0.9719	1013
GATA2	1.0049	1.0514	0.9014	0.8264	0.9711	1014
MED12	1.1004	1.0663	0.8884	0.7994	0.9413	1014
PRKAG2	1.0647	1.0415	0.8916	0.8167	0.9613	1016
MYD88	1.0821	1.1373	0.9123	0.7997	0.9006	1027
MYCL	1.2305	1.2267	0.8968	0.7318	0.8181	1029
HCK	1.1207	1.1348	0.9189	0.8109	0.8219	1031
PGD	1.6593	1.2022	0.8820	0.7220	0.7564	1032
FOXL2	1.0584	1.2081	0.9412	0.8078	0.8350	1041
EGFR	1.0145	1.0154	0.9302	0.8876	0.9412	1044
RELB	1.1108	1.0947	0.8739	0.7635	1.0271	1049

IDH2	1.0464	1.0196	0.9342	0.8916	0.9164	1052
PKM	1.1064	1.1030	0.9074	0.8096	0.9140	1061
SMAD1	1.0637	1.0231	0.9066	0.8483	0.9850	1063
CCNE1	1.0826	1.0976	0.9137	0.8218	0.9160	1064
CBFB	1.1925	0.9912	0.9141	0.8756	0.8767	1065
EPHB2	1.2186	1.1362	0.8920	0.7699	0.8889	1066
TET2	1.0827	1.0793	0.8962	0.8046	0.9887	1067
PRKCQ	1.0575	1.0107	0.9244	0.8812	0.9638	1070
HRAS	1.0233	1.0202	0.9191	0.8685	0.9951	1071
PRKAG3	1.1582	1.2823	0.9254	0.7469	0.8491	1076
CBL	1.1421	1.1281	0.8781	0.7531	1.0199	1078
AURKB	1.1653	1.0474	0.9179	0.8531	0.8646	1079
TAF1	1.2904	1.2471	0.8376	0.6328	0.9713	1084
PAF1	1.1169	1.3062	0.9005	0.6977	0.9647	1087
PGAM1	1.2212	1.0183	0.9090	0.8544	0.8780	1088
SMAD7	1.0412	1.0285	0.9484	0.9084	0.9176	1088
PDGFRA	1.0907	1.0871	0.9360	0.8605	0.8820	1093
CTCF	1.1351	0.9713	0.9136	0.8847	0.9597	1094
PCK2	1.0547	0.9985	0.9395	0.9099	0.9606	1095
ELF3	1.2025	1.0154	0.8821	0.8154	0.9849	1106
IKBKE	1.2627	1.0354	0.8803	0.8027	0.9459	1106
EP300	1.0884	1.1437	0.9072	0.7889	1.0039	1113
JAK3	1.1765	1.0889	0.9063	0.8150	0.9149	1115
STAT3	1.0608	1.2074	0.9243	0.7828	0.9901	1126
THAP11	1.0750	1.1114	0.9301	0.8395	0.9423	1126
H3F3A	1.0858	1.0056	0.9387	0.9052	0.9617	1129
FBP2	1.0284	1.1173	0.9465	0.8612	0.9457	1132
RET	1.0483	1.1070	0.9634	0.8916	0.9017	1132
MAP3K8	1.0841	1.1550	0.9520	0.8505	0.8879	1136
BTK	1.1945	1.0614	0.9180	0.8463	0.9116	1140
JAK2	1.3572	1.0000	0.8980	0.8470	0.9232	1142
NOTCH2	1.5019	1.0237	0.8964	0.8328	0.8810	1142
TSHZ3	1.1439	0.9689	0.9380	0.9225	0.9461	1142
MTOR	1.5189	0.9620	0.8984	0.8666	0.9098	1143
PRKACG	1.1317	1.1493	0.9268	0.8155	0.9077	1143
MAPK11	1.1899	1.0406	0.9286	0.8726	0.8964	1150
NOTCH1	1.0929	1.0677	0.9431	0.8808	0.9579	1169
KIT	1.2023	1.1322	0.9244	0.8205	0.9055	1180

PRKCA	1.1973	1.0714	0.9218	0.8469	0.9295	1182
REL	1.0337	1.0520	0.9760	0.9380	0.9871	1189
SMAD3	1.0361	1.0228	0.9743	0.9501	1.0153	1189
CRIPAK	1.1231	1.1048	0.9591	0.8862	0.9041	1190
MAPK10	1.1433	1.1886	0.9055	0.7640	1.1063	1192
FGR	1.1785	1.0524	0.9386	0.8817	0.9286	1199
HSP90AB1	1.1187	1.1977	0.9178	0.7778	1.1009	1206
GNAS	1.1781	1.0037	0.9274	0.8893	1.0025	1208
CDC37	1.5127	1.5928	0.9534	0.6338	0.8770	1212
ACVR2B	1.1513	1.1391	0.9445	0.8471	0.9381	1222
PRKCD	1.1505	1.0717	0.9692	0.9180	0.9240	1239
MAPK7	1.1089	1.3599	0.9188	0.6982	1.3096	1241
MST1R	1.0932	1.0261	0.9770	0.9524	0.9954	1242
ControlB2	1.2505	0.9790	0.9615	0.9527	0.9569	1262
MUSK	1.1478	1.0608	0.9478	0.8913	1.0246	1269
BCL2L2	1.0754	1.0697	0.9793	0.9341	1.0675	1275
MAPK8	1.1655	1.3240	0.9753	0.8009	0.9322	1276
EPHA6	1.0710	1.1036	0.9795	0.9174	1.0310	1277
ControlB4	1.1687	1.1468	0.9612	0.8684	0.9548	1283
FOXA2	1.0914	1.0464	0.9861	0.9559	1.0388	1289
CDKN1B	1.2327	1.2130	0.9151	0.7661	1.1178	1292
SMAD2	1.0741	1.0851	1.0119	0.9753	0.9995	1305
FGFR3	1.1504	1.1100	0.9724	0.9036	0.9820	1306
YES1	1.2953	1.0108	0.9658	0.9433	0.9682	1310
SETBP1	1.1085	1.0812	0.9979	0.9562	0.9926	1312
STK11	1.1562	1.1862	0.9416	0.8194	1.0810	1312
LRRK2	1.0797	1.0841	1.0067	0.9680	1.0214	1313
BDH1	1.1187	1.2530	0.9533	0.8035	1.1355	1323
KLF4	1.3119	1.1459	0.9482	0.8493	0.9548	1329
PRKAG1	1.1402	1.0775	0.9880	0.9433	1.0115	1332
TYRO3	1.1811	1.1697	0.9825	0.8889	0.9541	1337
GLS	1.1813	1.1792	0.9818	0.8830	0.9567	1340
PKN2	1.0926	1.0754	1.0160	0.9863	1.0442	1346
CDK1	1.2262	1.3384	0.9801	0.8010	0.9698	1356
SMO	1.2685	1.0339	0.9592	0.9218	1.0272	1357
HDAC2	1.1190	1.0773	1.0183	0.9889	1.0199	1364
EPHA8	1.1193	1.2973	0.9776	0.8178	1.1131	1368
PGAM2	1.1334	1.0684	1.0253	1.0037	1.0086	1370

ERBB3	1.1729	1.0574	1.0140	0.9923	0.9977	1374
ENO3	1.2280	1.2031	0.9401	0.8086	1.1527	1377
DDR2	1.2728	1.1461	0.9579	0.8638	1.0231	1383
PCBP1	1.6548	1.4999	0.9758	0.7138	1.0382	1403
EPHA10	1.1634	1.1411	0.9970	0.9250	1.0663	1404
ControlA4	1.2360	1.1110	0.9995	0.9438	0.9800	1406
LMO1	1.1509	1.1689	0.9905	0.9014	1.0948	1407
HDAC10	1.1549	1.1299	1.0300	0.9800	0.9958	1415
SRSF2	1.6578	1.1828	0.9207	0.7897	1.1775	1418
LTK	1.1152	1.2100	0.9846	0.8718	1.1879	1419
SIN3A	1.1081	1.1626	1.0321	0.9668	1.0706	1420
DNMT1	1.5314	1.3178	0.9828	0.8153	0.9409	1425
AURKC	1.2202	1.1246	0.9875	0.9190	1.0759	1428
ABL1	1.2479	1.0416	1.0107	0.9953	1.0326	1430
SYK	1.1809	1.2276	0.9975	0.8825	1.0556	1437
PRKAR1B	1.1945	1.3743	0.9870	0.7933	1.2515	1455
NFE2L3	1.1455	1.1600	1.0167	0.9451	1.1498	1462
PDK1	1.1971	1.1722	1.0374	0.9700	0.9885	1462
ARAF	1.1782	1.0771	1.0612	1.0532	1.0677	1464
SMAD9	1.2090	1.3498	0.9841	0.8012	1.2487	1466
NEDD9	1.2055	1.1150	1.0154	0.9657	1.1001	1469
AURKA	1.2563	1.2012	0.9742	0.8608	1.1721	1471
ControlB5	1.1616	1.2483	1.0068	0.8860	1.1371	1472
SLC16A1	1.2698	1.3659	1.0507	0.8932	0.9241	1481
EGR3	1.4218	1.2626	1.0186	0.8966	0.9340	1484
EPHA4	1.1961	1.1598	1.0293	0.9640	1.0949	1487
CDK12	1.1552	1.2223	1.0614	0.9809	1.0027	1488
IDH3G	1.1935	1.1993	1.0214	0.9325	1.1026	1488
BCL2	1.2908	1.4927	1.0931	0.8934	0.9090	1494
INSR	1.2785	1.3593	1.0240	0.8564	1.0151	1503
PTK2	1.2685	1.1664	1.0293	0.9607	1.0547	1516
AR	1.2752	1.2209	1.0364	0.9441	0.9946	1520
PIK3CG	1.3203	1.3302	1.0429	0.8992	0.9687	1528
ERBB2	1.3948	1.1554	1.0289	0.9656	1.0231	1537
HDAC7	1.2443	1.1723	1.0384	0.9714	1.0999	1543
PKN3	1.3996	1.2944	1.0074	0.8638	1.1255	1557
ESR1	1.2239	1.2589	1.0177	0.8971	1.2415	1561
ESRRB	1.3535	1.3133	1.0511	0.9200	1.0102	1573

MAP2K4	1.2420	1.2133	1.0860	1.0224	1.0785	1583
PRKCB	1.2923	1.2393	1.0599	0.9701	1.0819	1599
EPHB4	1.3043	1.3140	1.0782	0.9603	1.0305	1601
FH	1.2619	1.2431	1.0338	0.9292	1.2402	1602
SMAD4	1.2763	1.1842	1.0904	1.0435	1.1011	1602
MPL	1.2454	1.3008	1.1122	1.0179	1.0659	1615
FGFR4	1.3377	1.1521	1.0964	1.0685	1.1094	1617
FGFR2	1.2655	1.2681	1.0678	0.9677	1.1685	1632
AXL	1.1979	1.2169	1.1319	1.0894	1.1519	1633
TSHR	1.2269	1.3645	1.0837	0.9433	1.1850	1633
PKN1	1.2546	1.2489	1.0977	1.0221	1.1487	1639
PRX	1.4339	1.1916	1.0810	1.0257	1.1283	1640
SNAI1	1.2349	1.2276	1.1340	1.0872	1.1168	1643
MYCN	1.4351	1.1695	1.1114	1.0823	1.1083	1646
MAP3K1	1.4868	1.8180	1.2070	0.9016	0.9730	1647
TWIST1	1.2692	1.2748	1.1128	1.0318	1.1332	1659
STAT6	1.3410	1.2157	1.1090	1.0557	1.1301	1661
PAK1	1.2773	1.2302	1.1140	1.0559	1.1402	1663
PFKFB3	1.3094	1.1747	1.1243	1.0992	1.1670	1666
RICTOR	1.3504	1.2044	1.1196	1.0773	1.1628	1679
DDR1	1.2431	1.3411	1.1328	1.0286	1.1674	1684
PAX8	1.2917	1.2280	1.1501	1.1112	1.1277	1686
MAP2K2	1.3677	1.2076	1.1257	1.0848	1.1593	1689
CDK3	1.3049	1.1987	1.1661	1.1498	1.1552	1692
CDC42	1.3333	1.4072	1.1286	0.9893	1.1185	1696
CDKN2C	1.5318	1.2857	1.1148	1.0294	1.0950	1697
DVL2	1.3442	1.3793	1.1457	1.0290	1.0823	1700
CRKL	1.3861	1.4678	1.0967	0.9111	1.2657	1701
DHFR	2.5435	1.2866	1.0554	0.9399	1.1983	1706
NKX2-1	1.2775	1.3676	1.1679	1.0680	1.1393	1721
HIST1H1C	1.4463	1.2139	1.1554	1.1262	1.1503	1722
BRAF	1.8606	1.5944	1.1783	0.9703	1.0209	1724
STAT1	1.3708	1.2324	1.1347	1.0859	1.1768	1724
HDAC1	1.3226	1.2632	1.1613	1.1103	1.1651	1726
DNMT3A	1.5693	1.7740	1.2523	0.9914	1.0773	1755
JAK1	1.3595	1.3626	1.1361	1.0229	1.3526	1755
TERT	1.3587	1.3180	1.1734	1.1011	1.1742	1759
TIE1	1.3363	1.2953	1.2168	1.1775	1.2642	1775

MAPK3	1.8780	1.3630	1.1606	1.0594	1.1303	1776
B4GALT3	1.4362	1.3849	1.1576	1.0439	1.2477	1777
TBX3	1.3766	1.4682	1.1814	1.0381	1.2849	1786
ALK	1.4390	1.2997	1.2177	1.1766	1.2115	1789
CREBBP	1.5745	1.3917	1.1984	1.1018	1.1724	1807
IKBKB	1.6074	1.7558	1.2630	1.0166	1.1725	1809
EPHB3	1.5253	1.5969	1.2576	1.0879	1.1674	1812
AKT1	1.4627	1.4052	1.2132	1.1172	1.3862	1822
EPHA2	1.4470	1.5700	1.2840	1.1411	1.2158	1828
MAPK8IP1	1.5310	1.5345	1.2784	1.1504	1.1872	1832
ERCC2	1.6057	1.7534	1.2634	1.0184	1.4461	1835
FASN	1.4709	1.4327	1.3255	1.2719	1.3659	1842
ADSS	1.5722	1.6964	1.3189	1.1302	1.3756	1862
STAT2	1.5326	1.6190	1.3997	1.2900	1.6001	1876
HIST1H3B	1.8516	1.5480	1.4361	1.3802	1.4406	1884
CDKN1A	1.7364	1.6400	1.4452	1.3479	1.4504	1888
MAPK14	1.7545	1.7065	1.4733	1.3567	1.4109	1891
CHUK	1.7075	1.6942	1.5172	1.4287	1.5271	1895
MYC	1.7025	1.8435	1.4049	1.1856	1.6245	1895
IDH3B	1.8055	1.6279	1.5833	1.5610	1.5765	1902
MAP2K1	1.8628	1.9482	1.6460	1.4949	1.5087	1912
EZH2	2.0610	1.9633	1.6692	1.5222	1.5712	1920
PHGDH	2.1017	2.0441	1.7398	1.5877	2.0341	1931
MAPK1	2.3962	2.2709	1.9550	1.7971	1.8369	1934
RELA	2.3049	2.3294	2.0538	1.9160	1.9630	1937

Table

**DRA
REP1**

Gene	DM_mean	DM_median	three_score	GARP_score	sb_score	cum_rank
XIAP	0.2515	0.1954	0.1645	0.1491	0.1610	5
NFKB2	0.4675	0.4940	0.4057	0.3615	0.3924	21
SMC1A	0.6110	0.6314	0.3453	0.2022	0.2960	22
RAD21	0.5846	0.5660	0.4155	0.3403	0.4653	24
CDK6	0.6057	0.5691	0.4650	0.4129	0.4932	36
ERCC2	0.6157	0.5956	0.4462	0.3714	0.5087	40

HDAC8	0.5981	0.6597	0.5081	0.4323	0.6001	63
PGD	0.6978	0.5884	0.5082	0.4681	0.5524	65
MCL1	0.6329	0.7000	0.5178	0.4268	0.5334	68
SRSF2	0.6639	0.7697	0.4882	0.3475	0.4070	71
PCBP1	0.7826	0.7670	0.4749	0.3289	0.3848	82
SMC3	0.8356	0.6001	0.4787	0.4180	0.4849	94
YAP1	0.7673	0.7678	0.5509	0.4424	0.4909	104
SPOP	0.6333	0.6082	0.5904	0.5816	0.6001	105
MAPK8	0.7246	0.7152	0.5580	0.4793	0.6234	109
SRC	0.7109	0.7440	0.5959	0.5219	0.5776	118
RPL22	0.6552	0.8500	0.5080	0.3370	0.3593	122
TALDO1	0.6759	0.6245	0.6072	0.5985	0.6076	124
SLC25A1	0.8037	0.6950	0.5758	0.5162	0.6341	136
CCNE1	0.7232	0.7724	0.6021	0.5170	0.6346	145
TBL1XR1	0.7006	0.7719	0.6022	0.5173	0.6357	145
BCL2L1	0.6805	0.6605	0.6213	0.6017	0.6518	151
SKP2	0.6817	0.8769	0.5087	0.3246	0.3634	152
MDM4	0.8156	0.6724	0.5842	0.5401	0.6491	156
TAF1	0.8698	0.7006	0.5698	0.5045	0.5313	156
SLC2A1	0.8811	0.6629	0.5245	0.4553	0.6033	157
TSHZ2	0.6952	0.6949	0.6220	0.5856	0.6764	161
FLT3	0.8573	0.7444	0.5645	0.4746	0.6049	163
CTCF	0.7847	0.7206	0.5965	0.5345	0.6914	167
INSR	0.7353	0.7566	0.6558	0.6055	0.6135	173
FOXA2	0.7621	0.6816	0.6469	0.6296	0.6452	181
CS	0.9097	0.6705	0.5811	0.5363	0.5659	192
GLI1	0.7915	0.7046	0.6556	0.6312	0.6452	203
HSP90AB1	0.8206	0.7371	0.6690	0.6349	0.6686	231
NKX2-1	0.7461	0.7368	0.6742	0.6430	0.7184	238
NCOA3	0.8807	0.7415	0.6528	0.6084	0.6323	239
ALK	0.8459	0.8447	0.6406	0.5385	0.5576	240
USP9X	0.7864	0.8450	0.6629	0.5719	0.6297	242
BCL2A1	0.7671	0.7759	0.6881	0.6441	0.6505	245
SETBP1	0.7546	0.7610	0.6868	0.6497	0.6945	250
PRX	0.8308	0.7499	0.6758	0.6388	0.6686	255
PAF1	0.9192	0.7302	0.6153	0.5578	0.6749	257
CDK7	0.8429	0.7674	0.6261	0.5555	0.7413	258
CBL	0.7859	0.8505	0.6784	0.5924	0.6296	261

FGFR2	0.7820	0.8058	0.6868	0.6273	0.6957	262
RELB	0.8652	0.8382	0.6123	0.4994	0.6940	263
ENO3	0.8370	0.9057	0.6287	0.4903	0.4999	268
ESR1	0.7653	0.8182	0.6192	0.5197	0.7843	270
TKT	0.8950	0.7729	0.6709	0.6199	0.6202	274
EPHB1	0.7999	0.8284	0.6831	0.6104	0.6952	275
FH	0.7569	0.7964	0.7023	0.6553	0.7328	301
ESRRB	0.8307	0.7781	0.7011	0.6626	0.6924	303
SLC2A3	0.7933	0.9105	0.6715	0.5521	0.6485	306
CDK1	0.8173	0.8119	0.6900	0.6291	0.7367	309
CDC37	0.7698	0.7824	0.7119	0.6767	0.7037	313
NOTCH4	0.8172	0.8996	0.6551	0.5328	0.7023	315
PRKAB1	0.8382	0.8145	0.6760	0.6067	0.7608	323
MAPK9	0.8258	0.9643	0.6551	0.5005	0.5642	325
HDAC2	0.8311	0.8483	0.6563	0.5603	0.7653	331
KAT6A	0.7744	0.8345	0.6708	0.5890	0.8153	348
NFE2L3	0.8992	0.7623	0.7028	0.6731	0.6781	353
RAF1	0.8152	0.8291	0.7291	0.6791	0.7334	379
BDH1	0.8298	0.8491	0.7271	0.6661	0.7270	384
SOX17	0.8428	0.8019	0.7120	0.6670	0.7865	397
CDK8	0.8201	0.8596	0.7327	0.6692	0.7201	400
PKN2	0.8999	0.8521	0.7179	0.6508	0.6555	403
MAP2K4	0.8227	0.8224	0.6980	0.6358	0.8191	406
POU5F1	0.8518	0.8628	0.7317	0.6661	0.7015	412
PRKAA1	0.8064	0.8187	0.7528	0.7198	0.7337	418
SLC16A3	0.8329	0.9070	0.7385	0.6542	0.6671	418
MAPK11	0.8308	0.8154	0.7571	0.7279	0.7286	441
PRKAG3	0.8731	0.8500	0.7128	0.6442	0.7869	450
EPHA3	0.8332	0.7909	0.7513	0.7315	0.7655	453
MPL	0.9195	0.7728	0.7342	0.7149	0.7392	456
HDAC6	0.8443	0.8353	0.7281	0.6745	0.8063	464
SF3B1	0.9508	0.8403	0.7273	0.6708	0.7145	473
FRK	0.8462	0.7942	0.7531	0.7326	0.7711	477
NRAS	1.0193	0.8160	0.6963	0.6365	0.6692	478
RPIA	1.0787	0.7963	0.6785	0.6196	0.6410	484
ACVR2A	0.9771	0.8142	0.6778	0.6097	0.8009	486
PTK2	0.9650	0.8706	0.7146	0.6366	0.7042	490
PAX8	0.8721	0.8082	0.7529	0.7253	0.7901	498

HSP90AA1	0.8601	0.8243	0.7445	0.7047	0.8129	504
CDK2	0.9593	0.8304	0.6860	0.6138	0.8167	506
FGFR3	0.8985	0.9899	0.7376	0.6114	0.6378	507
ACLY	0.8571	0.9171	0.7632	0.6863	0.7061	509
BMPR1A	0.8433	0.8821	0.7194	0.6380	0.8376	509
SLC16A4	0.9194	0.8449	0.7471	0.6982	0.7609	509
LMO1	0.8254	0.8081	0.7696	0.7503	0.7967	511
BLK	0.8866	0.8860	0.7640	0.7029	0.7139	517
PGAM1	0.8913	0.9248	0.7407	0.6487	0.7600	518
AURKB	1.0372	0.8383	0.6886	0.6137	0.7306	524
G6PD	0.9384	0.8140	0.7281	0.6852	0.8111	528
KRAS	0.8735	0.8797	0.7286	0.6530	0.8168	528
CDK5	0.9521	0.8388	0.7546	0.7125	0.7188	530
PRKAA2	1.0126	0.8143	0.7203	0.6733	0.7365	543
KDR	0.9248	0.8989	0.7487	0.6736	0.7483	551
MTOR	0.8632	0.8110	0.7777	0.7610	0.7938	554
RGN	0.8959	0.9109	0.7592	0.6833	0.7547	555
PRKACG	0.9492	0.8932	0.7379	0.6603	0.7656	558
PRKAR2A	0.8761	0.8786	0.7603	0.7012	0.7942	562
PRKAR2B	0.8959	0.8897	0.7734	0.7153	0.7399	562
STK11	0.8445	0.8763	0.7787	0.7299	0.7747	563
PPP2R1A	0.9129	0.8912	0.7457	0.6729	0.7982	568
DHFR	0.9582	1.1342	0.6902	0.4681	0.5809	582
ControlA3	0.8748	1.0353	0.7038	0.5381	0.8043	591
TGFBR2	0.8583	0.8411	0.7966	0.7743	0.7780	592
MAP3K8	0.9257	0.8897	0.7554	0.6883	0.7871	593
TGFBR1	0.8453	0.8145	0.7973	0.7887	0.8040	605
CDC42	0.8246	0.8442	0.7927	0.7669	0.8249	609
HIST1H1C	1.0303	0.8728	0.7358	0.6673	0.7327	613
GLI3	0.8607	0.8515	0.7853	0.7522	0.8084	614
ControlA5	0.9220	0.9929	0.7785	0.6713	0.6808	617
PRKAR1B	0.9534	0.8450	0.7552	0.7103	0.8088	620
ControlB4	0.9521	1.1187	0.7483	0.5631	0.5894	621
SNAI1	0.8303	0.8772	0.7718	0.7191	0.8734	625
NSD1	0.9775	0.8934	0.7052	0.6111	0.8440	629
YES1	0.9311	0.8377	0.7837	0.7568	0.7971	632
CDK12	0.9299	0.9368	0.7570	0.6671	0.8076	641
CDK11A	1.5433	0.8436	0.6768	0.5934	0.7333	643

CARD11	0.9123	0.9002	0.7967	0.7450	0.7635	645
SMAD1	1.0075	0.8693	0.7601	0.7054	0.7460	647
SYK	0.8725	0.9350	0.7760	0.6965	0.8312	649
GATA3	0.8940	0.8316	0.8013	0.7862	0.8068	652
MAPK7	0.8655	0.9586	0.7118	0.5884	0.9239	652
U2AF1	0.9638	0.8512	0.7778	0.7412	0.7837	660
PRKACA	0.9362	0.9168	0.7467	0.6616	0.8639	661
PKN1	0.8989	0.8075	0.8051	0.8039	0.8074	665
ELF3	0.9833	0.8363	0.7604	0.7224	0.8181	670
E2F3	1.0392	0.9582	0.7510	0.6474	0.6988	675
SMAD2	0.9575	0.9269	0.7764	0.7012	0.7962	685
IDH1	0.9158	0.9328	0.7989	0.7320	0.7790	687
FLT1	0.9396	0.8848	0.8002	0.7579	0.7758	689
KIT	0.8953	0.8496	0.8108	0.7913	0.7973	690
POLQ	0.8856	0.9316	0.8143	0.7556	0.7690	696
PIK3CB	0.8589	0.8611	0.8007	0.7704	0.8526	697
ENO1	0.9689	0.9299	0.7962	0.7293	0.7398	705
HDAC4	0.8726	0.8421	0.8177	0.8056	0.8262	717
HDAC10	0.9987	0.8571	0.7923	0.7599	0.7714	718
PARP10	0.9217	0.9849	0.7823	0.6810	0.8311	733
PRKAB2	0.9046	0.9110	0.8002	0.7449	0.8403	733
EP300	0.9284	0.8828	0.7932	0.7485	0.8541	736
EIF4A2	0.9497	0.9722	0.8090	0.7275	0.7539	741
STAT6	1.0058	0.8582	0.7904	0.7565	0.7951	744
SMAD4	0.8826	0.8576	0.8223	0.8047	0.8292	746
PCK2	1.0160	0.9072	0.7953	0.7393	0.7579	755
ROCK1	1.0008	0.9520	0.7878	0.7057	0.7802	758
HDAC5	0.9186	0.8802	0.8097	0.7744	0.8497	761
HCK	0.9418	0.8372	0.8148	0.8036	0.8335	765
DVL2	0.9036	0.8676	0.8275	0.8074	0.8081	767
INTS4	1.0427	0.9228	0.7924	0.7272	0.7479	770
IKBKE	0.9746	1.0889	0.8062	0.6649	0.7199	781
RPL5	0.8998	0.9719	0.7974	0.7102	0.8868	791
SMAD3	0.9781	0.8427	0.8058	0.7873	0.8411	797
IDH2	0.9777	1.0432	0.7974	0.6745	0.7682	800
CAD	1.0653	0.8375	0.7999	0.7812	0.7972	815
CDKN2C	0.9770	0.9797	0.8143	0.7316	0.7761	816
ACVRL1	0.8856	0.8517	0.8421	0.8372	0.8434	817

HK2	0.9440	0.9865	0.8319	0.7546	0.7689	818
NANOG	0.9397	0.9195	0.8226	0.7742	0.8385	820
EPHB4	0.9663	0.8660	0.8252	0.8049	0.8146	828
KMT2A	0.9916	0.9246	0.8022	0.7410	0.8399	835
LRRK2	0.9654	0.9146	0.7958	0.7363	0.8980	837
MAPK10	0.9815	1.1037	0.8140	0.6691	0.7477	837
LIFR	1.0050	0.8946	0.8109	0.7691	0.8153	843
EPAS1	0.9849	1.0817	0.8279	0.7010	0.7230	851
RHOA	1.0176	0.8628	0.8160	0.7927	0.8031	852
CCND1	1.0015	1.1295	0.8253	0.6732	0.6955	859
ABL1	0.9765	0.8887	0.8240	0.7916	0.8397	870
ACVR1C	1.0725	1.3126	0.8112	0.5605	0.6088	871
BCL2	0.9808	1.0310	0.8310	0.7310	0.7657	883
PTCH1	0.9504	0.9654	0.8182	0.7446	0.8860	889
PRKAR1A	1.0504	0.8762	0.8187	0.7900	0.8049	894
TEK	0.9397	0.9290	0.8272	0.7763	0.8940	894
ERBB4	0.9231	0.8664	0.8587	0.8549	0.8566	899
MED12	1.4366	0.8980	0.7846	0.7279	0.7906	900
RAC1	0.9586	0.8652	0.8422	0.8307	0.8540	900
TERT	0.9334	0.9351	0.8390	0.7910	0.8728	905
PRKCA	0.9665	0.9276	0.8353	0.7891	0.8501	908
PIK3CD	0.9274	0.9705	0.8456	0.7832	0.8546	910
LDHC	1.0172	0.8878	0.8178	0.7828	0.8557	912
MECOM	0.9412	0.9891	0.8224	0.7391	0.8924	912
EPHB3	0.9156	0.8754	0.8646	0.8592	0.8598	918
AR	0.9464	0.9297	0.8608	0.8263	0.8318	929
BRD4	1.0071	0.8921	0.8391	0.8127	0.8237	934
TSHR	0.9553	1.0711	0.8656	0.7629	0.7644	935
MYCL	0.9320	0.9590	0.8606	0.8114	0.8486	941
UQCR10	0.9673	1.0256	0.8588	0.7754	0.7858	942
THAP11	1.0517	1.0767	0.8315	0.7089	0.7470	946
EPHB6	0.9151	1.0245	0.8103	0.7031	0.9929	953
TBX3	0.9979	0.9601	0.8459	0.7888	0.8185	954
GATA2	0.9608	1.0670	0.8394	0.7255	0.8524	960
PDK1	0.9541	1.0639	0.8288	0.7112	0.8906	960
NEDD9	0.9669	0.9793	0.8348	0.7626	0.8862	963
RET	0.9703	0.9664	0.8230	0.7513	0.9128	965
EPHA2	0.9494	0.9831	0.8590	0.7969	0.8516	966

BCL2L2	1.0042	1.1218	0.8572	0.7249	0.7769	973
STAT5A	0.9259	0.9456	0.8697	0.8318	0.8689	975
CBFB	0.9925	0.9633	0.8490	0.7918	0.8355	977
EPHB2	0.9576	1.0201	0.8610	0.7815	0.8523	1000
DNMT1	1.1596	1.2466	0.8473	0.6476	0.6592	1001
CRIPAK	1.0275	0.9308	0.8374	0.7907	0.8665	1007
DVL1	1.0196	0.9393	0.8565	0.8151	0.8308	1011
CRKL	1.1193	1.0698	0.8365	0.7198	0.7745	1018
ZEB1	0.9355	0.9838	0.8645	0.8048	0.9025	1023
FYN	0.9552	1.0232	0.8303	0.7338	0.9451	1026
CDK4	1.0189	0.8754	0.8620	0.8552	0.8566	1027
EPHA1	0.9618	0.9496	0.8523	0.8037	0.9184	1030
PGK2	0.9392	0.9469	0.8740	0.8376	0.9093	1044
PTPN11	1.0348	0.9249	0.8323	0.7860	0.9171	1045
EPHA4	1.0059	1.1043	0.8659	0.7467	0.8138	1047
ZNF217	1.0449	0.9679	0.8259	0.7549	0.9144	1057
ADSS	1.1037	0.8864	0.8550	0.8393	0.8417	1066
TYK2	0.9454	0.9190	0.8872	0.8713	0.9081	1068
CDK3	1.0961	1.2020	0.8770	0.7144	0.7256	1069
ESR2	1.0246	0.9141	0.8655	0.8412	0.8766	1072
FBP2	1.0012	0.9964	0.8593	0.7907	0.8881	1073
PDK3	0.9204	0.9466	0.8817	0.8493	0.9305	1074
ABL2	0.9975	1.0183	0.8223	0.7243	1.0032	1079
PGAM2	0.9612	0.9477	0.8704	0.8317	0.9232	1083
DNMT3B	0.9385	0.9196	0.9006	0.8912	0.8991	1085
HDAC3	0.9477	1.0049	0.8677	0.7991	0.9274	1086
GPI	1.4206	0.9648	0.8059	0.7264	0.9037	1096
HDAC9	1.1904	0.9678	0.8081	0.7282	0.9230	1097
ACVR1B	1.0095	1.0610	0.8639	0.7653	0.8804	1100
CDK9	0.9757	1.0044	0.8785	0.8155	0.8817	1100
SNAI2	1.0154	0.9838	0.8627	0.8022	0.8968	1102
CTNNB1	0.9475	0.9190	0.9024	0.8941	0.9025	1103
PKN3	0.9882	0.9452	0.8773	0.8433	0.8982	1103
CSF1R	0.9786	1.1065	0.8785	0.7645	0.8662	1109
ARAF	0.9749	0.9337	0.8745	0.8449	0.9320	1112
MAPK8IP1	0.9835	0.9579	0.8851	0.8487	0.8887	1115
RICTOR	1.0996	1.2450	0.8824	0.7012	0.7826	1123
JAK1	1.0329	1.0655	0.8849	0.7947	0.8277	1139

AJUBA	1.0459	0.9429	0.8724	0.8371	0.8979	1140
MYCN	1.0112	0.9645	0.8781	0.8350	0.9040	1145
ControlA2	0.9403	0.9831	0.8896	0.8429	0.9418	1145
DNMT3A	0.9729	0.9433	0.9083	0.8908	0.8967	1152
PRKCI	0.9544	1.0052	0.8955	0.8406	0.9095	1152
FBP1	1.0490	0.9914	0.8728	0.8135	0.8808	1159
MAP3K1	0.9527	0.9456	0.9108	0.8935	0.9121	1159
EPHA8	1.0043	0.9431	0.9066	0.8884	0.8905	1168
EPHA10	1.0943	1.0778	0.8603	0.7515	0.8879	1174
PRKAG1	1.0066	1.1133	0.8962	0.7877	0.8662	1177
BTK	0.9776	0.9534	0.9083	0.8857	0.9112	1182
PIK3R1	0.9803	1.0233	0.8841	0.8145	0.9341	1189
HIF1A	1.0083	0.9263	0.9013	0.8888	0.9175	1198
CREBBP	1.1468	1.0738	0.8674	0.7641	0.8618	1199
MOS	0.9773	0.9737	0.9165	0.8880	0.8987	1199
PRKCE	0.9677	0.9961	0.8931	0.8416	0.9420	1199
ACVR1	1.0436	0.9596	0.8927	0.8592	0.8985	1210
AKT2	1.0079	0.9899	0.9116	0.8725	0.8844	1214
SMAD9	1.0669	1.0044	0.8954	0.8410	0.8587	1215
MAP2K5	1.0502	0.9467	0.8867	0.8567	0.9163	1221
ControlB5	1.2338	1.0153	0.8819	0.8153	0.8158	1221
EPHA7	1.0247	1.0036	0.8987	0.8462	0.8990	1229
EGFR	1.0961	1.0383	0.8866	0.8107	0.8737	1240
ControlB2	1.0000	0.9593	0.9243	0.9069	0.9146	1244
MAPK12	1.0087	1.0504	0.8763	0.7893	1.0026	1245
PDGFRA	1.0724	1.0171	0.8763	0.8059	0.9297	1248
FOXL2	1.0562	0.9737	0.9069	0.8734	0.8914	1250
LYN	1.0160	1.0107	0.8870	0.8251	0.9543	1251
WT1	0.9972	1.0379	0.9164	0.8557	0.9125	1263
GLI2	1.0161	0.9834	0.9260	0.8974	0.9015	1277
LTK	1.0932	1.1694	0.9075	0.7765	0.8771	1289
TLR4	0.9850	1.0683	0.9097	0.8304	0.9858	1297
GNA11	1.0428	1.0704	0.9000	0.8148	0.9377	1302
RORA	1.0738	0.9683	0.9130	0.8854	0.9126	1302
JAK2	1.2257	1.1642	0.9078	0.7795	0.8349	1304
PRKCH	1.0421	0.9455	0.9257	0.9158	0.9338	1304
HDAC7	1.0769	1.1466	0.9194	0.8059	0.8606	1312
SDHA	1.0701	1.0620	0.9271	0.8596	0.8756	1324

HDAC11	1.1277	0.9902	0.8856	0.8332	0.9778	1333
TIE1	1.1272	1.1425	0.8793	0.7478	0.9688	1333
TWIST1	1.0338	1.0400	0.9103	0.8454	0.9458	1333
RALB	1.0048	0.9890	0.9358	0.9092	0.9637	1336
PDGFRB	1.0142	1.0768	0.9171	0.8373	0.9545	1337
NOTCH2	1.1286	1.1066	0.9262	0.8360	0.8474	1338
STAT2	1.4718	0.9739	0.8831	0.8377	0.9213	1339
NOTCH3	1.0155	0.9931	0.9420	0.9165	0.9260	1345
AKT1	1.1203	1.0943	0.9156	0.8262	0.8907	1347
RPTOR	1.3146	1.3465	0.9545	0.7585	0.7992	1350
AKT3	1.1479	0.9815	0.8989	0.8577	0.9499	1354
RALA	1.0364	1.1111	0.9103	0.8098	0.9870	1366
PAK1	1.1612	1.1588	0.9256	0.8089	0.8728	1372
PFKFB3	1.2244	1.0640	0.9018	0.8208	0.9152	1376
PRKCD	0.9883	1.0078	0.9553	0.9291	0.9749	1378
EGR3	1.1185	1.0349	0.9009	0.8339	0.9866	1385
MUSK	1.1015	1.0145	0.9215	0.8750	0.9408	1389
PIK3CG	1.0083	0.9983	0.9641	0.9470	0.9486	1393
LCK	1.0367	0.9897	0.9438	0.9208	0.9557	1394
HK1	1.0247	1.0073	0.9418	0.9090	0.9755	1395
TET1	1.1076	1.0971	0.9393	0.8604	0.8823	1395
NOTCH1	1.0385	0.9866	0.9446	0.9237	0.9615	1398
GNAQ	1.0595	1.0167	0.9281	0.8838	0.9793	1401
MST1R	1.0481	1.0326	0.9364	0.8882	0.9576	1405
DDR1	1.0306	1.0878	0.9529	0.8854	0.9475	1420
RPS6KB1	1.1546	1.0098	0.9080	0.8571	1.0025	1427
HRAS	1.0484	1.0124	0.9590	0.9322	0.9425	1429
BMPR1B	1.0649	0.9958	0.9583	0.9395	0.9469	1430
HIST1H2BD	1.1850	1.2364	0.9388	0.7900	0.9091	1430
ControlA1	1.0736	1.0237	0.9338	0.8888	0.9820	1431
PRKCQ	1.0706	1.0551	0.9483	0.8949	0.9353	1432
MAPK13	1.0837	1.0215	0.9344	0.8908	1.0015	1451
PRKACB	1.0451	1.0458	0.9602	0.9174	0.9666	1456
CDKN2A	1.0274	1.0805	0.9739	0.9206	0.9458	1458
BMPR2	1.1875	1.1987	0.9251	0.7882	0.9795	1465
AURKA	1.0768	1.0971	0.9270	0.8420	1.0348	1468
STAT4	1.3775	1.0721	0.9408	0.8752	0.9011	1470
PCK1	1.1395	1.1357	0.9375	0.8384	0.9541	1479

SLC16A7	1.0259	1.0434	0.9764	0.9429	0.9952	1479
STAT1	1.0618	1.0058	0.9833	0.9720	0.9960	1504
ControlB1	1.1102	1.0965	0.9718	0.9095	0.9375	1510
PRKCZ	1.0544	1.1047	0.9675	0.8990	1.0200	1525
SOX2	1.1866	1.0506	0.9720	0.9328	0.9395	1531
GAPDH	1.1046	1.1811	0.9398	0.8192	1.1370	1532
PRKCB	1.1216	1.1473	0.9683	0.8788	0.9712	1541
SMAD6	1.2942	1.2842	0.9751	0.8205	0.9163	1542
CDKN1B	1.0867	1.0932	0.9672	0.9041	1.0645	1547
GLS	1.0818	1.0272	0.9930	0.9759	1.0077	1552
LDHB	1.0440	1.0936	1.0004	0.9538	1.0074	1552
MAP2K2	1.0707	1.1914	0.9889	0.8877	0.9955	1558
KLF4	1.0851	1.0815	0.9741	0.9204	1.0632	1560
PRKCG	1.0898	1.1001	0.9772	0.9158	1.0117	1562
SLC2A2	1.0543	1.0639	1.0061	0.9773	1.0279	1563
TSHZ3	1.0702	1.1238	0.9830	0.9127	1.0315	1563
HIST1H3B	1.2074	1.1105	0.9414	0.8568	1.0969	1570
B4GALT3	1.1571	1.3263	1.0239	0.8727	0.9223	1582
ControlA4	1.0910	1.1329	1.0050	0.9411	0.9896	1593
ERBB3	1.1227	1.1252	0.9874	0.9185	0.9960	1594
ControlB3	1.0836	1.1534	1.0132	0.9431	0.9723	1595
AXL	1.1403	1.2335	1.0127	0.9023	0.9384	1597
REL	1.1600	1.0279	1.0009	0.9874	1.0112	1603
TYRO3	1.1420	1.0739	0.9846	0.9400	1.0653	1603
FGFR1	1.2344	1.1309	0.9820	0.9075	0.9807	1609
STAT3	1.1474	1.1421	0.9923	0.9175	0.9933	1611
CHEK2	1.1049	1.1083	1.0092	0.9596	1.0547	1630
ARID5B	1.2001	1.2316	1.0261	0.9234	0.9356	1636
MYD88	1.1080	1.1912	1.0076	0.9158	1.0333	1636
PGK1	1.1722	1.0880	1.0097	0.9705	1.0085	1637
EPHA6	1.2999	1.4848	1.0831	0.8823	0.9158	1643
DDR2	1.1357	1.1289	1.0107	0.9516	1.0259	1644
NFE2L2	1.1855	1.2400	0.9973	0.8760	1.0740	1647
JAK3	1.0997	1.1386	1.0296	0.9751	1.1181	1671
STAT5B	1.2711	1.2695	1.0182	0.8925	0.9865	1673
VEZF1	1.1018	1.1713	1.0269	0.9547	1.1456	1684
FGR	1.1864	1.2150	1.0346	0.9444	1.0106	1695
FOXA1	1.2450	1.1722	1.0361	0.9680	0.9975	1702

SLC16A1	1.1566	1.2025	1.0647	0.9958	1.0066	1703
AURKC	1.2144	1.1251	1.0378	0.9941	1.0820	1710
H3F3C	1.1641	1.1245	1.0822	1.0611	1.1188	1719
SMO	1.1806	1.2197	1.0426	0.9540	1.1171	1724
LDHA	1.2116	1.1784	1.0790	1.0293	1.0872	1741
SIN3A	1.2719	1.1390	1.0804	1.0511	1.0940	1751
MET	1.2178	1.2208	1.0866	1.0195	1.0741	1758
FASN	1.2084	1.1852	1.0968	1.0526	1.1047	1759
FGFR4	1.1871	1.2113	1.1092	1.0582	1.0834	1760
TUBD1	1.2085	1.1834	1.1033	1.0633	1.1216	1769
DVL3	1.2675	1.3775	1.0790	0.9297	1.1283	1772
IGF1R	1.5013	1.1419	1.1002	1.0794	1.0795	1781
EPHA5	1.2789	1.2581	1.0898	1.0056	1.1423	1800
MAPK3	1.2565	1.2278	1.1447	1.1032	1.1143	1802
BRAF	1.4393	1.2815	1.0803	0.9798	1.1447	1805
PRKAG2	1.2069	1.2125	1.1639	1.1396	1.1644	1806
SMAD7	1.2360	1.3364	1.0922	0.9701	1.2653	1806
IDH3A	1.4858	1.2482	1.0735	0.9861	1.2013	1809
PIK3CA	1.2603	1.1809	1.1539	1.1404	1.1643	1809
ACVR2B	1.3950	1.3760	1.0920	0.9500	1.2132	1811
PKM	1.4587	1.3734	1.0952	0.9561	1.1401	1813
H3F3A	1.2424	1.2741	1.1520	1.0910	1.1310	1815
CHUK	1.4414	1.2011	1.1330	1.0989	1.1481	1822
TET2	1.2712	1.3260	1.1242	1.0232	1.2135	1827
GNAS	1.2493	1.2890	1.1443	1.0719	1.2268	1830
ERBB2	1.2574	1.3232	1.1579	1.0753	1.2629	1842
EZH2	1.5621	1.5312	1.1541	0.9656	1.2222	1852
NFKB1	1.3916	1.3467	1.2029	1.1310	1.2004	1859
IDH3G	1.4310	1.2731	1.1940	1.1545	1.2578	1861
HDAC1	1.5103	1.7372	1.2889	1.0648	1.1478	1872
MDM2	1.6247	1.5226	1.2668	1.1389	1.3396	1894
MAPK14	1.5585	1.4692	1.2857	1.1940	1.3080	1895
MYC	1.5204	1.7700	1.3535	1.1452	1.2714	1901
CDKN1A	1.7883	1.6312	1.3408	1.1956	1.3445	1908
MAPK1	1.9372	1.5613	1.4483	1.3918	1.4461	1917
PHGDH	1.9229	1.7671	1.4780	1.3335	1.7002	1922
IKBKB	1.8328	1.7732	1.5851	1.4910	1.5947	1925
MAP2K1	2.3255	1.8107	1.4838	1.3203	1.6078	1928

IDH3B	1.7971	1.7875	1.6386	1.5642	1.7698	1930
RELA	2.1743	2.2372	1.9274	1.7726	2.0795	1939

**DRA
REP2**

Gene	DM_mean	DM_median	three_score	GARP_score	sb_score	cum_rank
XIAP	0.4232	0.1463	0.1170	0.1024	0.1092	5
BCL2L1	0.6211	0.6729	0.4172	0.2894	0.3059	24
TBL1XR1	0.7081	0.6408	0.4031	0.2843	0.4506	24
IDH1	0.5779	0.5332	0.4350	0.3858	0.4980	30
CDK2	0.7594	0.6638	0.4781	0.3852	0.6382	70
SRC	0.7956	0.7369	0.5735	0.4918	0.5821	98
KAT6A	0.8323	0.7236	0.5307	0.4343	0.5988	103
RAD21	0.8928	0.6608	0.5300	0.4646	0.5594	105
RAC1	0.7686	0.7894	0.6093	0.5192	0.5782	108
SMC1A	0.7410	0.8371	0.5698	0.4361	0.5909	115
NSD1	0.7780	0.7496	0.6408	0.5863	0.6332	135
BCL2A1	0.7912	0.7545	0.6485	0.5954	0.6008	139
KRAS	0.7868	0.7074	0.6399	0.6062	0.6294	139
HDAC8	0.7868	0.8936	0.5456	0.3717	0.4126	140
PRKAA1	0.8659	0.7588	0.6188	0.5487	0.5969	147
MCL1	0.8518	0.8476	0.6218	0.5089	0.5677	166
HIF1A	0.7862	0.8380	0.6255	0.5192	0.6794	169
HDAC6	0.7690	0.6815	0.6556	0.6427	0.6444	171
NFKB2	0.7503	0.9471	0.5488	0.3497	0.5156	171
PPP2R1A	0.9016	0.8818	0.5181	0.3363	0.4268	171
VEZF1	0.8640	0.8141	0.6536	0.5734	0.5991	180
RPL22	0.7717	0.6787	0.6632	0.6555	0.6735	190
MDM4	0.7520	0.7111	0.6576	0.6308	0.7103	193
CDK11A	0.7961	0.9314	0.6089	0.4477	0.5613	194
PRKCI	0.9002	0.6889	0.6353	0.6086	0.6806	199
INTS4	0.8111	0.6898	0.6595	0.6444	0.6869	206
MAPK12	0.8264	0.7831	0.6687	0.6116	0.6712	206
RPL5	0.7637	0.9866	0.5764	0.3712	0.4294	206
PRKAG2	0.8834	0.7118	0.6516	0.6215	0.6714	207
SPOP	0.8056	0.8846	0.6743	0.5691	0.5967	214
CDK6	0.8200	0.7906	0.6860	0.6337	0.6396	226

BMPR1A	0.8400	0.7048	0.6663	0.6470	0.6918	229
CDK8	0.8269	0.7397	0.6668	0.6303	0.7245	231
SKP2	0.8295	0.8475	0.6884	0.6089	0.6268	235
TALDO1	0.8181	0.8058	0.6658	0.5957	0.7579	239
ACVR1	0.8000	0.8484	0.6864	0.6054	0.6939	246
NCOA3	0.8010	0.9242	0.6828	0.5620	0.6124	246
GLI1	1.0222	0.7988	0.6308	0.5468	0.5506	259
PRKACG	0.9586	0.8433	0.6613	0.5703	0.6309	267
SNAI2	0.7788	0.7544	0.7184	0.7003	0.7019	277
ControlA2	0.7959	0.7977	0.6875	0.6324	0.7752	280
HDAC3	0.8427	0.8288	0.7159	0.6595	0.6730	292
SMAD6	0.8901	0.7841	0.6899	0.6428	0.7323	295
PARP10	0.9136	0.7581	0.6753	0.6339	0.7520	298
PCBP1	0.9300	1.0516	0.4829	0.1985	0.2642	302
STK11	1.0303	0.7569	0.6513	0.5985	0.6899	319
MDM2	0.9850	0.8210	0.6744	0.6011	0.6906	321
AR	0.8764	0.8381	0.6872	0.6117	0.7899	324
NRAS	0.9094	0.8855	0.7025	0.6110	0.6881	328
HCK	0.9011	0.8513	0.7009	0.6256	0.7465	330
CAD	0.8303	0.8683	0.6962	0.6102	0.7900	331
EPAS1	0.9457	0.8352	0.7066	0.6424	0.6693	331
HK1	0.8606	0.8115	0.7240	0.6803	0.7578	345
TUBD1	0.8940	0.8776	0.7130	0.6306	0.7469	353
GNAQ	0.8132	0.8144	0.7513	0.7197	0.7660	365
PRKCE	0.9383	0.7858	0.7232	0.6919	0.7258	365
ACVR2A	0.8708	0.8528	0.7156	0.6470	0.7892	370
MAPK10	0.9185	0.9556	0.7231	0.6069	0.6708	374
PTPN11	0.8395	0.8366	0.7518	0.7094	0.7535	375
USP9X	0.8176	0.7744	0.7534	0.7429	0.7666	379
DHFR	1.3748	0.5924	0.4952	0.4466	0.5677	387
SLC2A1	1.0547	0.8609	0.6893	0.6035	0.6383	394
ACVR1C	1.0766	0.9012	0.6741	0.5605	0.6051	406
CS	0.9436	1.0959	0.6571	0.4377	0.5209	406
CHEK2	0.9998	0.9315	0.7074	0.5953	0.6751	415
TEK	0.8585	0.8286	0.7627	0.7297	0.7878	416
PRKAB2	0.9346	1.0199	0.6882	0.5223	0.7156	418
LIFR	0.9977	0.8221	0.7009	0.6403	0.7793	419
LYN	0.8860	0.8853	0.7433	0.6724	0.8039	434

LRRK2	1.0533	0.8250	0.7148	0.6597	0.7147	448
GLI2	0.9702	0.8437	0.7603	0.7186	0.7271	451
PCK1	0.8792	0.9411	0.7763	0.6940	0.7137	452
FBP1	1.0246	0.7830	0.7253	0.6964	0.7676	460
SOX2	0.9953	0.7801	0.7488	0.7331	0.7516	464
RPS6KB1	0.8473	0.8264	0.7831	0.7615	0.7903	466
SLC16A4	0.9137	0.8710	0.7795	0.7338	0.7520	471
PRKAB1	0.9238	0.9862	0.7287	0.5999	0.8003	476
SMC3	4.3395	0.8744	0.4448	0.2300	0.2697	478
PDGFRB	1.0382	0.8612	0.7380	0.6764	0.7068	481
SDHA	0.9004	0.8625	0.7701	0.7239	0.8122	484
TKT	1.2814	0.7106	0.6567	0.6298	0.6881	493
DNMT1	1.2120	0.7272	0.6864	0.6660	0.6775	497
RHOA	0.8485	0.8716	0.7661	0.7133	0.8503	501
CCNE1	0.9538	1.0571	0.7416	0.5839	0.7180	502
SLC25A1	1.0814	1.1416	0.5539	0.2601	0.2989	505
FLT1	0.9377	1.0215	0.7458	0.6079	0.7707	509
NOTCH4	0.9904	1.1136	0.7297	0.5378	0.5446	513
G6PD	1.3751	0.7759	0.6743	0.6234	0.6332	515
KMT2A	0.9906	0.8975	0.7807	0.7223	0.7482	539
ACLY	0.9518	0.8762	0.7790	0.7304	0.8074	540
EPHB6	0.8901	0.8923	0.7873	0.7348	0.8317	549
HDAC4	0.9422	0.8157	0.7924	0.7807	0.8043	552
FLT3	0.9607	0.9029	0.7911	0.7352	0.7658	553
GNA11	0.8472	0.8310	0.8142	0.8058	0.8099	553
PGK1	1.0395	1.1802	0.7042	0.4663	0.5356	560
SLC2A3	0.9260	1.0813	0.7099	0.5242	0.8362	562
ABL2	0.9152	0.9247	0.8100	0.7527	0.7826	564
FRK	0.9627	0.9968	0.7460	0.6206	0.8264	566
CTNNB1	0.9314	0.9995	0.8080	0.7123	0.7400	568
EPHA5	1.0605	0.8101	0.7709	0.7513	0.7664	571
PKN2	0.9433	1.0125	0.7784	0.6613	0.7906	581
DVL3	0.8670	0.9137	0.8162	0.7675	0.8111	582
ZEB1	0.9553	0.9992	0.8013	0.7023	0.7484	586
UQCR10	0.9190	0.9334	0.8102	0.7487	0.7981	587
PRKCH	0.9626	0.8119	0.8020	0.7970	0.8068	588
TLR4	1.0708	0.9996	0.7659	0.6491	0.6508	593
SMAD2	0.8869	0.9666	0.8099	0.7315	0.8233	595

HDAC9	0.9649	0.9398	0.7965	0.7248	0.8060	598
ControlB1	0.9353	0.9094	0.8172	0.7711	0.7829	599
LCK	0.9778	0.9694	0.7697	0.6698	0.8304	601
ARID5B	0.9263	0.9580	0.8091	0.7346	0.8219	616
PRKAR2B	0.8982	0.9557	0.7717	0.6797	0.9214	620
PKM	0.9086	0.9591	0.7455	0.6387	0.9553	621
NFE2L2	0.9923	1.0435	0.7871	0.6589	0.7536	625
CDK5	0.8991	0.9837	0.8136	0.7286	0.8339	626
SF3B1	1.1447	1.0367	0.7364	0.5862	0.7002	627
RORA	1.0280	0.8858	0.7764	0.7218	0.8362	631
GAPDH	1.1028	0.8356	0.7862	0.7615	0.7882	647
FBP2	0.9186	0.9384	0.8381	0.7879	0.7894	649
YAP1	1.8333	0.9273	0.7157	0.6099	0.6154	651
YES1	1.0574	0.9232	0.7937	0.7290	0.7986	654
PIK3R1	0.9368	0.8393	0.8237	0.8160	0.8382	660
PRKAA2	0.9495	0.8560	0.8175	0.7982	0.8531	675
CCND1	0.9781	1.0066	0.8133	0.7167	0.8157	678
LDHA	0.9640	0.8610	0.8170	0.7950	0.8547	682
TSHZ2	1.1823	0.8512	0.7651	0.7221	0.8171	684
HSP90AB1	1.1137	1.0656	0.7688	0.6204	0.7538	693
ACVRL1	0.9765	0.8778	0.8175	0.7873	0.8500	696
ControlA1	0.9421	0.8577	0.8339	0.8220	0.8399	697
HSP90AA1	0.9554	0.9372	0.8433	0.7963	0.7991	705
MTOR	1.1372	0.8797	0.7523	0.6886	0.8769	708
FOXA1	1.0000	1.0253	0.8064	0.6970	0.8280	711
PGK2	0.9078	0.8582	0.8455	0.8391	0.8443	714
ROCK1	0.9236	0.8607	0.8449	0.8369	0.8397	716
RAF1	1.0039	1.1518	0.8277	0.6657	0.6859	718
PDK3	0.9824	0.9579	0.8424	0.7846	0.7986	725
ZNF217	0.9408	0.8902	0.8344	0.8065	0.8704	725
EPHA3	1.0248	0.8957	0.8298	0.7968	0.8137	731
MAP2K4	0.9913	0.8818	0.8227	0.7932	0.8726	735
CRIPAK	0.9347	0.8828	0.8486	0.8315	0.8357	736
AKT3	0.9252	0.9335	0.8473	0.8042	0.8450	745
IDH3A	1.0943	1.2356	0.8124	0.6008	0.6376	750
EPHA7	0.9408	0.8922	0.8485	0.8266	0.8415	758
GPI	1.0937	1.0955	0.7760	0.6162	0.8143	760
H3F3A	0.9460	0.9843	0.8177	0.7344	0.9280	762

CDK7	3.2593	0.7921	0.7620	0.7470	0.7814	763
RALB	1.0868	1.1082	0.8156	0.6693	0.7325	771
SLC2A2	1.0354	1.1102	0.8371	0.7005	0.7474	772
CDC37	1.3926	1.0816	0.7565	0.5939	0.6894	773
PIK3CD	0.9114	0.9798	0.8223	0.7435	0.9719	778
RPIA	1.2587	1.2407	0.7707	0.5358	0.5806	780
LDHC	1.0421	0.8937	0.8198	0.7829	0.8816	791
BDH1	1.1646	1.2086	0.7984	0.5933	0.7252	800
BMPR2	0.9741	0.8881	0.8469	0.8263	0.8752	800
ControlA5	0.9791	0.9217	0.8446	0.8061	0.8787	801
EPHB2	0.9352	0.9860	0.8545	0.7888	0.8752	804
SMAD9	1.0116	0.9024	0.8408	0.8100	0.8730	806
PRKAR1B	0.9394	0.9601	0.8438	0.7856	0.9196	808
SRSF2	1.6797	0.9091	0.7128	0.6147	0.8981	810
POU5F1	1.0249	0.8760	0.8416	0.8244	0.8669	812
EIF4A2	1.0605	1.1367	0.8426	0.6956	0.7499	816
PGAM1	1.5008	0.9542	0.7854	0.7010	0.7734	816
PRKCZ	0.9737	0.9757	0.8583	0.7997	0.8496	818
RALA	0.9777	0.8973	0.8492	0.8252	0.8794	821
HDAC5	1.0999	0.9698	0.8181	0.7422	0.8613	823
NKX2-1	1.1308	0.9810	0.8240	0.7455	0.8273	827
EPHA6	1.1009	1.0227	0.8348	0.7409	0.8116	830
H3F3C	1.0408	1.0099	0.8463	0.7644	0.8277	833
SMAD3	0.9882	0.9226	0.8459	0.8076	0.9076	835
CARD11	0.9895	0.9258	0.8529	0.8164	0.8917	841
TGFBR2	1.0149	1.0478	0.8707	0.7821	0.7939	847
PRKCQ	0.9438	1.0313	0.8603	0.7748	0.8931	853
CDK1	0.9719	1.0895	0.8605	0.7460	0.8401	854
CDK9	1.0413	1.0794	0.8574	0.7465	0.7967	854
PAF1	1.3201	1.5338	0.7890	0.4166	0.5745	855
LDHB	0.9650	0.9910	0.8716	0.8119	0.8560	859
PRKCG	0.9670	1.0402	0.8374	0.7360	0.9500	860
MAPK13	1.0479	0.9860	0.8335	0.7573	0.9239	868
CSF1R	0.9885	0.9493	0.8642	0.8217	0.8816	871
MAP3K8	0.9959	1.0365	0.8821	0.8049	0.8120	873
ACVR1B	1.1231	0.9455	0.8353	0.7802	0.8733	878
STAT4	1.1779	0.9308	0.8410	0.7961	0.8226	878
HDAC2	0.9985	0.8959	0.8679	0.8539	0.8818	880

SMO	1.0651	0.9700	0.8213	0.7469	0.9457	881
KDR	0.9937	0.9993	0.8413	0.7623	0.9519	883
EPHB1	1.0297	1.0757	0.8793	0.7812	0.7927	891
SLC16A7	1.0151	0.8998	0.8720	0.8580	0.8757	894
EP300	1.0193	1.0581	0.8697	0.7755	0.8384	897
PAK1	1.0851	0.9715	0.8692	0.8181	0.8182	899
PRKAR2A	1.0377	0.9567	0.8711	0.8283	0.8588	911
U2AF1	0.9748	1.0465	0.8402	0.7371	1.0130	925
MAPK8	0.9939	1.1289	0.8638	0.7313	0.8820	928
BCL2L2	1.0151	1.1012	0.8789	0.7677	0.8400	934
BMPR1B	0.9933	1.0156	0.8859	0.8211	0.8684	935
THAP11	1.0712	0.9779	0.8720	0.8190	0.8490	941
SMAD1	1.0596	0.9800	0.8438	0.7758	0.9604	943
CDC42	1.2387	1.0837	0.7735	0.6184	0.9352	948
INSR	1.0698	1.0319	0.8858	0.8128	0.8258	955
GATA2	1.0529	0.9270	0.8843	0.8629	0.9020	971
HK2	1.0190	1.0045	0.8836	0.8232	0.9031	975
IKBKE	1.1142	1.1149	0.8557	0.7262	0.8625	976
ACVR2B	1.1475	0.9452	0.8505	0.8032	0.9160	983
RPTOR	1.1315	1.0822	0.8094	0.6730	0.9915	988
HIST1H1C	0.9981	0.9369	0.9029	0.8859	0.9272	993
ENO1	1.0592	1.1578	0.8890	0.7546	0.8386	999
AJUBA	0.9933	1.0844	0.8717	0.7654	0.9700	1001
ERCC2	1.2788	0.9757	0.8378	0.7689	0.8996	1003
PRKAR1A	0.9836	0.9873	0.9106	0.8722	0.9181	1007
PRKACB	1.0219	1.0340	0.8795	0.8023	0.9529	1010
FGR	1.0165	0.9614	0.8958	0.8631	0.9427	1014
GLI3	1.0058	1.0367	0.8684	0.7842	1.0141	1023
CRKL	1.2720	1.0011	0.8383	0.7569	0.9156	1028
MECOM	1.0436	1.0533	0.8982	0.8207	0.8896	1029
REL	1.0647	1.1999	0.9067	0.7601	0.8335	1034
CBL	1.0778	0.9982	0.8923	0.8393	0.9011	1040
LTK	1.1340	1.2411	0.8994	0.7285	0.8197	1043
FYN	0.9836	0.9966	0.9227	0.8858	0.9421	1048
PIK3CG	1.1237	0.9083	0.9003	0.8963	0.9066	1049
CDKN2A	1.0506	0.9884	0.9111	0.8725	0.9041	1054
MYD88	1.0867	0.9946	0.8989	0.8510	0.9159	1062
TET1	1.1501	1.0762	0.8828	0.7862	0.8671	1062

SETBP1	1.0480	0.9998	0.8860	0.8291	0.9710	1066
HIST1H2BD	1.0591	1.1676	0.9007	0.7673	0.8960	1069
GATA3	1.0636	1.0726	0.9099	0.8285	0.8896	1091
NEDD9	1.0252	1.0155	0.9342	0.8936	0.9072	1092
PRKAG3	1.1473	1.1251	0.9059	0.7962	0.8354	1093
ControlA3	1.3353	0.9260	0.8653	0.8350	0.9073	1095
SYK	1.2224	1.1995	0.9027	0.7543	0.8131	1106
TAF1	1.1867	1.1588	0.9025	0.7744	0.8283	1106
AURKB	1.2442	1.1304	0.8853	0.7627	0.8397	1108
EPHA1	1.1197	1.0432	0.8922	0.8167	0.9450	1108
IGF1R	1.1815	1.0901	0.9073	0.8160	0.8304	1110
SNAI1	1.1211	0.9573	0.9162	0.8957	0.9377	1121
MET	1.0117	1.0989	0.9383	0.8580	0.9085	1126
SLC16A3	1.0932	0.9398	0.9304	0.9257	0.9382	1127
MAPK9	1.1313	1.2251	0.9253	0.7753	0.8407	1131
NFE2L3	1.0300	1.0735	0.9197	0.8428	0.9773	1154
PCK2	1.1260	1.0345	0.9312	0.8795	0.9019	1158
SMAD7	1.0571	1.1075	0.9509	0.8725	0.8745	1158
WT1	1.2011	0.9404	0.9140	0.9009	0.9264	1162
PRKCD	1.0283	1.0436	0.9254	0.8663	0.9984	1166
ControlB5	1.0733	1.2424	0.9333	0.7788	0.9058	1168
PDGFRA	1.1263	1.0522	0.9191	0.8525	0.9343	1169
EGR3	1.1928	1.0573	0.9006	0.8223	0.9240	1172
KIT	1.2115	1.0138	0.9204	0.8737	0.8804	1176
SOX17	1.0234	1.0151	0.9392	0.9013	1.0081	1179
NOTCH3	1.0866	1.1920	0.9332	0.8037	0.9087	1180
RELB	1.1231	1.2481	0.9017	0.7285	0.9827	1187
AURKC	1.1272	1.2279	0.9582	0.8234	0.8257	1188
ESR1	1.1620	1.0589	0.9253	0.8585	0.9202	1203
CBFB	1.0908	1.0170	0.9450	0.9089	0.9706	1216
STAT3	1.3690	1.4050	0.9296	0.6918	0.8488	1219
PIK3CA	1.2505	0.9879	0.9060	0.8651	0.9616	1220
ControlB3	1.0363	1.0723	0.9794	0.9330	0.9380	1231
ENO3	1.0102	1.0955	0.9373	0.8582	1.0629	1233
CREBBP	1.1609	1.4030	0.9392	0.7073	0.9526	1241
TSHZ3	1.0680	1.0901	0.9680	0.9070	0.9313	1243
BTK	1.1283	1.0236	0.9314	0.8854	1.0097	1246
EPHA8	1.1358	1.2739	0.9436	0.7784	0.9341	1252

ESR2	1.2468	0.9769	0.9452	0.9294	0.9333	1255
MAP2K5	1.0759	1.1542	0.9616	0.8653	0.9304	1255
RGN	1.0587	1.0415	0.9769	0.9447	0.9769	1257
MPL	1.1652	1.2270	0.9264	0.7761	0.9710	1266
MAPK11	1.1947	1.1742	0.9464	0.8325	0.8768	1269
DNMT3B	1.1836	1.0398	0.9151	0.8527	1.0204	1272
AURKA	1.1786	1.0912	0.9085	0.8171	1.0247	1275
HRAS	1.0775	1.0191	0.9760	0.9544	1.0053	1286
ERBB4	1.1696	1.0697	0.9542	0.8965	0.9488	1291
ControlB4	1.0627	1.0180	0.9860	0.9701	1.0126	1291
NOTCH1	1.0610	1.0656	0.9675	0.9184	1.0271	1294
STAT5A	1.0632	1.0566	1.0003	0.9722	0.9786	1308
MOS	1.1764	1.0092	0.9607	0.9365	0.9985	1314
MYC	1.6650	1.9077	1.1005	0.6969	0.8051	1323
JAK2	1.5205	1.1079	0.9393	0.8550	0.8765	1326
ABL1	1.1594	1.1097	0.9782	0.9124	0.9293	1330
FH	1.2086	0.9973	0.9654	0.9495	0.9891	1330
PKN3	1.2789	1.1088	0.9256	0.8340	0.9780	1339
MAP3K1	1.3704	1.0285	0.9406	0.8966	0.9747	1347
STAT6	1.2142	1.0740	0.9755	0.9263	0.9409	1349
PTK2	1.1178	1.1027	0.9874	0.9298	0.9790	1350
MYCL	1.3149	1.3466	0.9950	0.8192	0.8355	1357
BLK	1.4483	0.9719	0.9655	0.9624	0.9633	1361
PIK3CB	1.1418	1.1065	0.9570	0.8823	1.0452	1361
FOXA2	1.1689	1.0662	0.9764	0.9315	1.0013	1366
IDH2	1.0858	1.0576	1.0074	0.9823	1.0181	1370
SLC16A1	1.2611	1.1025	0.9585	0.8865	0.9704	1373
JAK3	1.1882	1.2182	0.9711	0.8476	0.9606	1374
TGFBR1	1.1477	1.0757	0.9888	0.9454	0.9873	1374
E2F3	1.1615	1.2227	0.9674	0.8398	0.9874	1375
AKT2	1.3994	1.2415	0.9759	0.8431	0.8593	1378
EPHA10	1.1133	1.1332	0.9725	0.8921	1.0796	1386
PRKCA	1.0905	1.0697	1.0038	0.9709	1.0500	1388
PGD	1.7002	1.1896	0.9020	0.7582	1.1034	1389
CDK4	1.2625	1.0665	0.9593	0.9058	1.0127	1395
NANOG	1.1446	1.0860	1.0126	0.9759	0.9781	1402
EPHA2	1.1305	1.0694	1.0187	0.9933	1.0020	1405
CDK3	1.1075	1.0473	1.0348	1.0286	1.0335	1408

BRD4	1.2701	1.1060	0.9889	0.9304	0.9432	1413
ELF3	1.1492	1.0653	1.0215	0.9995	1.0064	1422
DVL1	1.1667	1.2841	0.9736	0.8183	1.0484	1427
PRKACA	1.1703	1.2451	1.0117	0.8950	0.9439	1428
NFKB1	1.2008	1.1614	1.0037	0.9248	0.9547	1429
PRX	1.2724	1.2847	0.9547	0.7897	1.0249	1429
HDAC10	1.2941	1.2378	0.9498	0.8059	1.0360	1431
STAT1	1.1833	1.0735	0.9914	0.9504	1.0534	1442
STAT5B	1.1341	1.1169	1.0164	0.9662	1.0163	1443
TYRO3	1.1005	1.1241	1.0186	0.9658	1.0543	1444
ControlA4	1.1564	1.0674	1.0174	0.9924	1.0620	1455
TET2	1.2307	1.2705	1.0058	0.8734	0.9629	1468
MST1R	1.1362	1.1232	1.0492	1.0122	1.0153	1483
PRKCB	1.2196	1.1552	0.9917	0.9099	1.0285	1483
RET	1.1804	1.1964	0.9977	0.8984	1.0750	1486
FGFR3	1.3106	1.1211	1.0034	0.9446	0.9796	1487
ControlB2	1.1268	1.1390	1.0360	0.9845	1.0509	1487
STAT2	1.1563	1.2149	1.0537	0.9731	1.0137	1517
DDR2	1.2621	1.2323	0.9835	0.8591	1.1143	1520
PGAM2	1.1176	1.1429	1.0690	1.0321	1.1094	1528
MAPK7	1.2790	1.2434	1.0412	0.9401	0.9569	1534
PTCH1	1.2012	1.3071	1.0187	0.8745	1.0401	1536
TWIST1	1.1901	1.1125	1.0571	1.0294	1.0429	1539
ERBB2	1.2302	1.3161	1.0423	0.9054	0.9822	1540
DNMT3A	1.4138	1.1627	1.0205	0.9493	0.9752	1541
ESRRB	1.2514	1.2973	1.0073	0.8623	1.0554	1544
JAK1	1.2973	1.3008	0.9897	0.8342	1.1084	1547
HDAC11	1.6804	1.1464	1.0089	0.9402	0.9813	1549
DVL2	1.1642	1.1105	1.0813	1.0667	1.0827	1550
EPHA4	1.3435	1.2230	1.0415	0.9508	0.9737	1555
FOXL2	1.2233	1.3386	1.0622	0.9240	0.9846	1559
ADSS	1.4786	1.1317	0.9831	0.9087	1.1303	1562
EGFR	1.1805	1.1527	1.0593	1.0126	1.1089	1567
NOTCH2	1.4460	1.3718	1.0514	0.8911	0.9525	1568
TYK2	1.1370	1.1554	1.0832	1.0471	1.1191	1568
POLQ	1.4120	1.1533	1.0396	0.9828	1.0044	1580
PRKAG1	1.1959	1.2560	1.0651	0.9696	1.0420	1587
EPHB4	1.4069	1.1723	1.0610	1.0054	1.0106	1609

GLS	1.1922	1.2460	1.0805	0.9978	1.0709	1615
DDR1	1.1782	1.2198	1.1025	1.0438	1.1322	1626
PKN1	1.2160	1.1444	1.1077	1.0894	1.1199	1626
CDKN1B	1.2012	1.2768	1.0764	0.9762	1.1122	1630
KLF4	1.4087	1.2016	1.0540	0.9802	1.0460	1631
FGFR1	1.2691	1.2825	1.0637	0.9542	1.0935	1639
AKT1	1.6889	1.2050	1.0468	0.9676	1.0392	1640
BCL2	1.3817	1.3933	1.0860	0.9324	1.0168	1656
HDAC7	1.2136	1.1888	1.1501	1.1307	1.1441	1662
TIE1	1.2176	1.2985	1.0876	0.9822	1.1446	1666
SMAD4	1.2319	1.2566	1.1162	1.0460	1.1036	1671
HDAC1	1.3270	1.4606	1.1406	0.9806	0.9981	1675
MUSK	1.4859	1.1835	1.0675	1.0095	1.1241	1680
PAX8	1.2436	1.2049	1.1451	1.1152	1.1627	1681
FGFR2	1.2633	1.3580	1.1281	1.0131	1.0631	1693
ARAF	1.2291	1.2098	1.1614	1.1372	1.2032	1694
GNAS	1.2798	1.2563	1.0928	1.0111	1.1621	1694
CDKN2C	1.3083	1.4273	1.0921	0.9245	1.2832	1705
B4GALT3	1.4501	1.4175	1.1235	0.9765	1.0243	1709
LMO1	1.2446	1.2758	1.1779	1.1290	1.1496	1724
MYCN	1.2767	1.2888	1.1648	1.1027	1.1156	1729
PDK1	1.4147	1.2286	1.1331	1.0853	1.1322	1730
TSHR	1.2649	1.2715	1.1756	1.1276	1.1982	1736
BRAF	2.0139	1.1986	1.0980	1.0477	1.1705	1737
IDH3G	1.3365	1.3704	1.1390	1.0233	1.1927	1747
MAPK8IP1	1.2970	1.2818	1.1521	1.0872	1.2533	1749
MAP2K2	1.4945	1.2611	1.1408	1.0806	1.1135	1751
FGFR4	1.3012	1.2434	1.2276	1.2197	1.2418	1764
TERT	1.3731	1.3333	1.1609	1.0747	1.1930	1766
FASN	1.4754	1.2253	1.2076	1.1988	1.2088	1780
TBX3	1.4343	1.2893	1.1890	1.1389	1.2050	1795
CDK12	1.3560	1.3920	1.2264	1.1436	1.2687	1803
AXL	1.3560	1.3620	1.2304	1.1646	1.3036	1807
CTCF	1.4945	1.3029	1.1849	1.1259	1.2783	1810
ERBB3	1.4142	1.3928	1.2313	1.1506	1.2073	1816
PFKFB3	1.3712	1.4256	1.2576	1.1736	1.2573	1820
IKBKB	1.6036	1.6923	1.2489	1.0272	1.1970	1823
MED12	1.4340	1.4963	1.2303	1.0973	1.4561	1833

RICTOR	1.4676	1.5152	1.2859	1.1712	1.2683	1848
SIN3A	1.5911	1.4570	1.2805	1.1922	1.2323	1851
EPHB3	1.5236	1.4337	1.3347	1.2852	1.3713	1864
ALK	1.5449	1.4825	1.3121	1.2269	1.3285	1866
MAPK3	1.7241	1.4471	1.3528	1.3056	1.3836	1879
HIST1H3B	1.7200	1.7235	1.4920	1.3762	1.5688	1893
CHUK	1.8455	1.6452	1.5262	1.4667	1.5377	1898
EZH2	2.0324	1.9113	1.5219	1.3272	1.3741	1900
CDKN1A	1.7417	1.7463	1.5433	1.4419	1.6725	1904
MAPK14	1.8843	1.8900	1.6358	1.5087	1.6129	1908
MAPK1	2.1952	2.1950	1.7882	1.5848	1.6386	1921
IDH3B	2.4052	2.0779	1.7279	1.5530	1.6569	1922
PHGDH	2.3091	2.4047	1.8089	1.5110	1.6954	1927
MAP2K1	2.2017	2.3467	1.9727	1.7857	1.8183	1930
RELA	2.5801	2.7678	2.2667	2.0161	2.0682	1938

Appendix C

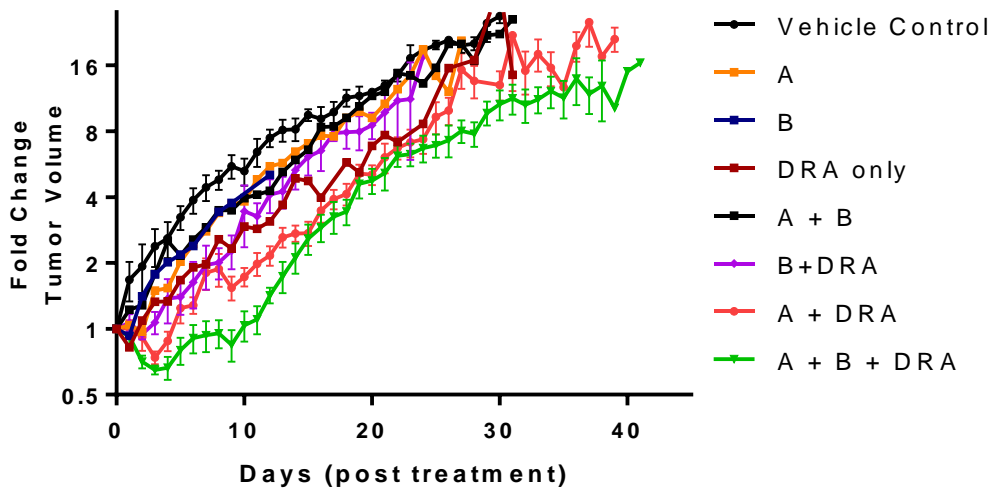


Figure 44: CRC247 PDX data over course of entire study.

DRA formulation used in these plots was ELP-DRA and abbreviated to “DRA” in descriptions. Tumor regression data; mice were treated with A-1331852 (A, 25 mg/kg daily p.o.) and/or BV6 (B, 5 mg/kg q.4.d.), and/or ELP-DRA (30 mg/kg weekly s.c.) until Day 21. Data were analyzed using two-way analysis of variance (ANOVA) of matched values followed by Fisher’s LSD multiple comparisons test to establish significance ($p < 0.05$) of the difference between groups at each day of treatment. Results indicate statistically significant tumor volumes between and including days 5 and 13 for triple combination of A-1331852 + BV6 + ELP-DRA compared to other groups.

References

1. K. Strebhardt, A. Ullrich, Paul Ehrlich's magic bullet concept: 100 years of progress. *Nat Rev Cancer* **8**, 473-480 (2008).
2. G. Kohler, C. Milstein, Continuous cultures of fused cells secreting antibody of predefined specificity. *Nature* **256**, 495-497 (1975).
3. D. R. Leach, M. F. Krummel, J. P. Allison, Enhancement of antitumor immunity by CTLA-4 blockade. *Science* **271**, 1734-1736 (1996).
4. D. Schrama, R. A. Reisfeld, J. C. Becker, Antibody targeted drugs as cancer therapeutics. *Nat Rev Drug Discov* **5**, 147-159 (2006).
5. C. Gronwall, S. Stahl, Engineered affinity proteins--generation and applications. *J Biotechnol* **140**, 254-269 (2009).
6. L. M. Weiner, R. Surana, S. Wang, Monoclonal antibodies: versatile platforms for cancer immunotherapy. *Nat Rev Immunol* **10**, 317-327 (2010).
7. P. J. Carter, G. A. Lazar, Next generation antibody drugs: pursuit of the 'high-hanging fruit'. *Nat Rev Drug Discov* **17**, 197-223 (2018).
8. A. M. Scott, J. D. Wolchok, L. J. Old, Antibody therapy of cancer. *Nat Rev Cancer* **12**, 278-287 (2012).
9. P. Holliger, P. J. Hudson, Engineered antibody fragments and the rise of single domains. *Nat Biotechnol* **23**, 1126-1136 (2005).

10. F. Li, J. V. Ravetch, Inhibitory Fcγ receptor engagement drives adjuvant and anti-tumor activities of agonistic CD40 antibodies. *Science* **333**, 1030-1034 (2011).
11. F. Li, J. V. Ravetch, Apoptotic and antitumor activity of death receptor antibodies require inhibitory Fcγ receptor engagement. *Proc Natl Acad Sci U S A* **109**, 10966-10971 (2012).
12. Y. Xu, A. J. Szalai, T. Zhou, K. R. Zinn, T. R. Chaudhuri, X. Li, W. J. Koopman, R. P. Kimberly, FcγRs Modulate Cytotoxicity of Anti-Fas Antibodies: Implications for Agonistic Antibody-Based Therapeutics. *The Journal of Immunology* **171**, 562 (2003).
13. R. Stewart, S. A. Hammond, M. Oberst, R. W. Wilkinson, The role of Fc gamma receptors in the activity of immunomodulatory antibodies for cancer. *Journal for ImmunoTherapy of Cancer* **2**, 29 (2014).
14. J. S. Swers, L. Grinberg, L. Wang, H. Feng, K. Lekstrom, R. Carrasco, Z. Xiao, I. Inigo, C. C. Leow, H. Wu, D. A. Tice, M. Baca, Multivalent scaffold proteins as superagonists of TRAIL receptor 2-induced apoptosis. *Mol Cancer Ther* **12**, 1235-1244 (2013).
15. V. Pillay, H. K. Gan, A. M. Scott, Antibodies in oncology. *N Biotechnol* **28**, 518-529 (2011).
16. G. M. Thurber, M. M. Schmidt, K. D. Wittrup, Antibody tumor penetration: transport opposed by systemic and antigen-mediated clearance. *Adv Drug Deliv Rev* **60**, 1421-1434 (2008).
17. M. M. Schmidt, K. D. Wittrup, A modeling analysis of the effects of molecular size and binding affinity on tumor targeting. *Mol Cancer Ther* **8**, 2861-2871 (2009).

18. K. E. Tiller, P. M. Tessier, Advances in Antibody Design. *Annu Rev Biomed Eng* **17**, 191-216 (2015).
19. E. Fischer, *Engineering in Translational Medicine*. W. Cai, Ed., (Springer, 2014).
20. J. R. Kintzing, M. V. Filsinger Interrante, J. R. Cochran, Emerging Strategies for Developing Next-Generation Protein Therapeutics for Cancer Treatment. *Trends Pharmacol Sci* **37**, 993-1008 (2016).
21. E. S. Ward, D. Gussow, A. D. Griffiths, P. T. Jones, G. Winter, Binding activities of a repertoire of single immunoglobulin variable domains secreted from *Escherichia coli*. *Nature* **341**, 544-546 (1989).
22. T. Wurch, A. Pierre, S. Depil, Novel protein scaffolds as emerging therapeutic proteins: from discovery to clinical proof-of-concept. *Trends Biotechnol* **30**, 575-582 (2012).
23. H. K. Binz, P. Amstutz, A. Pluckthun, Engineering novel binding proteins from nonimmunoglobulin domains. *Nat Biotechnol* **23**, 1257-1268 (2005).
24. B. Leader, Q. J. Baca, D. E. Golan, Protein therapeutics: a summary and pharmacological classification. *Nat Rev Drug Discov* **7**, 21-39 (2008).
25. R. Vazquez-Lombardi, T. G. Phan, C. Zimmermann, D. Lowe, L. Jermutus, D. Christ, Challenges and opportunities for non-antibody scaffold drugs. *Drug Discov Today* **20**, 1271-1283 (2015).
26. M. Gebauer, A. Skerra, Engineered protein scaffolds as next-generation antibody therapeutics. *Curr Opin Chem Biol* **13**, 245-255 (2009).
27. J. Sörensen, D. Sandberg, M. Sandström, A. Wennborg, J. Feldwisch, V. Tolmachev, G. Åström, M. Lubberink, U. Garske-Román, J. Carlsson, H.

- Lindman, First-in-human molecular imaging of her2 expression in breast cancer metastases using the 111in-aby-025 affibody molecule. *Journal of Nuclear Medicine* **55**, 730-735 (2014).
28. P. C. Cirino, S. Qian, in *Synthetic Biology*, H. Zhao, Ed. (Academic Press, Boston, 2013), pp. 23-42.
 29. K. M. Ferguson, M. B. Berger, J. M. Mendrola, H.-S. Cho, D. J. Leahy, M. A. Lemmon, Egf activates its receptor by removing interactions that autoinhibit ectodomain dimerization. *Molecular Cell* **11**, 507-517 (2003).
 30. S. Koide, A. Koide, D. Lipovšek, in *Methods in Enzymology*, K. D. Wittrup, G. L. Verdine, Eds. (Academic Press, 2012), vol. 503, pp. 135-156.
 31. A. Koide, C. W. Bailey, X. Huang, S. Koide, The fibronectin type III domain as a scaffold for novel binding proteins. *J Mol Biol* **284**, 1141-1151 (1998).
 32. A. L. Main, T. S. Harvey, M. Baron, J. Boyd, I. D. Campbell, The three-dimensional structure of the tenth type III module of fibronectin: An insight into RGD-mediated interactions. *Cell* **71**, 671-678 (1992).
 33. B. J. Hackel, A. Kapila, K. D. Wittrup, Picomolar affinity fibronectin domains engineered utilizing loop length diversity, recursive mutagenesis, and loop shuffling. *J Mol Biol* **381**, 1238-1252 (2008).
 34. D. Lipovsek, Adnectins: engineered target-binding protein therapeutics. *Protein Eng Des Sel* **24**, 3-9 (2011).
 35. R. Mamluk, I. M. Carvajal, B. A. Morse, H. Wong, J. Abramowitz, S. Aslanian, A.-C. Lim, J. Gokemeijer, M. J. Storek, J. Lee, M. Gosselin, M. C. Wright, R. T. Camphausen, J. Wang, Y. Chen, K. Miller, K. Sanders, S. Short, J. Sperinde, G. prasad, S. Williams, R. Kerbel, J. ebos, A. Mutsaers, J. D. Mendlein, A. S. Harris,

- E. S. Furfine, Anti-tumor effect of CT-322 as an adnectin inhibitor of vascular endothelial growth factor receptor-2. *mAbs* **2**, 199-208 (2010).
36. J. Lemke, S. von Karstedt, J. Zinngrebe, H. Walczak, Getting TRAIL back on track for cancer therapy. *Cell Death Differ* **21**, 1350-1364 (2014).
37. S. von Karstedt, A. Montinaro, H. Walczak, Exploring the TRAILs less travelled: TRAIL in cancer biology and therapy. *Nat Rev Cancer* **17**, 352-366 (2017).
38. M. van Dijk, A. Halpin-McCormick, T. Sessler, A. Samali, E. Szegezdi, Resistance to TRAIL in non-transformed cells is due to multiple redundant pathways. *Cell Death & Disease* **4**, e702 (2013).
39. D. W. Stuckey, K. Shah, TRAIL on trial: preclinical advances in cancer therapy. *Trends Mol Med* **19**, 685-694 (2013).
40. P. J. Kaplan-Lefko, J. D. Graves, S. J. Zoog, Y. Pan, J. Wall, D. G. Branstetter, J. Moriguchi, A. Coxon, J. N. Huard, R. Xu, M. L. Peach, M. L. Peach, G. Juan, S. Kaufman, Q. Chen, A. Bianchi, J. J. Kordich, M. Ma, I. N. Foltz, B. C. Gliniak, Conatumumab, a fully human agonist antibody to death receptor 5, induces apoptosis via caspase activation in multiple tumor types. *Cancer Biology & Therapy* **9**, 618-631 (2014).
41. R. N. Gilbreth, B. M. Chacko, L. Grinberg, J. S. Swers, M. Baca, Stabilization of the third fibronectin type III domain of human tenascin-C through minimal mutation and rational design. *Protein Eng Des Sel* **27**, 411-418 (2014).
42. V. P. Torchilin, A. N. Lukyanov, Peptide and protein drug delivery to and into tumors: challenges and solutions. *Drug Discovery Today* **8**, 259-266 (2003).
43. Y. Lu, J. Yang, E. Sega, Issues related to targeted delivery of proteins and peptides. *AAPS J* **8**, E466-478 (2006).

44. A. Patel, K. Cholkar, A. K. Mitra, Recent developments in protein and peptide parenteral delivery approaches. *Ther Deliv* **5**, 337-365 (2014).
45. F. M. Veronese, Peptide and protein PEGylation: a review of problems and solutions. *Biomaterials* **22**, 405-417 (2001).
46. J. M. Anderson, M. S. Shive, Biodegradation and biocompatibility of PLA and PLGA microspheres. *Advanced Drug Delivery Reviews* **28**, 5-24 (1997).
47. S. R. MacEwan, A. Chilkoti, Elastin-like polypeptides: biomedical applications of tunable biopolymers. *Biopolymers* **94**, 60-77 (2010).
48. D. E. Meyer, A. Chilkoti, Purification of recombinant proteins by fusion with thermally-responsive polypeptides. *Nat Biotechnol* **17**, 1112-1115 (1999).
49. D. E. Meyer, K. Trabbic-Carlson, A. Chilkoti, Protein purification by fusion with an environmentally responsive elastin-like polypeptide: effect of polypeptide length on the purification of thioredoxin. *Biotechnol Prog* **17**, 720-728 (2001).
50. W. Hassouneh, S. R. MacEwan, A. Chilkoti, Fusions of elastin-like polypeptides to pharmaceutical proteins. *Methods Enzymol* **502**, 215-237 (2012).
51. M. Amiram, K. M. Luginbuhl, X. Li, M. N. Feinglos, A. Chilkoti, Injectable protease-operated depots of glucagon-like peptide-1 provide extended and tunable glucose control. *Proc Natl Acad Sci U S A* **110**, 2792-2797 (2013).
52. B. Vogelstein, N. Papadopoulos, V. E. Velculescu, S. Zhou, L. A. Diaz, Jr., K. W. Kinzler, Cancer genome landscapes. *Science* **339**, 1546-1558 (2013).
53. L. Wang, D. A. Wheeler, Genomic sequencing for cancer diagnosis and therapy. *Annu Rev Med* **65**, 33-48 (2014).

54. D. M. Hyman, B. S. Taylor, J. Baselga, Implementing Genome-Driven Oncology. *Cell* **168**, 584-599 (2017).
55. J. S. Boehm, W. C. Hahn, Towards systematic functional characterization of cancer genomes. *Nat Rev Genet* **12**, 487-498 (2011).
56. X. Hu, Z. Zhang, Understanding the genetic mechanisms of cancer drug resistance using genomic approaches. *Trends Genet* **32**, 127-137 (2016).
57. J. W. Tyner, Integrating functional genomics to accelerate mechanistic personalized medicine. *Cold Spring Harb Mol Case Stud* **3**, a001370 (2017).
58. A. N. Hata, A. Yeo, A. C. Faber, E. Lifshits, Z. Chen, K. A. Cheng, Z. Walton, K. A. Sarosiek, A. Letai, R. S. Heist, M. Mino-Kenudson, K. K. Wong, J. A. Engelman, Failure to induce apoptosis via BCL-2 family proteins underlies lack of efficacy of combined MEK and PI3K inhibitors for KRAS-mutant lung cancers. *Cancer Res* **74**, 3146-3156 (2014).
59. X. Yang, J. S. Boehm, X. Yang, K. Salehi-Ashtiani, T. Hao, Y. Shen, R. Lubonja, S. R. Thomas, O. Alkan, T. Bhimdi, T. M. Green, C. M. Johannessen, S. J. Silver, C. Nguyen, R. R. Murray, H. Hieronymus, D. Balcha, C. Fan, C. Lin, L. Ghamsari, M. Vidal, W. C. Hahn, D. E. Hill, D. E. Root, A public genome-scale lentiviral expression library of human ORFs. *Nat Methods* **8**, 659-661 (2011).
60. F. H. Wilson, C. M. Johannessen, F. Piccioni, P. Tamayo, J. W. Kim, E. M. Van Allen, S. M. Corsello, M. Capelletti, A. Calles, M. Butaney, T. Sharifnia, S. B. Gabriel, J. P. Mesirov, W. C. Hahn, J. A. Engelman, M. Meyerson, D. E. Root, P. A. Janne, L. A. Garraway, A functional landscape of resistance to ALK inhibition in lung cancer. *Cancer Cell* **27**, 397-408 (2015).
61. J. Shi, E. Wang, J. P. Milazzo, Z. Wang, J. B. Kinney, C. R. Vakoc, Discovery of cancer drug targets by CRISPR-Cas9 screening of protein domains. *Nat Biotechnol* **33**, 661-667 (2015).

62. C. Fellmann, B. G. Gowen, P. C. Lin, J. A. Doudna, J. E. Corn, Cornerstones of CRISPR-Cas in drug discovery and therapy. *Nat Rev Drug Discov* **16**, 89-100 (2017).
63. O. Shalem, N. E. Sanjana, E. Hartenian, X. Shi, D. A. Scott, T. Mikkelsen, D. Heckl, B. L. Ebert, D. E. Root, J. G. Doench, F. Zhang, Genome-scale CRISPR-Cas9 knockout screening in human cells. *Science* **343**, 84-87 (2014).
64. H. Wang, Z. Gao, X. Liu, P. Agarwal, S. Zhao, D. W. Conroy, G. Ji, J. Yu, C. P. Jaronec, Z. Liu, X. Lu, X. Li, X. He, Targeted production of reactive oxygen species in mitochondria to overcome cancer drug resistance. *Nat Commun* **9**, 562 (2018).
65. S. J. Pettitt, D. B. Krastev, I. Brandsma, A. Drean, F. Song, R. Aleksandrov, M. I. Harrell, M. Menon, R. Brough, J. Campbell, J. Frankum, M. Raney, H. N. Pemberton, R. Rafiq, K. Fenwick, A. Swain, S. Guettler, J. M. Lee, E. M. Swisher, S. Stoyanov, K. Yusa, A. Ashworth, C. J. Lord, Genome-wide and high-density CRISPR-Cas9 screens identify point mutations in PARP1 causing PARP inhibitor resistance. *Nat Commun* **9**, 1849 (2018).
66. D. P. McLornan, H. L. Barrett, R. Cummins, U. McDermott, C. McDowell, S. J. Conlon, V. M. Coyle, S. Van Schaebroeck, R. Wilson, E. W. Kay, D. B. Longley, P. G. Johnston, Prognostic significance of TRAIL signaling molecules in stage II and III colorectal cancer. *Clin Cancer Res* **16**, 3442-3451 (2010).
67. M. Devetzi, V. Kosmidou, M. Vlassi, I. Perysinakis, C. Aggeli, T. Choreftaki, G. N. Zografos, A. Pintzas, Death receptor 5 (DR5) and a 5-gene apoptotic biomarker panel with significant differential diagnostic potential in colorectal cancer. *Sci Rep* **6**, 36532 (2016).
68. K. W. Wagner, E. A. Punnoose, T. Januario, D. A. Lawrence, R. M. Pitti, K. Lancaster, D. Lee, M. von Goetz, S. F. Yee, K. Totpal, L. Huw, V. Katta, G. Cavet, S. G. Hymowitz, L. Amler, A. Ashkenazi, Death-receptor O-glycosylation controls tumor-cell sensitivity to the proapoptotic ligand Apo2L/TRAIL. *Nat Med* **13**, 1070-1077 (2007).

69. J. R. McDaniel, J. A. Mackay, F. G. Quiroz, A. Chilkoti, Recursive directional ligation by plasmid reconstruction allows rapid and seamless cloning of oligomeric genes. *Biomacromolecules* **11**, 944-952 (2010).
70. M. B. Herren Wu, Jeffrey Swers, Benoy Chacko (Medimmune LLC, USA, 2013).
71. J. L. Lau, M. K. Dunn, Therapeutic peptides: Historical perspectives, current development trends, and future directions. *Bioorg Med Chem* **26**, 2700-2707 (2018).
72. D. S. Pisal, M. P. Kosloski, S. V. Balu-Iyer, Delivery of therapeutic proteins. *J Pharm Sci* **99**, 2557-2575 (2010).
73. D. E. Meyer, A. Chilkoti, Quantification of the effects of chain length and concentration on the thermal behavior of elastin-like polypeptides. *Biomacromolecules* **5**, 846-851 (2004).
74. D. W. Urry, Physical chemistry of biological free energy transduction as demonstrated by elastic protein-based polymers. *The Journal of Physical Chemistry B* **101**, 11007-11028 (1997).
75. S. R. MacEwan, D. J. Callahan, A. Chilkoti, Stimulus-responsive macromolecules and nanoparticles for cancer drug delivery. *Nanomedicine (Lond)* **5**, 793-806 (2010).
76. W. Hassouneh, K. Fischer, S. R. MacEwan, R. Branscheid, C. L. Fu, R. Liu, M. Schmidt, A. Chilkoti, Unexpected multivalent display of proteins by temperature triggered self-assembly of elastin-like polypeptide block copolymers. *Biomacromolecules* **13**, 1598-1605 (2012).
77. S. R. MacEwan, A. Chilkoti, Controlled apoptosis by a thermally toggled nanoscale amplifier of cellular uptake. *Nano Lett* **14**, 2058-2064 (2014).

78. K. M. Luginbuhl, J. L. Schaal, B. Umstead, E. M. Mastria, X. Li, S. Banskota, S. Arnold, M. Feinglos, D. D'Alessio, A. Chilkoti, One-week glucose control via zero-order release kinetics from an injectable depot of glucagon-like peptide-1 fused to a thermosensitive biopolymer. *Nat Biomed Eng* **1**, 0078 (2017).
79. C. A. Martz, K. A. Ottina, K. R. Singleton, J. S. Jasper, S. E. Wardell, A. Peraza-Penton, G. R. Anderson, P. S. Winter, T. Wang, H. M. Alley, L. N. Kwong, Z. A. Cooper, M. Tetzlaff, P. L. Chen, J. C. Rathmell, K. T. Flaherty, J. A. Wargo, D. P. McDonnell, D. M. Sabatini, K. C. Wood, Systematic identification of signaling pathways with potential to confer anticancer drug resistance. *Sci Signal* **7**, ra121 (2014).
80. P. S. Winter, K. A. Sarosiek, K. H. Lin, M. Meggendorfer, S. Schnittger, A. Letai, K. C. Wood, RAS signaling promotes resistance to JAK inhibitors by suppressing BAD-mediated apoptosis. *Sci Signal* **7**, ra122 (2014).
81. T. Wang, J. J. Wei, D. M. Sabatini, E. S. Lander, Genetic screens in human cells using the CRISPR-Cas9 system. *Science* **343**, 80-84 (2014).
82. G. R. Anderson, P. S. Winter, K. H. Lin, D. P. Nussbaum, M. Cakir, E. M. Stein, R. S. Soderquist, L. Crawford, J. C. Leeds, R. Newcomb, P. Stepp, C. Yip, S. E. Wardell, J. P. Tingley, M. Ali, M. Xu, M. Ryan, S. J. McCall, A. J. McRee, C. M. Counter, C. J. Der, K. C. Wood, A landscape of therapeutic cooperativity in KRAS mutant cancers reveals principles for controlling tumor evolution. *Cell Rep* **20**, 999-1015 (2017).
83. K. C. Wood, Mapping the pathways of resistance to targeted therapies. *Cancer Res* **75**, 4247-4251 (2015).
84. K. R. Singleton, K. C. Wood, Narrowing the focus: a toolkit to systematically connect oncogenic signaling pathways with cancer phenotypes. *Genes Cancer* **7**, 218-228 (2016).

85. E. N. De Toni, S. E. Thieme, A. Herbst, A. Behrens, P. Stieber, A. Jung, H. Blum, B. Göke, F. T. Kolligs, OPG IS REGULATED by β -Catenin and mediates resistance to TRAIL-induced apoptosis in colon cancer. *Clinical Cancer Research* **14**, 4713 (2008).
86. D.-Y. Jin, P. Kaler, V. Galea, L. Augenlicht, L. Klampfer, Tumor Associated Macrophages Protect Colon Cancer Cells from TRAIL-Induced Apoptosis through IL-1 β - Dependent Stabilization of Snail in Tumor Cells. *PLoS ONE* **5**, e11700 (2010).
87. T. Osada, M. Chen, X. Y. Yang, I. Spasojevic, J. B. Vandeusen, D. Hsu, B. M. Clary, T. M. Clay, W. Chen, M. A. Morse, H. K. Lyerly, Antihelminth compound niclosamide downregulates Wnt signaling and elicits antitumor responses in tumors with activating APC mutations. *Cancer Res* **71**, 4172-4182 (2011).
88. K. Azijli, B. Weyhenmeyer, G. J. Peters, S. de Jong, F. A. Kruyt, Non-canonical kinase signaling by the death ligand TRAIL in cancer cells: discord in the death receptor family. *Cell Death Differ* **20**, 858-868 (2013).
89. J. K. Son, S. Varadarajan, S. B. Bratton, TRAIL-activated stress kinases suppress apoptosis through transcriptional upregulation of MCL-1. *Cell Death Differ* **17**, 1288-1301 (2010).
90. J. E. Allen, R. Ferrini, D. T. Dicker, G. Batzer, E. Chen, D. I. Oltean, B. Lin, M. W. Renshaw, A. Kretz-Rommel, W. S. El-Deiry, Targeting TRAIL death receptor 4 with trivalent DR4 Atrimer complexes. *Mol Cancer Ther* **11**, 2087-2095 (2012).
91. A. L. Hong, Y. Y. Tseng, G. S. Cowley, O. Jonas, J. H. Cheah, B. D. Kynnap, M. B. Doshi, C. Oh, S. C. Meyer, A. J. Church, S. Gill, C. M. Bielski, P. Keskula, A. Imamovic, S. Howell, G. V. Kryukov, P. A. Clemons, A. Tsherniak, F. Vazquez, B. D. Crompton, A. F. Shamji, C. Rodriguez-Galindo, K. A. Janeway, C. W. Roberts, K. Stegmaier, P. van Hummelen, M. J. Cima, R. S. Langer, L. A. Garraway, S. L. Schreiber, D. E. Root, W. C. Hahn, J. S. Boehm, Integrated genetic and pharmacologic interrogation of rare cancers. *Nat Commun* **7**, 11987 (2016).

92. Genetic Screens in Human Cells Using the CRISPR-Cas9 System.
93. L. A. Gilbert, M. A. Horlbeck, B. Adamson, J. E. Villalta, Y. Chen, E. H. Whitehead, C. Guimaraes, B. Panning, H. L. Ploegh, M. C. Bassik, L. S. Qi, M. Kampmann, J. S. Weissman, Genome-scale CRISPR-mediated control of gene repression and activation. *Cell* **159**, 647-661 (2014).
94. P. Obexer, M. J. Ausserlechner, X-linked inhibitor of apoptosis protein - a critical death resistance regulator and therapeutic target for personalized cancer therapy. *Front Oncol* **4**, 197 (2014).
95. M. Ehrenschwender, S. Bittner, K. Seibold, H. Wajant, XIAP-targeting drugs resensitize PIK3CA-mutated colorectal cancer cells for death receptor-induced apoptosis. *Cell Death Dis* **5**, e1570 (2014).
96. E. Varfolomeev, B. Alicke, J. M. Elliott, K. Zobel, K. West, H. Wong, J. M. Scheer, A. Ashkenazi, S. E. Gould, W. J. Fairbrother, D. Vucic, X chromosome-linked inhibitor of apoptosis regulates cell death induction by proapoptotic receptor agonists. *J Biol Chem* **284**, 34553-34560 (2009).
97. K. Connolly, R. Mitter, M. Muir, D. Jodrell, S. Guichard, Stable XIAP knockdown clones of HCT116 colon cancer cells are more sensitive to TRAIL, taxanes and irradiation in vitro. *Cancer Chemother Pharmacol* **64**, 307-316 (2009).
98. O. Ndozangue-Touriguine, M. Sebbagh, D. Merino, O. Micheau, J. Bertoglio, J. Breard, A mitochondrial block and expression of XIAP lead to resistance to TRAIL-induced apoptosis during progression to metastasis of a colon carcinoma. *Oncogene* **27**, 6012-6022 (2008).
99. Z. F. Tao, L. Hasvold, L. Wang, X. Wang, A. M. Petros, C. H. Park, E. R. Boghaert, N. D. Catron, J. Chen, P. M. Colman, P. E. Czabotar, K. Deshayes, W. J. Fairbrother, J. A. Flygare, S. G. Hymowitz, S. Jin, R. A. Judge, M. F. Koehler, P. J. Kovar, G. Lessene, M. J. Mitten, C. O. Ndubaku, P. Nimmer, H. E. Purkey, A. Oleksijew, D. C. Phillips, B. E. Sleebbs, B. J. Smith, M. L. Smith, S. K. Tahir, K. G.

- Watson, Y. Xiao, J. Xue, H. Zhang, K. Zobel, S. H. Rosenberg, C. Tse, J. D. Levenson, S. W. Elmore, A. J. Souers, Discovery of a potent and selective BCL-XL inhibitor with in vivo activity. *ACS Med Chem Lett* **5**, 1088-1093 (2014).
100. P. J. Jost, S. Grabow, D. Gray, M. D. McKenzie, U. Nachbur, D. C. Huang, P. Bouillet, H. E. Thomas, C. Borner, J. Silke, A. Strasser, T. Kaufmann, XIAP discriminates between type I and type II FAS-induced apoptosis. *Nature* **460**, 1035-1039 (2009).
101. J. D. Levenson, D. C. Phillips, M. J. Mitten, E. R. Boghaert, D. Diaz, S. K. Tahir, L. D. Belmont, P. Nimmer, Y. Xiao, X. M. Ma, K. N. Lowes, P. Kovar, J. Chen, S. Jin, M. Smith, J. Xue, H. Zhang, A. Oleksijew, T. J. Magoc, K. S. Vaidya, D. H. Albert, J. M. Tarrant, N. La, L. Wang, Z. F. Tao, M. D. Wendt, D. Sampath, S. H. Rosenberg, C. Tse, D. C. Huang, W. J. Fairbrother, S. W. Elmore, A. J. Souers, Exploiting selective BCL-2 family inhibitors to dissect cell survival dependencies and define improved strategies for cancer therapy. *Sci Transl Med* **7**, 279ra240 (2015).
102. P. L. Toogood, P. J. Harvey, J. T. Repine, D. J. Sheehan, S. N. VanderWel, H. Zhou, P. R. Keller, D. J. McNamara, D. Sherry, T. Zhu, J. Brodfuehrer, C. Choi, M. R. Barvian, D. W. Fry, Discovery of a potent and selective inhibitor of cyclin-dependent kinase 4/6. *J Med Chem* **48**, 2388-2406 (2005).
103. S. C. Lueck, A. C. Russ, U. Botzenhardt, R. F. Schlenk, K. Zobel, K. Deshayes, D. Vucic, H. Dohner, K. Dohner, S. Fulda, L. Bullinger, Smac mimetic induces cell death in a large proportion of primary acute myeloid leukemia samples, which correlates with defined molecular markers. *Oncotarget* **7**, 49539-49551 (2016).
104. J. L. Fox, M. MacFarlane, Targeting cell death signalling in cancer: minimising 'Collateral damage'. *Br J Cancer* **115**, 5-11 (2016).
105. M. Angelova, P. Charoentong, H. Hackl, M. L. Fischer, R. Snajder, A. M. Krogsdam, M. J. Waldner, G. Bindea, B. Mlecnik, J. Galon, Z. Trajanoski, Characterization of the immunophenotypes and antigenomes of colorectal

cancers reveals distinct tumor escape mechanisms and novel targets for immunotherapy. *Genome Biol* **16**, 64 (2015).

106. Y. Zhang, N. Li, H. Suh, D. J. Irvine, Nanoparticle anchoring targets immune agonists to tumors enabling anti-cancer immunity without systemic toxicity. *Nat Commun* **9**, 6 (2018).
107. A. S. Cheung, D. K. Y. Zhang, S. T. Koshy, D. J. Mooney, Scaffolds that mimic antigen-presenting cells enable ex vivo expansion of primary T cells. *Nature Biotechnology* **36**, 160 (2018).
108. K. H. Lin, P. S. Winter, A. Xie, C. Roth, C. A. Martz, E. M. Stein, G. R. Anderson, J. P. Tingley, K. C. Wood, Targeting MCL-1/BCL-XL forestalls the acquisition of resistance to ABT-199 in acute myeloid leukemia. *Sci Rep* **6**, 27696 (2016).
109. D. A. Luedtke, X. Niu, Y. Pan, J. Zhao, S. Liu, H. Edwards, K. Chen, H. Lin, J. W. Taub, Y. Ge, Inhibition of Mcl-1 enhances cell death induced by the Bcl-2-selective inhibitor ABT-199 in acute myeloid leukemia cells. *Signal Transduct Target Ther* **2**, 17012 (2017).
110. N. Cancer Genome Atlas Research, M. Albert Einstein College of, S. Analytical Biological, H. Barretos Cancer, M. Baylor College of, H. Beckman Research Institute of City of, A. Buck Institute for Research on, C. Canada's Michael Smith Genome Sciences, S. Harvard Medical, F. G. C. C. Helen, S. Research Institute at Christiana Care Health, B. HudsonAlpha Institute for, L. L. C. Ilisbio, M. Indiana University School of, V. Institute of Human, B. Institute for Systems, C. International Genomics, B. Leidos, H. Massachusetts General, U. McDonnell Genome Institute at Washington, W. Medical College of, C. Medical University of South, C. Memorial Sloan Kettering Cancer, C. Montefiore Medical, NantOmics, I. National Cancer, A. N. National Hospital, I. National Human Genome Research, S. National Institute of Environmental Health, D. National Institute on, D. Other Communication, L. H. S. C. Ontario Tumour Bank, O. I. f. C. R. Ontario Tumour Bank, T. O. H. Ontario Tumour Bank, H. Oregon, U. Science, C.-S. M. C. Samuel Oschin Comprehensive Cancer Institute, S. R. A. International, S. St Joseph's Candler Health, Eli, L. B. I. o. M. I. o. T. Edythe, U. Harvard, H. Research Institute at Nationwide Children's, U. Sidney Kimmel

Comprehensive Cancer Center at Johns Hopkins, B. University of, M. D. A. C. C. University of Texas, H. University of Abuja Teaching, B. University of Alabama at, I. University of California, C. University of California Santa, C. University of Kansas Medical, L. University of, C. University of New Mexico Health Sciences, H. University of North Carolina at Chapel, C. University of Oklahoma Health Sciences, P. University of, R. a. P. M. S. University of Sao Paulo, C. University of Southern, W. University of, M. University of Wisconsin School of, H. Public, I. Van Andel Research, L. Washington University in St, Integrated genomic and molecular characterization of cervical cancer. *Nature* **543**, 378-384 (2017).

Biography

Mandana Taghizadeh Manzari was born April 7th 1988 in Tehran, Iran. She is the daughter of Simin Parvaz and Majid T. Manzari, and has a brother, Mohammad. She graduated from the Massachusetts Institute of Technology with a B.S. degree in Chemical and Biological Engineering (course 10B, 2011). In 2012, Mandana began her Ph.D. in biomedical engineering (expected Fall 2018) at Duke University, in the Chilkoti lab. At Duke, she was awarded the Theo Pilkington Fellowship, the Pharmacological Sciences Training Program Fellowship, and TA of the Year in 2015. Her work helped secure an R21 and DCI/BME collaborative grant, produce several patent applications, and the following publications:

M. T. Manzari, G. R. Anderson, K. H. Lin, M. Cakir, M. Zhang, C. E. Moore, R. N. Skelton, M. Fevre, X. Li, S. E. Wardell, S. A. Costa, K. C. Wood, A. Chilkoti. "Genomically informed small molecule drugs overcome resistance to sustained release formulation of an engineered death receptor agonist." (Submitted)

M. T. Manzari, S. A. Costa, K. C. Wood, A. Chilkoti. "Bridging Genomics and Drug Delivery to Improve Anti-Cancer Therapeutics." (In preparation)

J. B. Spangler, M. T. Manzari, E. K. Rosalia, T. F. Chen, K. D. Wittrup. Triepitopic Antibodies Inhibit Cetuximab-Resistant BRAF- and KRAS- Mutant Tumors via EGFR Signal Repression. *J Mol Biol* **422**(4):532-44 (2012).